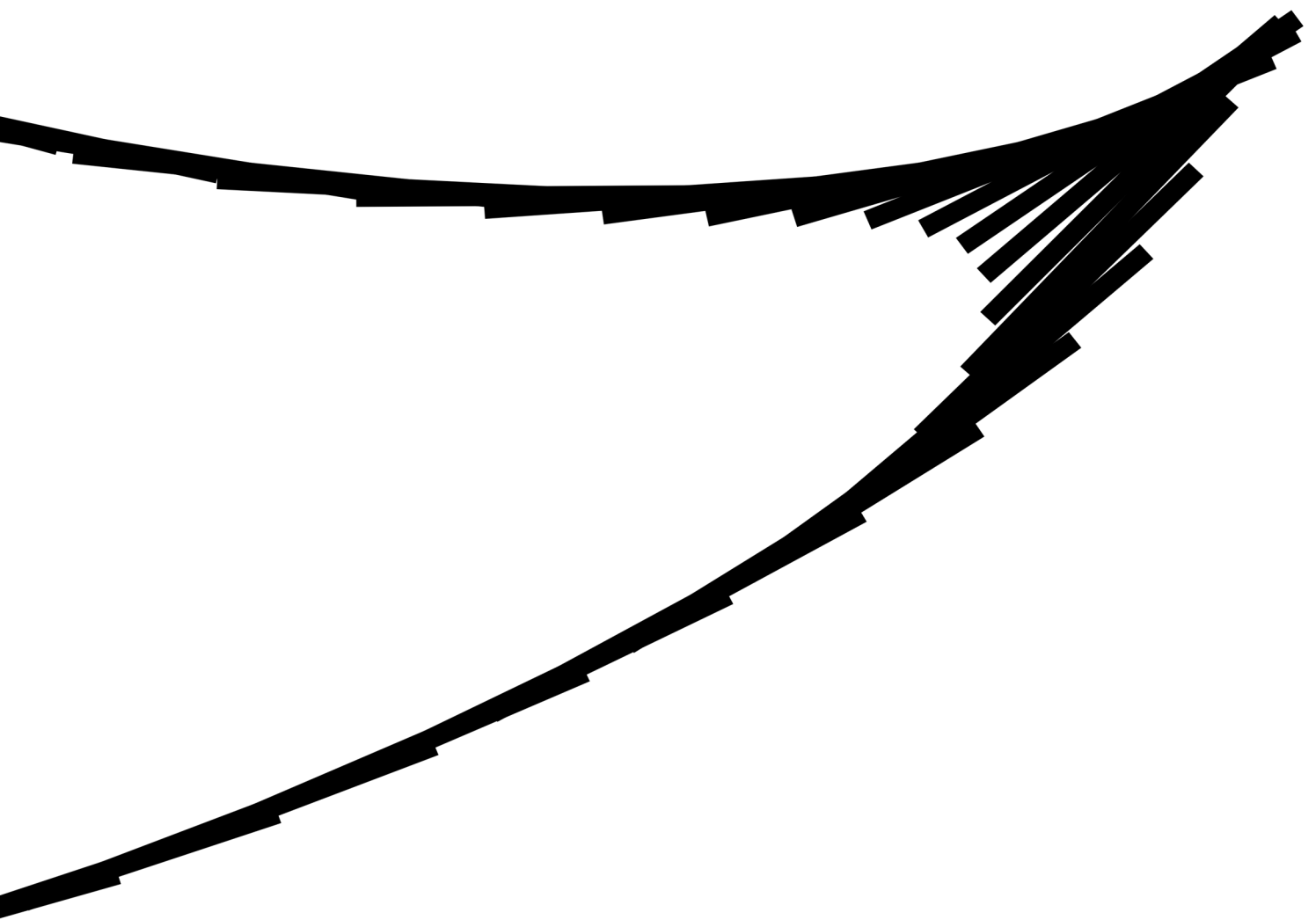


Extending the Existing Modelling Framework for Non-Spherical Particles to Include Flat Plates in Free Fall

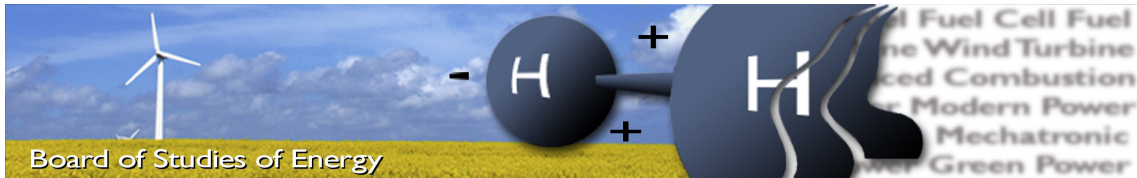
An Experimental and Numerical Investigation of the Unsteady Aerodynamics of Flat Plates



AALBORG UNIVERSITY
STUDENT REPORT

Anna Lyhne Jensen and Jakob Hærvig
Master Thesis Project, June 2014

Thermal Energy and Process Engineering
Aalborg University



Title: Extending the Existing Modelling Framework for Non-Spherical Particles to Include Flat Plates in Free Fall
- An Experimental and Numerical Investigation of the Unsteady Aerodynamics of Flat Plates

Semester: 10.

Semester theme: Master thesis

Project period: 3rd of February to 3rd of June 2014

ECTS: 30

Supervisors: Henrik Sørensen
Marie Cecilie Pedersen

Anna Lyhne Jensen

Jakob Hærvig

Copies: 5

Pages, total: 154, consisting of:
117 pages report
13 pages enclosures
24 pages formalia and blank pages

Appendices: A-J

Enclosures: A-B

Supplements: CD

Synopsis:

Accurate modelling of flows with non-spherical particles is important for a wide range of industrial applications. State-of-the-art CFD software fails to include crucial information on exact shape and orientation of the particles, resulting in less accurate modelling of highly non-spherical objects such as flat plates.

An extensive study of the forces and torques on a plate, reveals the existing modelling framework for flat plates in free fall to be insufficient to describe the actual trajectories using an Euler-Lagrange approach. Through numerous CFD simulations, new correlations are proposed for rotational lift, rotational drag, and centre of pressure location, resulting in a model able to predict the trajectories with high accuracy.

A comparison to a regime map found in literature suggests the model to be general applicable to a wide range of plates, and therefore this work has led to a significant improvement of the existing modelling framework for flat plates in free fall.

By signing this document, each member of the group confirms that all participated in the project work and thereby all members are collectively liable for the content of the report.

Nomenclature

Acronym	Description
6DOF	Six Degrees of Freedom
CFD	Computational Fluid Dynamics
MATLAB	Matrix Laboratory (software)
UDF	User Defined Function

Subscripts	Description
f	Fluid
p	Plate
x	x-direction
y	y-direction
z	z-direction
i	i'th entry

Coordinates	Coordinate system description
(X-Y)	Stationary global coordinate system
(x-y)	Global coordinate system following plate
(x'-y')	Local coordinate system following and rotating with plate

Symbol	Description	Unit	Dimensions
a	Side length of superelliptic shape	m	L
\vec{a}	Acceleration	m/s^2	LT^{-2}
a_1	Constant used for unsteady drag coefficient calculation	—	—
a_2	Constant used for unsteady drag coefficient calculation	—	—
c_1	Constant used for angle of attack calculation	rad	—
c_2	Constant used for angle of attack calculation	rad	—
cp_b	Centre of pressure for buoyancy force	m	L
cp_o	Centre of pressure for aerodynamic forces	m	L
A	Surface area of plate	m^2	L^2
\bar{A}	Added mass matrix	kg or kg·m	M or ML
\vec{A}	Surface area normal inward pointing vector	m^2	L^2
b	Side length of superelliptic shape	m	L
b	Depth of plate	m	L
C	Added mass coefficient	—	—
C_f	Friction drag coefficient	—	—
C_D	Drag coefficient	—	—
$C_{D,r}$	Drag coefficient for resistance force	—	—
C_L	Lift coefficient	—	—
C_{per}	Net perpendicular force coefficient	—	—
C_{tan}	Net tangential force coefficient	—	—
dt	Time step	s	T
\vec{F}_a	Added mass force	N	MLT^{-2}
\vec{F}_b	Buoyancy force	N	MLT^{-2}
\vec{F}_D	Drag force	N	MLT^{-2}
\vec{F}_g	Gravitational force	N	MLT^{-2}
\vec{F}_h	History force	N	MLT^{-2}
\vec{F}_L	Lift force	N	MLT^{-2}
\vec{F}_r	Resulting force	N	MLT^{-2}
\vec{F}_p	Pressure force	N	MLT^{-2}
\vec{F}_τ	Viscous force	N	MLT^{-2}
\vec{g}	Gravitational acceleration	m/s^2	LT^{-2}
h	Height of plate	m	L
I	Moment of Inertia	Nm	ML^2T^{-2}
I^*	Dimensionless moment of inertia	—	—
L	Length of plate	m	L
m	Mass of plate	kg	M
m_a	Added mass	kg	M
n	Superelliptic exponent	—	—
n	Number of samples	—	—
n	Number used for summation	—	—
\vec{n}	Unit vector perpendicular to surface of plate	—	—
p	Total pressure	N/m^2	$ML^{-1}T^{-2}$
p_h	Hydrostatic pressure	N/m^2	$ML^{-1}T^{-2}$
Re	Reynolds number	—	—
S	Surface area of a given particle	m^2	L^2
s	Surface area of a perfect sphere	m^2	L^2
s	Sample standard deviation	—	—
t	Time	s	T

$t_{\alpha/2}$	Critical value of t-distribution	—	—
T	Temperature	°C	Θ
\vec{T}	Torque	Nm	ML^2T^{-2}
\vec{T}_b	Buoyancy force off-set torque	Nm	ML^2T^{-2}
\vec{T}_o	Aerodynamic forces off-set torque	Nm	ML^2T^{-2}
\vec{T}_{resist}	Resistance torque	Nm	ML^2T^{-2}
$\vec{T}_{g \rightarrow 1}$	Transformation from global to local coordinate system	—	—
$\vec{T}_{1 \rightarrow g}$	Transformation from local to global coordinate system	—	—
u_*	Friction velocity	m/s	LT^{-1}
$u_{t,a}$	Apparent terminal velocity	m/s	LT^{-1}
\vec{u}	Plate velocity	m/s	MT^{-1}
U_∞	Free stream velocity	m/s	MT^{-1}
\vec{v}	Relative fluid velocity	m/s	MT^{-1}
\vec{w}	Fluid velocity	m/s	MT^{-1}
V	Volume	m^3	L^3
\bar{x}	Sample mean value	—	—
y^+	Dimensionless first cell height	—	—
α	Angle of Attack	rad	—
β	Height to length aspect ratio	—	—
Δy_1	First cell height	m	L
μ	Dynamic viscosity	Pa·s	$MT^{-1}L^{-1}$
ω	Angular velocity	rad/s	T^{-1}
$d\omega/dt$	Angular acceleration	rad/s ²	T^{-2}
ϕ	Sphericity factor	—	—
φ	Relative fluid velocity angle	rad	—
ρ	Density	kg/m ³	ML^{-3}
$\vec{\tau}_w$	Wall shear stress	Pa	$ML^{-1}T^{-2}$
σ	Standard deviation	—	—
θ	Angular position	rad	—
θ_e	Angle for equal-sided object	rad	—
θ_{max}	Maximum angle in cell	rad	—
θ_{min}	Minimum angle in cell	rad	—

Preface

This masters thesis project is written in the period 3rd of February to 3rd of June 2014 at the Department of Energy Technology at Aalborg University.

Reading Instructions

Throughout the project, references are made to relevant literature using the Harvard method, where the source in the text is referenced to with (Author, Year). References are listed in the back of the report.

Figures, tables, and equations are numbered according to the chapter in which they are located. That is, the first figure in chapter 4 has number 4.1, the next number 4.2, etc. Explanatory text is given below figures and above tables. The appendices and enclosures are addressed with letters, while the files on the attached CD are addressed with numbers.

The appendices, found in the back of this report, are denoted Appendix A, Appendix B, etc. These appendices contain information relevant to different parts of the main report. References to these appendices are made throughout the report. The enclosures are placed after the appendices and contain pieces of code developed throughout the project.

Most of the figures in this report are either scalable vector graphic or very high resolution images. Therefore, the report is enjoyed the best at a high resolution digital display if a hard-copy is not available. Additionally, all the figures can be found on the CD attached to the report.

Furthermore, both the report and the executive summary can be found in digital versions on the CD attached.

Acknowledgments

We would like to express our gratitude to our supervisors Associate Professor Henrik Sørensen and Ph.D Student Marie Cecilie Pedersen, who have been helpful with discussions, guidance, plate fascination, and constant inspiration when the plate would not fall as we wanted it to. Also thanks to Professor Karl Erik Widell who has taken his time to provide us with useful information on unsteady fluid dynamics related to flat plates.

Contents

1	Introduction	1
1.1	Existing Modelling Framework for the Motion of Non-spherical Particles	1
1.2	Characterising the Motion of Flat Plates in Free Fall by Dimensionless Parameters	3
2	Problem Statement and Description	9
2.1	Problem Statement	10
2.2	Problem Description	10
2.2.1	Arrangement of the Report	12
3	Quasi-steady Two-dimensional Model of Flat Plates in Free Fall	13
3.1	Governing Equations and Model Definitions	13
3.1.1	Governing Equations	13
3.1.2	Global and Local Coordinate Systems	14
3.1.3	Definition of Translational and Rotational Velocities used in Model	15
3.1.4	Angle of Attack	16
3.2	Physical Mechanisms Resulting in Force Contributions	17
3.2.1	Net Force on Plate in Free Fall	18
3.2.2	Drag Force	21
3.2.3	Lift Force	25
3.2.4	Added Mass Force	27
3.2.5	History Force	29
3.2.6	Buoyancy Force	31
3.2.7	Gravity Force	32
3.3	Physical Mechanisms Resulting in Torque Contributions	32
3.3.1	Net Torque on Plate in Free Fall	33
3.3.2	Rotational Resistance Torque	33
3.3.3	Torque Contribution from Aerodynamic Forces	34
3.3.4	Torque Contribution from Buoyancy	36
3.4	Procedure of Model	37
3.5	Limitation of Quasi-steady 2D model	38
3.5.1	Interference with Vortices Shed back in Time	39
3.5.2	Saffman's Lift Force Due to Shear Velocity Field	39
3.5.3	Magnus Lift Force Due to Heavy Rotational Motion	39
4	Numerical Simulations of Freely Falling Flat Plates using Computational Fluid Dynamics	41
4.1	Overall Mesh Topology	41
4.1.1	Dynamic Mesh Zone	42
4.1.2	Non-deforming Boundary Layer Mesh	43
4.2	Modelling of Turbulence	45
4.3	Degrees of Freedom	45
4.3.1	Extraction of Results for Moving Object	46
4.4	Computational Domain and Boundary Conditions	46
4.5	Grid Independence Analysis	47
4.6	Domain Size Independence Analysis	49
4.7	Time Step Independence Analysis	50
4.8	Convergence	51

5	Experimental Investigation of Flat Plates	53
5.1	Description of Experiment	53
5.2	Apparatus and Instruments	54
5.3	Processing of Results	54
5.4	Presentation of Results	55
5.4.1	Statistical Considerations	56
5.5	Sources of Error and Uncertainties	57
5.5.1	Precision of Plate Release Time	58
5.5.2	Three-dimensional Effects	58
5.5.3	Consistency of Plates and Manufacturing Flaws	58
6	Results for Freely Falling Flat Plates	61
6.1	Validation of CFD Simulations by Experiment	61
6.2	Visualisation of Flow Field	66
6.3	Terminal Velocity and Characterisation of Regime	69
7	Development of New Correlations for the Quasi-steady Two-dimensional Model	71
7.1	New Lift Coefficient Correlations	72
7.2	New Drag Coefficient Correlations	75
7.3	New Centre of Pressure Correlation	78
7.4	Results and Validation of Revised Model	80
7.4.1	Deviations in x-position as function of time	81
7.4.2	Deviations in y-position as function of time	82
7.4.3	Deviations in orientation angle as function of time	83
7.5	Extending the Model Capabilities to Other Flat Plates	84
7.5.1	On the Validity of the Revised Model Using Motion Regimes	86
8	Closure	87
8.1	Conclusions	87
8.2	Suggestions for Further Work and Discussion	89
	References	91
	List of Appendices	95
A	Numerical Investigation of Translational Drag and Lift Coefficients	
B	Numerical Investigation of Added Mass Coefficient Matrix	
C	Numerical Investigation of History Force	
D	Sensitivity Analysis of Revised Model Results	
E	Logical Statements to Determine the Sign of Centre of Pressure Location	
F	Details on Dynamic Meshes	
G	Numerical Investigation of Rotational Drag and Lift Coefficients	
H	Detailed CFD Results	
I	CD Content	

Chapter 1

Introduction

Modelling the behaviour of flows with particles is important for several industrial applications, such as cyclone separators, dust collectors, and pulverised-coal combustors (Zastawny et al., 2012). Models of flows where the motion of such particles is important, often rely on computational fluid dynamics (CFD). One approach of using CFD is to solve for the exact flow field around the particle. This allows the total force acting on the particle to be determined by integrating the pressure field and velocity gradients normal to the surface around the surface of the plate. However, one drawback of this approach is the lack of the possibility of handling the collision of particles. The collisions become increasingly important when the particle load in the flow increases (Crowe et al., 1998). One way to deal with high particle loads is by statistical correlations which describe how the particles interact based on experiments. These correlations can be used in an Euler-Lagrange modelling framework where the particles are treated like point masses and the forces are modelled using correlations. Whilst this method is well established and validated for spherical particles, much work still remains to be done for highly non-spherical particles.

1.1 Existing Modelling Framework for the Motion of Non-spherical Particles

The Euler-Lagrange methodology used in state of the art commercial CFD software allows different force contributions to be included. Considering a fluid without temperature gradients and neglecting the small scale Brownian forces, the forces can be listed as follows (ANSYS, Inc., 2011b):

- Drag force due to the pressure distribution and velocity gradients around the surface of the object. This results in a force parallel to the relative fluid velocity.
- Saffman's lift force due to shear in the velocity field resulting in a force contribution perpendicular to the relative fluid velocity.
- Added mass force due to acceleration of the fluid surrounding an accelerating object. The result is an additional drag term.

The contributions listed above are modelled using correlations covering a wide range of conditions including different Reynolds numbers, particle and fluid densities, and shear

fields. For perfectly spherical particles the drag coefficient correlations are typically a function of the Reynolds number only. This is the case in the correlation presented by Morsi and Alexander (1972) and used by ANSYS.

Since the particles in most industrial flows can not accurately be simplified to a spherical shape, studies have been carried out trying to extend the existing correlations to include non-spherical particles. When non-spherical particles are considered, the drag coefficient correlations are typically extended to take a sphericity factor into account (Haider and Levenspiel, 1989). The sphericity factor definition, used in recent studies, describes the ratio between the surface area of the particle S and that of a perfect sphere s with same volume, and was first proposed by Wadell (1935). The definition is presented in Equation (1.1).

$$\phi = \frac{s}{S} \quad (1.1)$$

One disadvantage of these relatively simple correlations is the fact that they fail to include the exact shape of the particle. This means that two particles with entirely different shapes, and consequently different aerodynamic behaviour, can have the same sphericity factor (Rosendahl, 1998). To include more information about the exact geometry, studies have been done to characterise the particle geometry by a superelliptic shape function (Rosendahl, 2000). In general super-ellipsoids in two dimensions are described by their aspect ratio β and superelliptic exponent n as shown in Equation (1.2).

$$\left(\frac{x}{a}\right)^n + \left(\frac{y}{b}\right)^n = 1 \quad n \leq 2.0, \quad \frac{b}{a} = \beta \leq 1.0 \quad (1.2)$$

Equation (1.2) allows different geometries to be expressed in the same manner, which allows for a general description of entirely different shapes ranging from perfect spheres ($\beta = 1, n = 2$) to long flat plates ($\beta \gg 1, n = \infty$). Figure 1.1 gives an overview of different shapes generated by Equation (1.2).

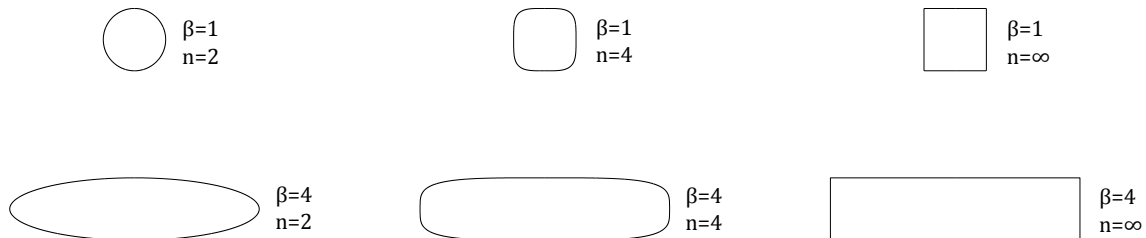


Figure 1.1. Different superellipsoids classified by aspect ratio β and superelliptic exponent n .

Due to non-spherical shapes, lift will be generated and the forces on non-spherical particles will depend on the orientation of the particle. The generated lift results in a secondary motion of the particle, perpendicular to the overall direction of motion. Several attempts have been done trying to develop a model with orientation dependent coefficients. In order to be able to precisely predict the motion, the fact that the centre of gravity and the centre of pressure are not coincident has to be taken into account. As the behavior of objects differs considerably depending on the exact geometry, general studies are intractable and consequently only few geometries have been studied in details.

The PhD thesis by Rosendahl (2000) investigated the general motion of non-spherical particles on the form given by Equation (1.1) by developing a numerical model able to predict the

motion of non-spherical particles including the orientation of the particles. However, this work failed to validate the model by experiments since focus was on swirl burners, where initial conditions were complicated. Another PhD thesis by Pesavento (2006) concentrated on the free fall trajectories of different objects ranging from ellipsoids ($n = 2$) to flat plates ($n = \infty$). In this work the orientation of the particles was modelled as well. Since well-controlled free fall trajectories were investigated, validation based on experiments was possible. Some of the discrepancies between the model and experiments by Pesavento (2006) were later investigated by Jin and Xu (2008). One conclusion of their work was that the motion of ellipses and rectangles is very alike even though the rectangle rotates much slower. Other studies of superelliptic shapes include Zastawny et al. (2012) who investigated various objects, Tanabe and Kaneko (1994) who focused on falling papers, and Belmonte et al. (1998) who focused on thin paper strips.

Summing up, the existing modelling of non-spherical particles in commercial CFD software is deficient due to:

- failure to include exact shape of the particle
- failure to include orientation of the particle

Even though attempts to include these factors for a small range of non-spherical particles similar to cylinder have been proposed in literature such as by Yin et al. (2004), a general model has yet to be defined.

In this work, flat plates characterised by a high aspect ratio β as well as a high superelliptic exponent n will be of interest. For this shape the instantaneous orientation is of utmost importance to describe the exact motion at a given time. The following presents an overall description of the motion of flat plates in free fall.

1.2 Characterising the Motion of Flat Plates in Free Fall by Dimensionless Parameters

The dimensions of the plate used in this work are sketched in Figure 1.2. The length of the plate is denoted L , the height of the plate is denoted h , and the width of the plate is denoted b .

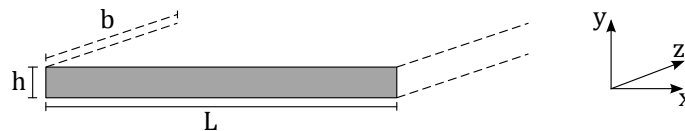


Figure 1.2. Flat plate with length L , height h , and width b .

Depending on the plate dimensions, plate material, plate moment of inertia, and surrounding fluid, different characteristic free fall trajectories occur. The regimes of the trajectories range from a steady falling regime, to a periodic oscillating motion regime to a tumbling motion regime. Examples of different types of free fall trajectories are illustrated in Figure 1.3.

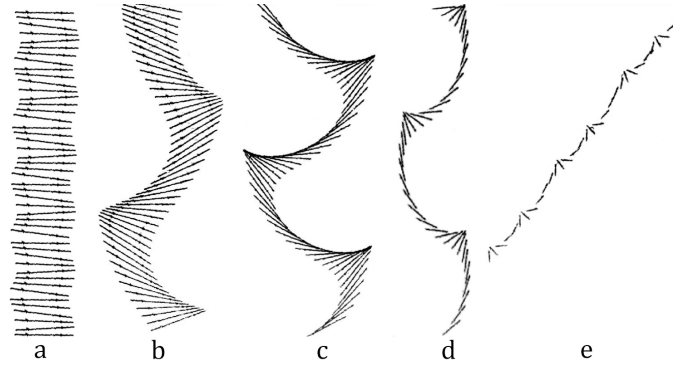


Figure 1.3. Different distinct types of motion for falling plates; Steady falling regime (a), periodic oscillating motion regime (b-d), and tumbling motion regime (e) (Belmonte et al., 1998). Note the steady falling regime has been added to the original figure.

Several attempts have been made to categorise the occurrences of the different regimes and describe each of them in details. Researchers, such as Field et al. (1997) have categorised the motion of disks in details, and Smith (1970) did a similar study for flat plates. These studies categorising the trajectories rely on extensive experimental data, since such experiments are straightforward when only the type of trajectory is of interest. Furthermore, different studies have been dealing with the details of a single trajectory type. The periodic oscillation motion has been categorised and described by Tanabe and Kaneko (1994), Tanabe and Kaneko (1995), Andersen et al. (2005a), Andersen et al. (2005b), and Pesavento (2006). For flat plates the tumbling motion regime is governed by auto-rotation, which was first described by Riabouchinsky (1935) and later investigated in studies by Iversen (1979) and latest Hargreaves et al. (2014). Even though quite some studies have been carried out, much work still remains to be done to fully categorise the motion and especially the importance of unsteady effects.

To characterise the trajectory type in general, the dimensionless moment of inertia I^* shown in Equation (1.3) is used, where I , ρ_f , and L denote the moment of inertia, fluid density and a characteristic length respectively (Smith, 1970). Further information on the moment of inertia I for the plate considered in this work is given in Section 3.1.

$$I^* = \frac{32I}{\pi\rho_f L^4} \quad (1.3)$$

When a flat plate with rectangular cross section is considered, Equation (1.3) reduces to Equation (1.4).

$$I^* = \frac{8\rho_p h(L^2 + h^2)}{3\pi\rho_f L^3} \quad (1.4)$$

Besides the dimensionless moment of inertia, the Reynolds number Re , based on the apparent terminal velocity $u_{t,a}$, is used as a parameter to characterise the occurrences of the different motion regimes. The Reynolds number is defined as given in Equation (1.5).

$$Re = \frac{\rho_f u_{t,a} L}{\mu} \quad (1.5)$$

Studies mapping the motion regimes based on the dimensionless moment of inertia and Reynolds number include Willmarth et al. (1964), Smith (1970), and Field et al. (1997). Figure 1.4 shows such a regime map of the free fall trajectories for flat plates by Smith (1970).

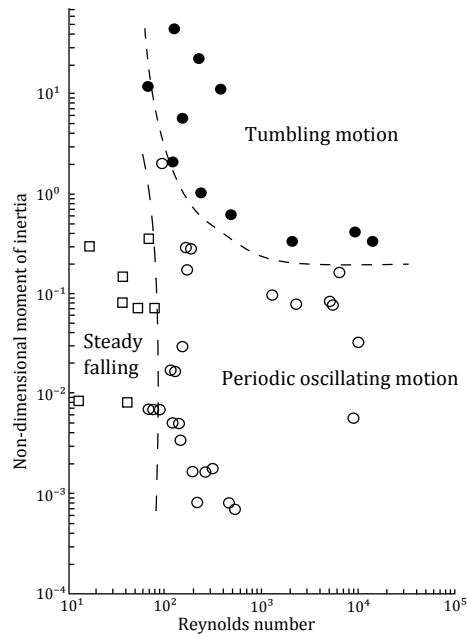


Figure 1.4. Regime map describing the type of falling motion as function of dimensionless moment of inertia and Reynolds number (Smith, 1970).

As the figure indicates, flat plates with $Re < 10^2$ will typically fall steadily without any dominant secondary motion. When the Reynolds number is increased, the plates will either have a side-to-side oscillating motion or tumbling motion depending on the moment of inertia. The boundary between the periodic oscillating motion regime and tumbling motion regime is approximately constant $I^* = 0.2$ for $Re > 10^3$. Later studies such as Belmonte et al. (1998) verified these boundaries by a set of quasi-two-dimensional experiments.

Expressing the Reynolds number for free fall motion is not trivial. When the plate falls in the steady falling regime and does not have a secondary motion, the terminal velocity can easily be estimated by balancing out the gravity, buoyancy and the drag force and using an appropriate drag coefficient to calculate the terminal velocity. However, when the plate has a more or less dominant secondary motion, the terminal velocity varies with time and in this case the apparent terminal velocity is used. Figure 1.5 illustrates how the terminal velocity is function of time while the apparent terminal velocity does not vary with time.

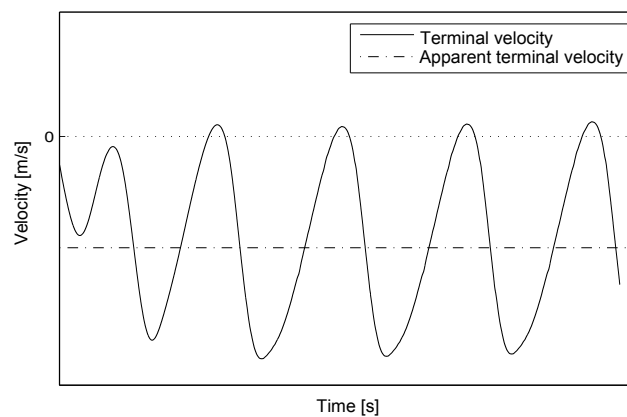


Figure 1.5. Terminal and apparent terminal velocities as function of time for a flat plate in free fall.

Basing the Reynolds number on the apparent terminal velocity is convenient as it can easily be measured in experiments. The drawback of expressing the Reynolds number based on the apparent terminal velocity is the fact that it remains unknown until measurements or simulations are made. There have been several attempts in the literature to estimate the apparent terminal velocity of different non-spherical particles before an actual experiment is made.

Such studies of flat plates in free fall include Andersen et al. (2005a) who suggests balancing gravity, buoyancy and drag force by using the drag coefficient of 1 to give a rough estimate on the terminal velocity. Other studies of non-spherical particles include Haider and Levenspiel (1989) and Clift et al. (1978) who suggest more sophisticated methods by taking the sphericity factor into account.

The following section gives the reader an opportunity to get familiarised with flat plates in free fall by a simple experiment where a slip of paper is let free to fall.

Try it Yourself Plate

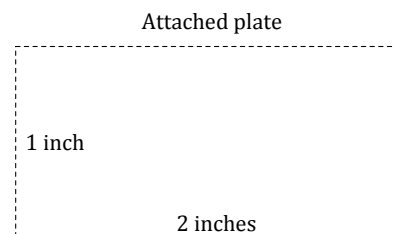
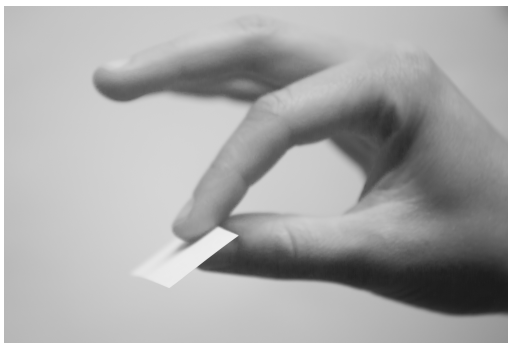
The intention of this page is to familiarise the reader with the fascinating world of flat plates in free fall. The motion of falling leaves, papers, snow flakes, and playing cards may seem beautiful yet chaotic to many people. Due to the complex nature of this time dependent motion, and the fact that it has not yet been successfully described analytically, it remains an interesting phenomena for scientists as well as an important field for industries dealing with flows containing non-spherical particles.

This interest and fascination date back to Maxwell who did a series of experiments back in 1853 by letting a rectangular slip of paper (2 inches long and 1 inch broad) fall freely (Maxwell, 1853). Based on their trajectories he published a series of thoughts on, what governs especially the side to side way motion of such objects.

The slip of paper below measures 2 by 1 inches, has a density of approximately 800 kg/m^3 , and a thickness of 0.1 mm. The result is a dimensionless moment of inertia $I^* = 4.4$ when rotating about its longer axis, which will typically be the case after some time in free fall depending on the initial conditions and surrounding air. A rough estimate on the apparent terminal velocity results in 0.5 m/s, corresponding to a Reynolds number $Re \approx 800$. These conditions should, according to Figure 1.4, result in the slip of paper falling in the tumbling motion regime.

It is now up to the reader to drop the slip of paper to observe and classify the trajectory. Suggestions on how to get the plate to fall in the tumbling motion regime rather than chaotic regime is given in the following (best performed indoor):

1. Remove the authentic slip of paper from this page
2. Close all windows and doors to minimise sources of error
3. Hold the slip on the long edge as shown in the following figure at a height of approximately 2 metres:



4. Release the slip of paper at approximately 30 deg to horizontal and enjoy

Chapter 2

Problem Statement and Description

Different approaches can be used to model the motion of non-spherical particles. One approach is to resolve the flow field around the particle using CFD and calculate the forces and torques directly by integrating the pressure- and velocity field around the particle. Based on the calculated force and torque, the position and orientation can be updated at the end of each time step. Since the exact flow field must be used, this approach is computationally expensive and limited by the numerical accuracy of the CFD simulations such as mesh resolution, space and time discretisation schemes, and time step size. Due to the high computational cost, it is typically not feasible to resolve the flow field around each particle in particle-laden flow containing a large amount of particles (Richter and Nikrityuk, 2013).

Another approach is to model the particles as point-masses, keeping track of the orientation of the particle, and using correlations to describe the forces and torques explicitly. These correlations can be found by either experiments or different types of CFD simulations. As the accuracy of this method relies solely on the accuracy of the correlations, it is of utmost importance to increase the accuracy and investigate the validity of these correlations.

The two above mentioned approaches can be summarised as shown in Figure 2.1

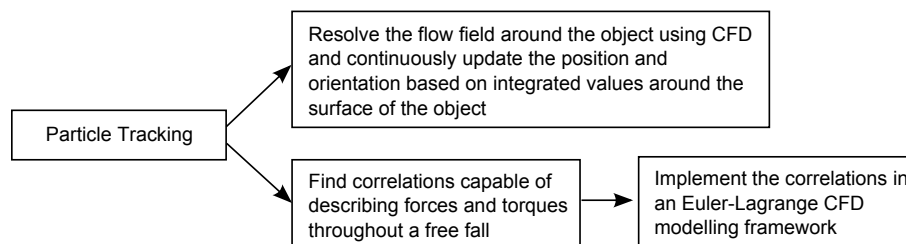


Figure 2.1. An overview of the different approaches used to predict the motion of non-spherical particles.

One limitation of both approaches is the fact that they require separate models to describe particle-particle or particle-wall collisions and the effect of turbulence on the particle trajectories. These phenomena are typically included using statistical models such as a particle cloud tracking model and discrete random walk model respectively (ANSYS, Inc., 2011b). In the present study, the motion of a single flat plate in free fall in a stagnant fluid is investigated. Therefore, models describing particle collisions and turbulence dispersions are not important to describe the trajectory.

2.1 Problem Statement

This work aims to develop a numerical quasi-steady model using correlations to describe forces and torques capable of predicting the motion of flat plates in free fall in a stagnant fluid. This leads to the following problem statement:

How can a numerical quasi-steady 2D model based on correlations and capable of predicting the motion of flat plates be developed with the purpose of implementing the results in an Euler-Lagrange CFD modelling framework?

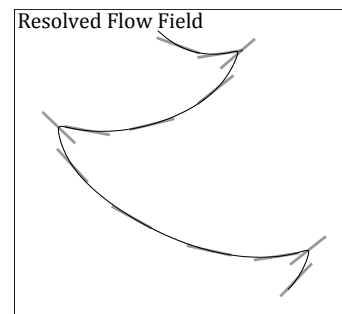
2.2 Problem Description

For this work a plate with length $L = 40$ mm, aspect ratio $\beta = 1/20$, and superelliptic exponent $n = \infty$ is chosen for further investigation. The investigation focuses on the regime of periodic oscillation motion with a Reynolds number in the order of 10^3 - 10^4 . The plate used in experiments and simulations is made of aluminium with density 2700 kg/m^3 and the surrounding fluid is water at approximately 20°C .

In order to model the free fall behaviour of flat plates correctly using quasi-steady approximations, the correlations used to describe the forces and torques correctly are of uttermost importance. Therefore, the work will be split into two different parts investigating the free fall by different methods. These different parts are described in the following along with small illustrations.

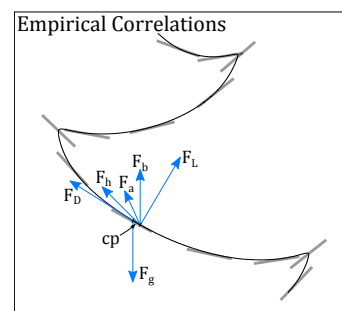
Part 1 - CFD Simulations of Flat Plates in Free Fall

The freely falling plate in a stagnant fluid is modelled numerically using commercial CFD software. Instead of modelling the plate as a point mass and relying on correlations to describe the different forces, the detailed coupled time-dependent velocity and pressure field around the plate is used to describe the total force and torque acting on the plate at any time during the free fall. The reason for choosing to investigate the free fall trajectory instead of a non-moving plate is the possibility of simple validation techniques by comparing trajectories. Digital video camera measurements of a plate falling freely in water will be used to validate the CFD simulations by comparing the free fall trajectories.



Part 2 - Quasi-steady 2D Model of Flat Plates in Free Fall

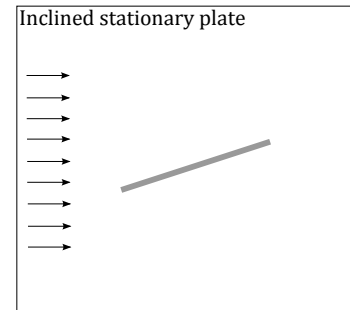
A model able to predict the free fall trajectories is developed. Instead of relying on a coupled velocity and pressure field, the forces and torques are modelled explicitly using different correlations. The overall goal of the model is to obtain free fall trajectories similar to those obtained by the CFD simulations and the experiments described in part 1. When such a model is developed, the results could be implemented in an Euler-Lagrange CFD modelling framework for non-spherical particles with shapes similar to flat plates.



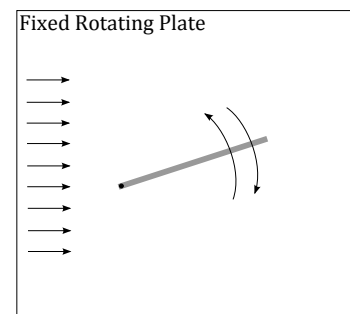
Additional CFD Simulations

In order to model the free fall trajectories in part 2, an additional set of CFD simulations is carried out. The purpose of these simulations is to investigate and quantify the importance of different, both steady and transient, fluid dynamic related phenomena in relation to flat plates in free fall.

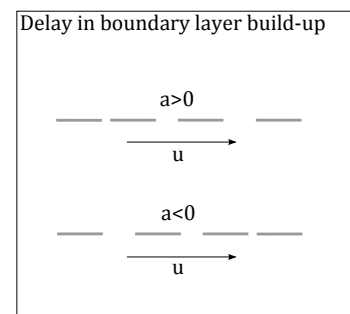
A fixed plate inclined to the flow is modelled numerically using commercial CFD to investigate the time-averaged forces acting on a stationary plate. The results will contribute with detailed drag and lift characteristics for the exact plate of interest in this project for a wide variety of angles of attack and Reynolds numbers. The result is a set of correlations describing the time-independent drag- and lift coefficients as function of angle of attack and Reynolds number.



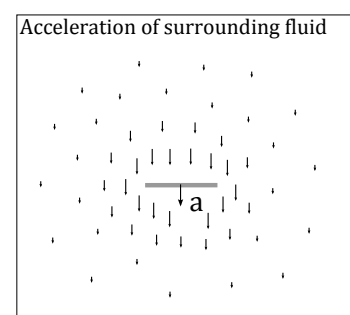
A fixed plate rotating around the leading edge is modelled numerically using commercial CFD software to investigate the time-dependent forces acting on the plate. These effects can be described by an in-stationary boundary layer and dynamic stall caused by a leading edge vortex passing over the side of the plate. The results will contribute with angular velocity dependent drag and lift coefficients for the exact plate of interest in this project.



A plate translating parallel to its long side is modelled numerically using commercial CFD software. The purpose of these simulations is to investigate the time-dependent forces on the plate as the boundary layer is changing in time at different rates caused by different plate accelerations. This in-stationary force commonly known as the history or Basset force is of interest as deformations of the boundary layer is directly related to the viscous forces on the plate.



A plate accelerating due to a well-defined applied force is modelled numerically using commercial CFD software. The purpose of these simulations is to investigate the time-dependent forces on the plate due to acceleration of the surrounding fluid as the plate accelerates. The surrounding fluid acts as an added or virtual mass that has to be accelerated with the plate corresponding to an additional mass. The results of the simulations is a description of this added mass force.



2.2.1 Arrangement of the Report

To give the reader an overview of the structure of the report, a short description of the content of each chapter is presented in the following and summarised in Figure 2.2.

- Chapter 3 contains a detailed description of how the motion of flat plates in free fall can be modelled. Furthermore, state-of-the-art correlations from literature used to describe different force and torque contributions are presented. In order to investigate some of the contributions in more details, different CFD simulations are used. As presented in Section 2.2, these simulations are:
 - Inclined stationary plate to investigate lift and drag coefficients at different angles and Reynolds numbers.
 - Fixed rotating plate to investigate time-dependent forces.
 - Translating plate to simulate delay in boundary layer build up.
 - Accelerating plate to simulate acceleration of surrounding fluid.

References are given to appendices describing how these CFD simulations are set up.

- Chapter 4 contains a description of the configuration of the CFD simulations for the freely falling plate.
- Chapter 5 describes experiments using digital video recordings made to validate the simulations of the free fall trajectories.
- Chapter 6 presents the results obtained by the CFD simulations of flat plates in free fall. The results are compared and validated using the results obtained through the experiment.
- Chapter 7 contains a description of how new correlations are developed in this work to extend the existing modelling framework for flat plates in free fall. This development will be based upon the findings made throughout this report and result in a revised model formulation.

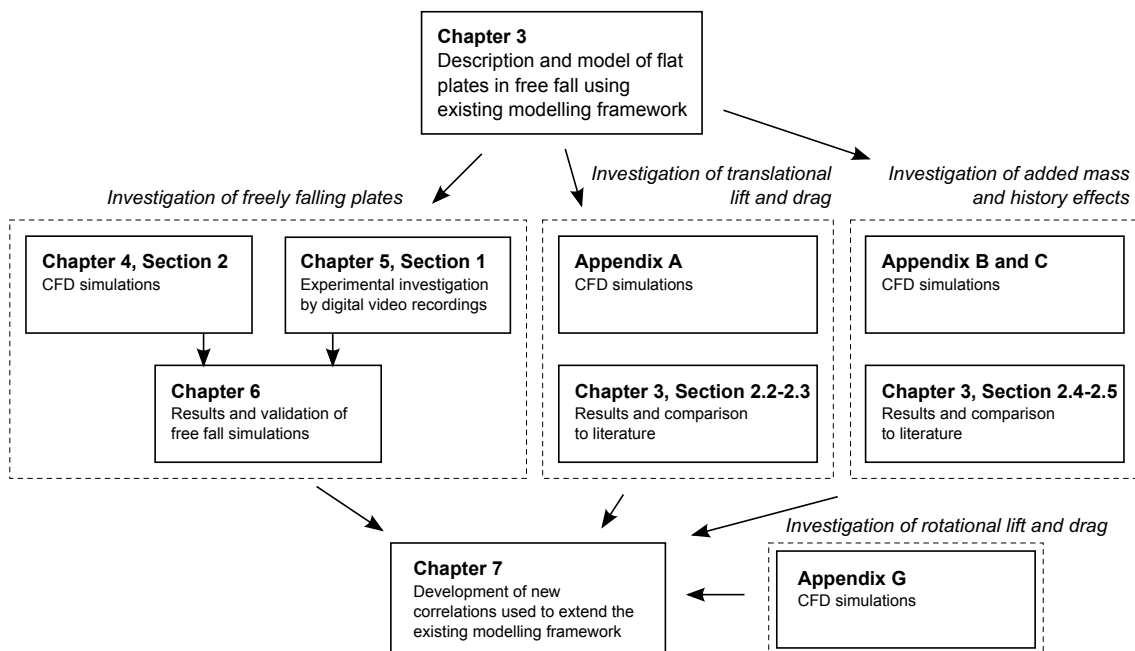


Figure 2.2. Overview of how the rest of the report is arranged.

Chapter 3

Quasi-steady Two-dimensional Model of Flat Plates in Free Fall

This chapter describes the development of a quasi-steady 2D model which has the purpose of predicting the motion of a flat plate in free fall. The model will be based on existing correlations found in either literature, through CFD simulations, or by fluid mechanical theory.

Firstly, the equations governing the motion and model definitions are given in Section 3.1. Afterwards, the different force contributions are discussed in Section 3.2 followed by a description of the different torque contributions in Section 3.3. Finally, an overview of the procedure of the model is given in Section 3.4 while limitations of the model are discussed in Section 3.5.

3.1 Governing Equations and Model Definitions

This section presents the governing equations of motion along with definitions of coordinate systems used to simplify the expressions used throughout the model. Finally different velocities as well as an angle of attack are defined.

3.1.1 Governing Equations

The model is based on a Newtonian description of both translational and rotational motion. This means that the translational velocity \vec{u} of the plate can be described in differential form by Equation (3.1).

$$m \frac{d\vec{u}}{dt} = \sum_{i=1}^n \vec{F}_{r,i} \quad (3.1)$$

The different force contributions $\vec{F}_{r,i}$ are explained in details throughout Section 3.2. Similarly there will be a net torque rotating the plate. In general, the angular velocity ω of a plate around the three axes, can be described in differential form by Equation (3.2) to (3.4) (Meriam and Kraige, 2007). The marks used as superscripts in the equations relate to the coordinate system used. Details on the different coordinate systems used throughout the model are given in Subsection 3.1.2.

$$I_{x'} \frac{d\omega_{x'}}{dt} - \omega_y \omega_z (I_y - I_z) = \sum_{i=1}^n T_{x',i} \quad (3.2)$$

$$I_{y'} \frac{d\omega_{y'}}{dt} - \omega_{z'} \omega_{x'} (I_{z'} - I_{x'}) = \sum_{i=1}^n T_{y',i} \quad (3.3)$$

$$I_{z'} \frac{d\omega_{z'}}{dt} - \omega_{x'} \omega_{y'} (I_{x'} - I_{y'}) = \sum_{i=1}^n T_{z',i} \quad (3.4)$$

Since the model is limited to two dimensions, only Equation (3.4) is required to describe the rotational motion of the plate. Additionally, this equation reduces to Equation (3.5), since the angular velocities around the x- and y-axis are zero.

$$I_{z'} \frac{d\omega_{z'}}{dt} = \sum_{i=1}^n T_{z',i} \quad (3.5)$$

The moment of inertia $I_{z'}$ used in Equation (3.5) can be calculated using the integral in Equation (3.6) (Meriam and Kraige, 2007).

$$I_z = \int (x^2 + y^2) dm \quad (3.6)$$

For a flat plate with length L , height h , and homogenous density ρ_p , Equation (3.6) reduces to Equation (3.7).

$$I_z = \frac{Lh\rho_p(L^2 + h^2)}{12} \quad (3.7)$$

The different contributions to the net torque $T_{z'}$, and how these contributions can be modelled, are described in details in Section 3.3.

As already mentioned, different coordinate systems are used throughout the model. Details on these coordinate systems are given in the following.

3.1.2 Global and Local Coordinate Systems

In this work, the position of the plate is kept track of in a stationary global coordinate system (X-Y), which has its origin where the plate is located initially. Besides the stationary global coordinate system, a coordinate system following the plate will be used. This coordinate system will simply be denoted as the global coordinate system (x-y). Furthermore, a local coordinate system both following and rotating with the plate is used. This will be denoted as the local coordinate system (x'-y'). The three coordinate systems are illustrated in Figure 3.1.

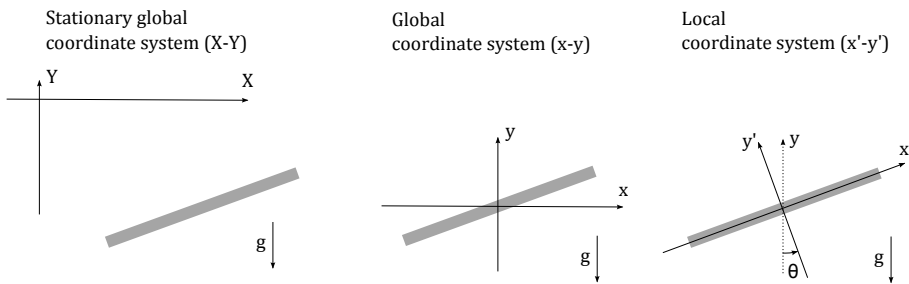


Figure 3.1. The stationary global coordinate system (X-Y), the global coordinate system following the plate (x-y), and the local coordinate system following and rotating with the plate (x'-y'). The orientation angle θ is used to keep track of how the plate is orientated throughout a free fall, that is θ satisfies $\theta \in [-\infty; \infty]$. In the figure θ is positive.

As seen in Figure 3.1, the global coordinate system and local coordinate system are related through the orientation angle θ . When quantities are transformed from one coordinate system to another, transformation matrices are used. Equation (3.8) shows the transformation matrix $\bar{T}_{g \rightarrow l}$ which transforms quantities from the global to the local coordinate system. Similarly the transformation matrix in Equation (3.9) is used to transform quantities from the local to the global coordinate system.

$$\bar{T}_{g \rightarrow l} = \begin{bmatrix} \cos(\theta) & \sin(\theta) \\ -\sin(\theta) & \cos(\theta) \end{bmatrix} \quad (3.8)$$

$$\bar{T}_{l \rightarrow g} = \begin{bmatrix} \cos(\theta) & -\sin(\theta) \\ \sin(\theta) & \cos(\theta) \end{bmatrix} \quad (3.9)$$

In the description of the different correlations presented later, the velocity of the plate relative to the fluid is an important factor. A definition of the velocities used throughout the model is given in the following.

3.1.3 Definition of Translational and Rotational Velocities used in Model

The translational velocity of the plate relative to the stationary global coordinate system changes throughout the fall when the motion is not in the steady-falling regime. In the following, the instantaneous velocity in the stationary global coordinate system will be denoted \vec{u} . The instantaneous local fluid velocity relative to the global coordinate system will be denoted \vec{w} , thus $\vec{w} = 0$ for a stagnant fluid. Even though the fluid is stagnant, vortices shed back in time might interfere with the plate trajectories. This effect is neglected in the quasi-steady 2D model described in this chapter. How this assumption affects the results is discussed in Section 3.5.

The velocity of interest in the model is the instantaneous plate velocity \vec{u} relative to the instantaneous local fluid velocity \vec{w} . This will be called the relative fluid velocity and be denoted by \vec{v} . The relative fluid velocity \vec{v} is defined by Equation (3.10).

$$\vec{v} = \vec{w} - \vec{u} \quad (3.10)$$

Furthermore the angle of the relative fluid velocity will be used in the model. This will be denoted φ , and is defined by Equation (3.11).

$$\varphi = \tan^{-1} \left(\frac{v_y}{v_x} \right) \quad (3.11)$$

Figure 3.2 is a graphical representation of the velocities and the relative fluid angle defined in Equation (3.10) and Equation (3.11) respectively.

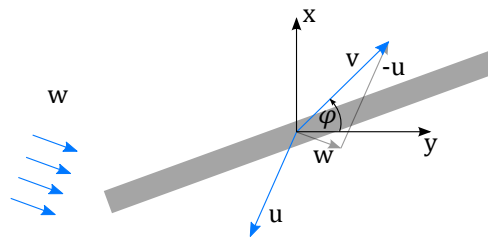


Figure 3.2. Relation between plate velocity \vec{u} , fluid velocity \vec{w} , and relative fluid velocity \vec{v} .

Similar to the case of translational motion, different angular velocities are defined. The angular velocity of the plate itself around the z-axis is denoted $\omega_{z,p}$ and the angular velocity of the fluid around the centre of the plate is denoted $\omega_{z,f}$. The difference between these two gives a relative rotational velocity $\omega_{z,rel}$. This relative rotational velocity is calculated by Equation (3.12).

$$\omega_{z,rel} = \omega_{z,p} - \omega_{z,f} \quad (3.12)$$

Figure 3.3 serves to visualise Equation (3.12) and the three angular velocities.

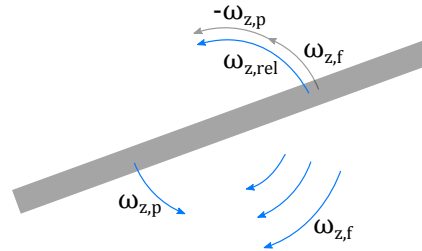


Figure 3.3. Relation between plate rotational velocity $\omega_{z,p}$, fluid rotational velocity $\omega_{z,f}$, and relative fluid rotational velocity $\omega_{z,rel}$.

The angle between the chord and the relative fluid velocity is important when the different force contributions are to be expressed by correlations. This angle will be denoted the angle of attack α , and is described in details in the following subsection.

3.1.4 Angle of Attack

The angle of attack is defined as the angle between the plate chord and the relative fluid velocity \vec{v} , and lies in the interval $[-90^\circ; 90^\circ]$. The angle is measured from the chord of the plate to the relative fluid velocity \vec{v} , with the counterclockwise direction resulting in positive angles. This is illustrated in Figure 3.4. The figure illustrates how the angle of attack α varies for four different plate orientations at a constant relative fluid velocity. Note how the sign of α suddenly changes when the orientation angle is increased from 80° to 100° .

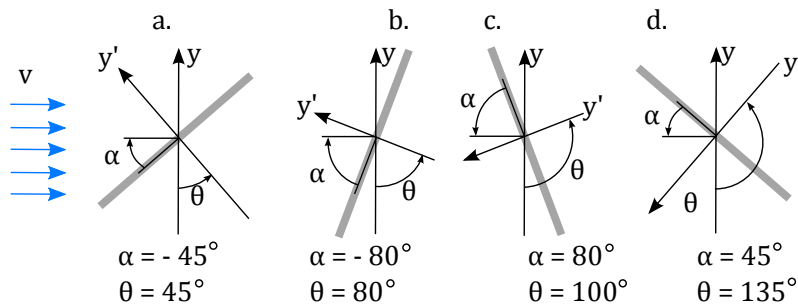


Figure 3.4. Angle of attack at different orientation angles with a constant relative fluid velocity \vec{v} . The relative fluid angle φ is 0° in the figure.

The result of the sudden change in angle of attack is a discontinuity, when the plate is rotated at a constant relative fluid angle φ . Depending on the relative fluid angle φ the discontinuity will appear at different orientation angles. Figure 3.5 shows the angle of attack α as function of orientation angle θ at two different relative fluid velocity angles.

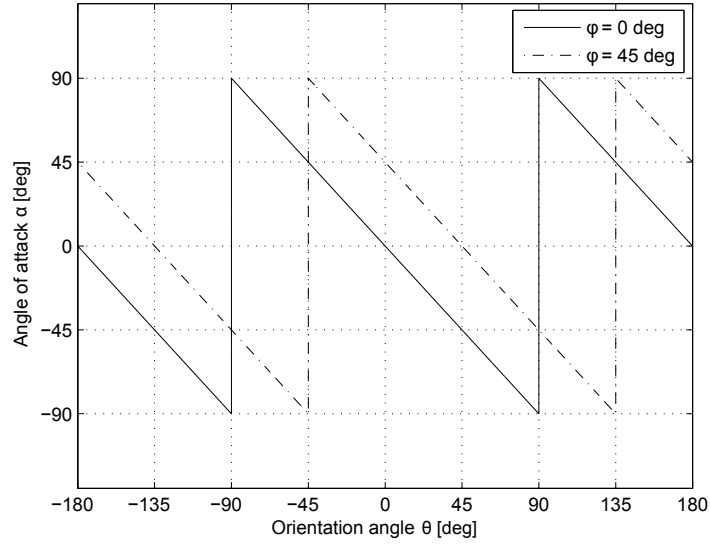


Figure 3.5. The angle of attack α as a function of the orientation angle of the plate θ . Note how the two curves are shifted by exactly the relative fluid angle φ .

The function shown above can be describe by a saw-tooth function. This function is shown in Equation (3.13), where c_1 is the amplitude of the function equal to $\pi/2$ and c_2 is the period equal to π .

$$\alpha = \frac{2 \cdot c_1}{\pi} \tan^{-1} \left(\cot \left(\frac{\pi \cdot \theta}{c_2} - \frac{\pi}{2} - \varphi \right) \right) \quad (3.13)$$

This equation will be used throughout the model to calculate the angle of attack α based on the relative fluid velocity \vec{v} and the plate orientation angle θ .

The following section contains a description of the forces acting on a plate in free fall. Furthermore, details on different state-of-the-art correlations used to model the different force contributions will be given.

3.2 Physical Mechanisms Resulting in Force Contributions

The following section describes the different force contributions to \vec{F}_r used in Equation (3.1) to update both the translational velocity and position of the plate. Those contributions expected to be important to the total net force on a plate in free fall, are listed in the following along with their point of application:

- Drag force \vec{F}_D due to differences in pressure and wall shear stress around the plate. The drag force always acts through a point denoted the centre of pressure for the aerodynamic forces, and in the same direction as the relative fluid velocity. The centre of pressure off-set results in a torque contribution which is explained in details in Section 3.3. The drag force is described in details in Subsection 3.2.2.
- Lift force \vec{F}_L due to differences in pressure and wall shear stress around the plate. The lift force always acts through the centre of pressure for the aerodynamic forces and perpendicular to the relative fluid velocity. The centre of pressure off-set results in a torque

contribution which is explained in details in Section 3.3. The lift force is described in details in Subsection 3.2.3.

- Added mass force \vec{F}_a due to fluid inertial forces when the plate accelerates. The force slows down the acceleration of the plate. The exact direction of the force depends on the plate orientation and the relative fluid velocity. Like the drag and lift forces, the added mass force results in a torque contribution. The added mass force along with the torque contribution is described in details in Subsection 3.2.4.
- History force \vec{F}_h caused by a delay in boundary layer build-up. The force slows down the acceleration of the plate. This force contribution is described in Subsection 3.2.5.
- Buoyancy force \vec{F}_b due to the pressure varying with depth in the surrounding fluid. The result is an upward pointing force with a magnitude proportional to the density of the surrounding fluid. This force acts in the centre of pressure for the buoyancy force, resulting in a torque contribution which is described in Section 3.3. The buoyancy force is described in details in Subsection 3.2.6.
- Gravity force \vec{F}_g caused by the plate being accelerated towards the centre of the Earth. This force is described in details in Subsection 3.2.7.

In the list shown above, some force contributions have been neglected. These include the Saffman's lift force due to a shear in the surrounding velocity field, which will have no impact in a stagnant fluid. How a shear velocity field is expected to alter the free fall behaviour of a flat plate is explained in Section 3.5. Furthermore, there will be a lift force when an object rotates while it translates as the surrounding fluid is either accelerated or decelerated. This is denoted the Magnus lift force and is only expected to be important when the plate repeatedly tumbles over. More information on the Magnus lift force is given in Section 3.5.

The following section gives a general description of the net force acting on a flat plate during a free fall.

3.2.1 Net Force on Plate in Free Fall

The instantaneous net force \vec{F}_r acting on the plate can at any time be described by a combination of an integral over the pressure distribution p around the plate, an integral over the wall shear stresses $\vec{\tau}_w$ acting on the plate surfaces, and the gravity force \vec{F}_g . This is given in Equation (3.14). In this equation the hydrostatic pressure and therefore buoyancy effects are included in the pressure term p .

$$\vec{F}_r = \int p d\vec{A} + \int \vec{\tau}_w dA + \vec{F}_g \quad (3.14)$$

When the plate is inclined to the relative fluid velocity \vec{v} , there will be an asymmetric pressure distribution around the plate surfaces. An example of such a pressure distribution, visualised by pressure contours, is shown in Figure 3.6.

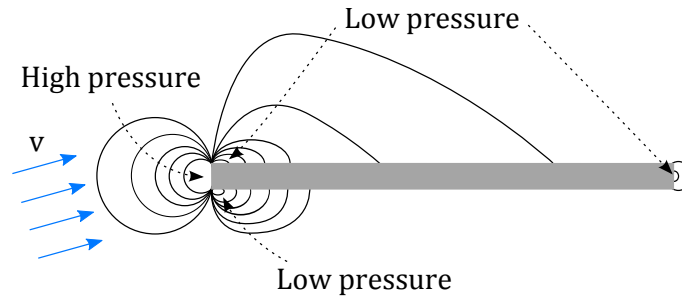


Figure 3.6. Example of pressure distribution around a flat plate inclined to the relative flow velocity.

The asymmetric pressure distribution around the plate shown in the figure results in a net force which is not parallel to the relative flow velocity. Rewriting Equation (3.14), the net force \vec{F}_r is the sum of the three force contributions given in Equation (3.15). In this Equation \vec{F}_p is the pressure force, \vec{F}_τ is the viscous force, and \vec{F}_g is the gravity force.

$$\vec{F}_r = \vec{F}_p + \vec{F}_\tau + \vec{F}_g \quad (3.15)$$

The pressure force is directly related to the local pressure field around the surface of the plate while the viscous force is related to the velocity gradients normal to the surface of the plate.

Pressure Force Contribution

As already stated the pressure force contribution is directly related to the pressure field around the surface of the plate. The total pressure force acting on the plate is determined using Equation (3.16) assuming the pressure field around the plate is known. In the equation \vec{A} denotes an inward pointing vector normal to the surface.

$$\vec{F}_p = \int p \, d\vec{A} \quad (3.16)$$

Figure 3.7 shows an example of how the pressure multiplied by the area normal vector gives the force vector of a discrete element at the corner of the plate.

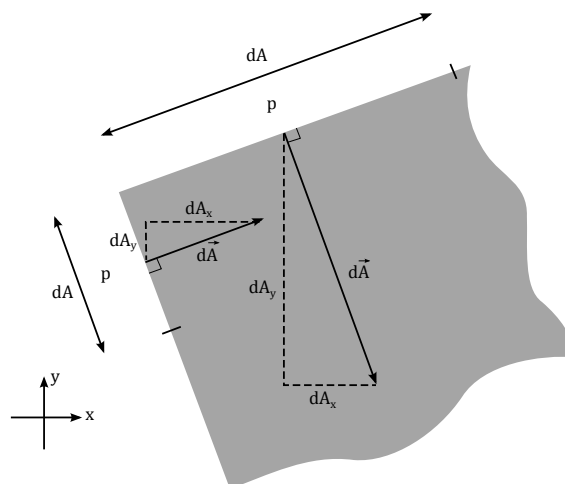


Figure 3.7. Example of how the normal area vector pointing inward gives the direction of the local force acting on each discrete element of the plate surface.

Note that the pressure field is not calculated explicitly in the 2D quasi-steady model. Instead, the quasi-steady 2D model is based on descriptions of the different contributions to the overall net force listed on page 17.

Viscous Force Contribution

Fluid moving around the plate exerts a viscous force on the plate due to velocity differences between the plate and the surrounding fluid. The overall contribution due to viscous effects can be estimated by integrating over the wall shear stress $\vec{\tau}_w$ around the plate surface as shown in Equation (3.17).

$$\vec{F}_\tau = \int \vec{\tau}_w dA \quad (3.17)$$

In the above shown equation, the wall shear stress $\vec{\tau}_w$ is calculated as the dynamic viscosity multiplied with the velocity gradient in the viscous sublayer. The calculation is shown in Equation (3.18) where \vec{n} denotes a vector normal to the surface.

$$\vec{\tau}_w = -\mu \frac{d\vec{v}}{d\vec{n}} \quad (3.18)$$

In the viscous sublayer, the velocity gradient is linear. An example of the linear velocity profile sufficiently close to the wall is given in Figure 3.8.

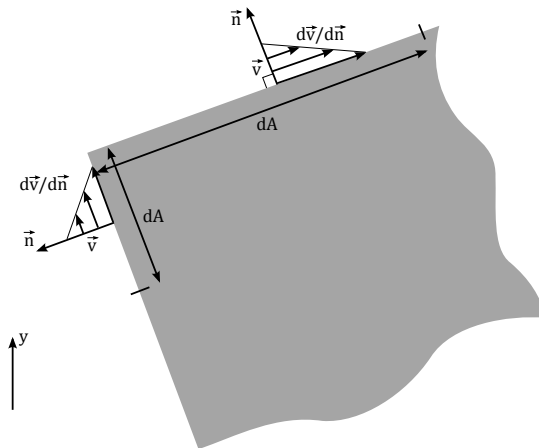


Figure 3.8. Example of the linear velocity profile sufficiently close to the wall used to calculate the viscous forces. Note that the plate is moving and the surrounding fluid is stagnant resulting in a fluid velocity different from zero at the surface.

Note again that this force contribution is not included explicitly in the quasi-steady 2D model. Even though neither the exact pressure field nor the wall shear stresses are used to calculate the net force in the quasi-steady 2D model, the principles are important for the physical understanding and for the interpretation of the results of the CFD simulations presented in Chapter 6.

Instead of relying on an exact pressure field and wall shear stresses around the plate, the quasi-steady 2D model is based on descriptions of the different contributions to the overall net force listed on page 17. One such force contribution is the drag force which is explained in the following section.

3.2.2 Drag Force

The drag force is defined as a component of the net force \vec{F}_r acting in the same direction as the undisturbed relative fluid velocity (Hoerner, 1965). The drag force is commonly accepted to be a function of the fluid density ρ_f , a characteristic surface area $L \cdot b$ (b is unit length in the 2D model developed in this work), a drag coefficient C_D , and the relative fluid velocity squared $|\vec{v}| \cdot \vec{v}$, as shown in Equation (3.19) (Munson et al., 2010). When expressing the relative fluid velocity in this way, the drag force automatically acts in the same direction as the relative fluid velocity \vec{v} .

$$\vec{F}_D = \frac{1}{2} \rho_f \cdot L \cdot b \cdot C_D |\vec{v}| \cdot \vec{v} \quad (3.19)$$

The drag coefficient will in this work be based on the plate length L instead of the plate height h , since $L \gg h$ and therefore L governs the flow around the plate. Furthermore, the drag coefficient is assumed to be a function of plate orientation described by the angle of attack and the Reynolds number only, that is $C_D = f(\alpha, Re_L)$. A detailed explanation of the drag coefficient and state-of-the-art correlations are given in the following subsection.

Orientation Dependent Drag Coefficient for Flat Plates

The pressure field and wall shear stress around the plate strongly depend on how the plate is orientated compared to the relative fluid velocity. The relation between the orientation and relative fluid velocity can be expressed through the angle of attack which makes it convenient to use in the description of the orientation dependency. Numerous attempts to describe the drag coefficient as function of angle of attack for various non-spherical objects have been done in literature. One of the most investigated shapes approaching the flat plate is the airfoil because of its industrial importance. Even though correlations describing the drag coefficient as function of angle of attack at different Reynolds numbers have been well validated for airfoils as described by Hoerner (1965), much research still remains to be done for simple flat plates.

For a flat plate the extreme values of drag coefficients are at 0 deg and 90 deg, where the drag coefficient is typically dominated by viscous and pressure effects respectively. One crude assumption commonly used to take the angle of attack into account when describing the drag coefficient is to use a blending function. These blending functions only take the extreme values at $\alpha = 0$ deg and $\alpha = 90$ deg into account and use a combination of trigonometric functions to make a more or less sophisticated fit between these extremes.

Different blending functions found in literature to describe the drag coefficient variation between the two extremes of various objects are given in Table 3.1.

Table 3.1. Different blending functions found in literature to describe the drag coefficient variation between the two extremes as function of the angle of attack.

Function	Applied to	Author
$C_D(\alpha) = C_D(0) \cos^2 \alpha + C_D(90) \sin^2 \alpha$	Plates in free fall	Pesavento (2006)
$C_D(\alpha) = C_D(0) + (C_D(90) - C_D(0)) \sin^3 \alpha $	Non-spherical particles	Rosendahl (2000)

The two blending functions presented in Table 3.1 are visualised in Figure 3.9.

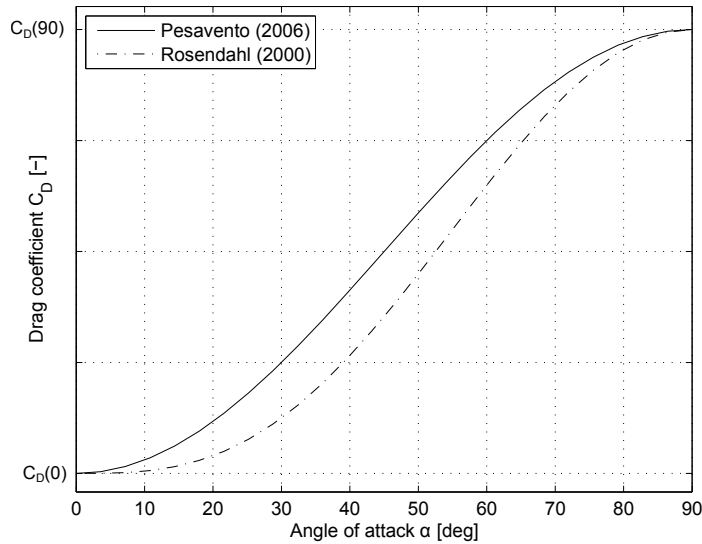


Figure 3.9. Blending functions found in literature used to estimate the drag coefficient at various angle of attack.

In order to successfully utilise such correlations to model the drag coefficient for flat plates in free fall, one has to question their validity. The shape of the functions is not a function of Reynolds number, which is expected to be important when describing both the extreme values and the shape of the blending functions. In order to investigate the shape of these blending functions at a well-defined Reynolds number, a series of transient CFD simulations have been carried out at $Re_L = 10000$ with constant angles of attack ranging from 0 deg to 90 deg. Additional information on these simulations is given in Appendix A. Figure 3.10 shows the results of the simulations together with the blending function presented by Rosendahl (2000).

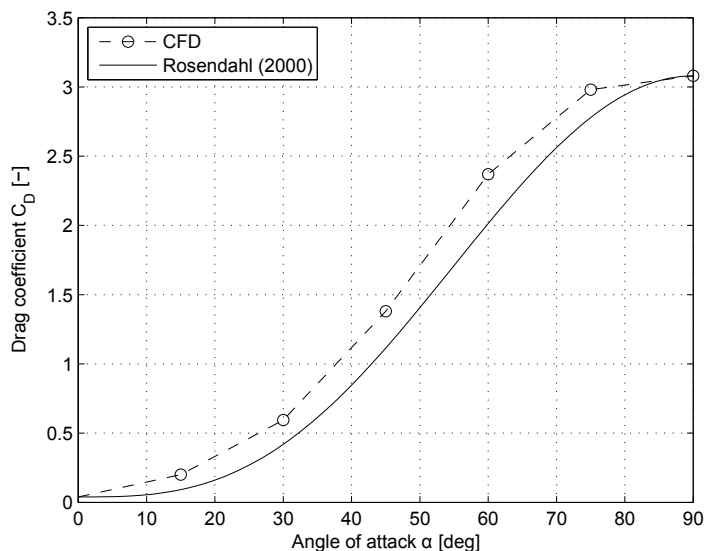


Figure 3.10. Drag coefficient as function of angle of attack for a flat plate found by computational fluid dynamics simulations with $Re_L = 10000$.

As seen in the figure, the simulations show that the drag coefficient does in general increase, as

the angle of attack is increased. The figure indicates that the shape of the blending functions presented in literature correspond well to the results obtained by CFD.

The drag coefficient is a function of the Reynolds number as well. Since the Reynolds number varies throughout a free fall, it is of importance to investigate this dependency as well.

Reynolds Number Dependent Drag Coefficient for Flat Plates

When describing the Reynolds number dependency on the drag coefficient for a flat plate, different distinct flow regimes describing the flow around the plate are typically used. These are listed in the following (Munson et al., 2010):

- Very low Reynolds number flows where viscous forces are dominant.
- Moderate Reynolds number flows with laminar boundary layer ($Re_L < 5 \cdot 10^5$).
- High Reynolds number flows with turbulent boundary layer ($Re_L \geq 5 \cdot 10^5$).

These different types of flow greatly affect the drag coefficient. For infinitesimally thin plates at $\alpha = 0$ deg, Baker (1983) suggests the correlations presented in Equation (3.20) to determine the friction drag coefficient as function of Reynolds number Re_L .

$$C_{D(0)} = \begin{cases} 1.328 / (Re_L)^{0.5}, & \text{if laminar boundary layer} \\ 0.455 / (\ln Re_L)^{2.58} - 1700 / Re_L, & \text{if transitional boundary layer} \end{cases} \quad (3.20)$$

Where laminar boundary layer flow is encountered for $Re_L < 5 \cdot 10^5$ and transitional is for flow with $Re_L \geq 5 \cdot 10^5$. The correlations presented in Equation (3.20) are visualised in Figure 3.11.

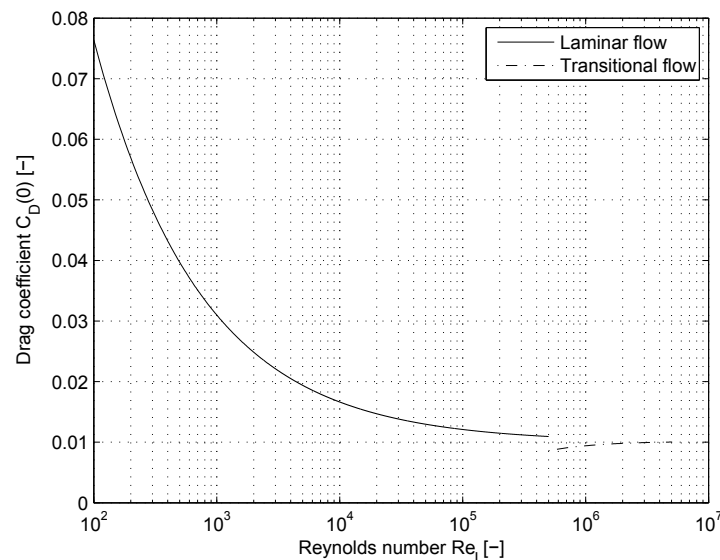


Figure 3.11. Drag coefficient for flat plates parallel to the flow at different Reynolds numbers (Baker, 1983).

As seen in the figure, the correlations suggest the drag coefficient to decrease as the Reynolds number increases. For low Reynolds numbers the drag coefficient is high corresponding to

Stokes flow. The decrease in drag coefficient at $Re_L = 5 \cdot 10^5$ correspond to the transition from a laminar boundary layer to a part of the boundary layer becoming turbulent. When the Reynolds number is increased further, the drag coefficient remains almost constant corresponding to the transition from laminar to turbulent Re_x moving towards the leading edge of the plate (Munson et al., 2010).

Investigation of Drag Coefficient using CFD

For this specific work, Reynolds numbers much lower than $5 \cdot 10^5$ are important. In order to model the drag coefficient in details, a series of steady CFD simulations at angles of attack of 0 deg and 90 deg have been carried out. These are further described in details in Appendix A. Figure 3.12 shows the results of these simulations.

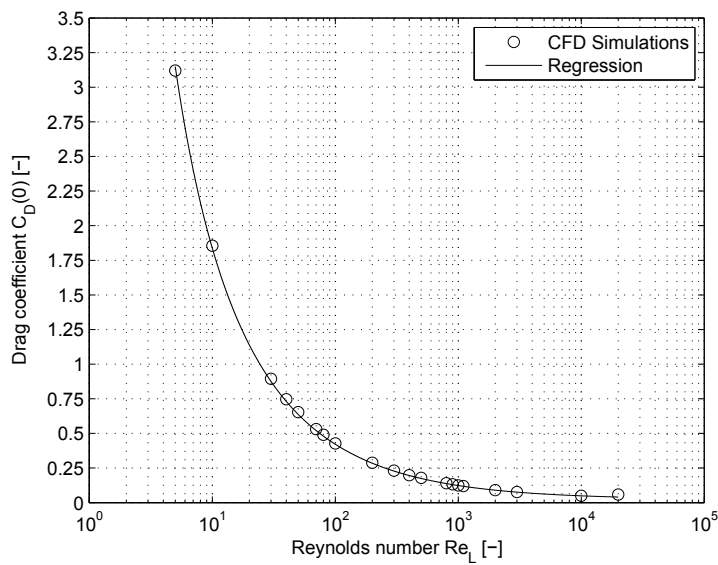


Figure 3.12. Drag coefficient for parallel flow at various Reynolds numbers Re_L found by the CFD simulations presented in Appendix A.

Based on the simulations presented in the figure, the function in Equation (3.21) describing the drag coefficient for parallel flow as function of the Reynolds number is made.

$$C_D(0) = \frac{0.023 + 5.45}{Re_L^{0.58} - 0.80} \quad \text{for } 5 < Re_L < 2 \cdot 10^4 \quad (3.21)$$

For a flat perpendicular to the flow, different regimes will be present as well. These include Stokes flow at very low Reynolds numbers, to steady separation, to systematic Karman vortices being shed periodically from the edges to a fully turbulent wake. For a fully turbulent wake with $Re_L = 10^5$, a value of 1.98 is typically used (Munson et al., 2010). For this study a series of CFD simulations with a plate normal to the flow have been carried out. These are described in Appendix A. The results are shown in Figure 3.13.

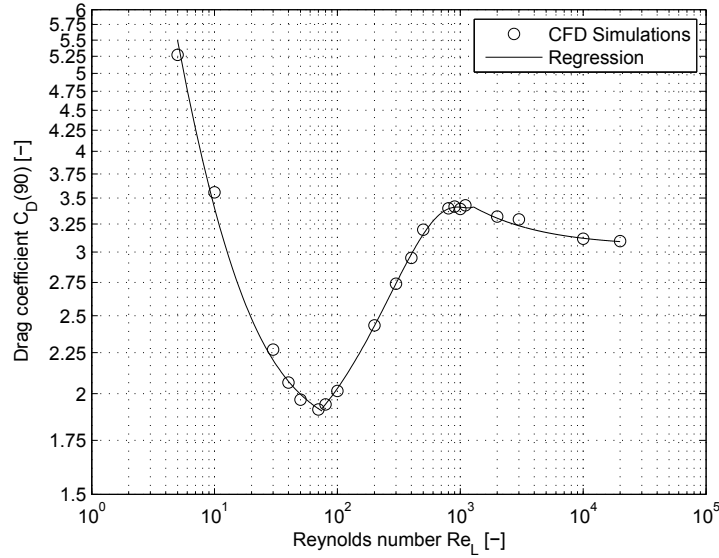


Figure 3.13. Drag coefficient for normal flow at various Reynolds numbers Re_L found by the CFD simulations presented in Appendix A.

Based on the simulations presented in the figure, the piece-wise function in Equation (3.22) describing the drag coefficient for normal flow as function of the Reynolds number is made.

$$C_D(90) = \begin{cases} 1.75 + \frac{5.0}{0.20 \cdot Re_L^{1.18}}, & \text{for } 5 < Re_L \leq 75 \\ 1.63 \cdot 10^{-9} \cdot Re_L^3 - 5.17 \cdot 10^{-6} \cdot Re_L^2 + 5.41 \cdot 10^{-3} \cdot Re_L + 1.54, & \text{for } 75 < Re_L \leq 1280 \\ 3.05 + \frac{5.0}{0.045 \cdot Re_L^{0.80}}, & \text{for } 1280 < Re_L \leq 2.0 \cdot 10^4 \end{cases} \quad (3.22)$$

Based on this subsection, the drag coefficient can be modelled using one of the blending functions in Table 3.1 with the extreme values estimated by Equation (3.21) and (3.22).

3.2.3 Lift Force

The lift force is defined as a component of the net force \vec{F}_r acting perpendicular to the relative fluid velocity. Like the drag force, the lift force can be estimated using a dimensionless coefficient taking the angle of attack and Reynolds number into account, that is $C_L = f(\alpha, Re_L)$. In general, the lift force can be determined using Equation (3.23) (Munson et al., 2010).

$$\vec{F}_L = \frac{1}{2} \rho_f \cdot L \cdot b \cdot C_L |\vec{v}| \cdot \vec{v} \quad (3.23)$$

The lift force will in this work be based on the plate length instead of the height, since $L \gg h$. A description of the lift coefficient as function of Reynolds number and the angle of attack is given in the following subsections.

Angle of Attack Dependent Lift Coefficient for Flat Plates

The lift coefficient of an object depends heavily on the angle of attack. For airfoils and flat plates, the lift coefficient is almost proportional to the angle of attack when the angle of attack

is low. When a certain angle of attack is reached the flow will separate from the plate and vortices will be shed from the trailing edge of the plate. After this point the lift coefficient will oscillate in time. A set of experiments carried out by Brunton and Rowley (2011) describes the lift coefficient as function of angle of attack at $Re_L = 100$ for a flat plate. The results of these experiments are shown in Figure 3.14.

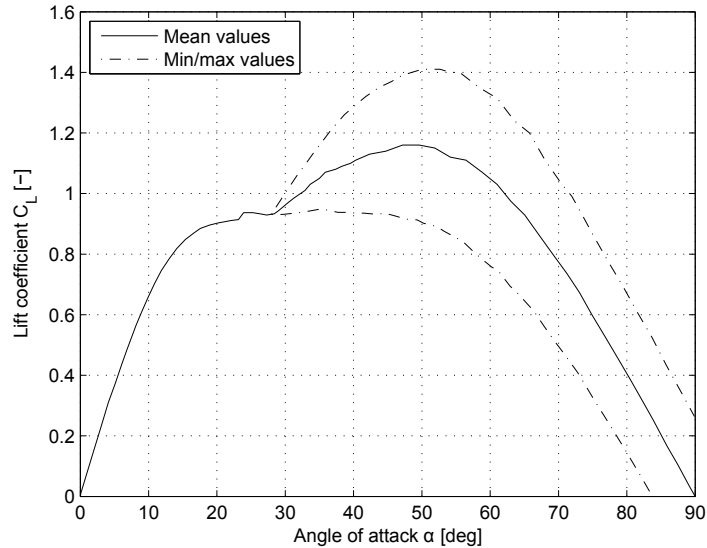


Figure 3.14. Lift coefficient as function of angle of attack for a flat plate at $Re_L = 100$ (Brunton and Rowley, 2011).

As the figure shows, the lift coefficient C_L is almost proportional to the angle of attack up to $\alpha = 15$ deg at $Re_L = 100$. At this point the plate stalls and the lift coefficient does not increase with the angle of attack until oscillations begin at around $\alpha = 30$ deg.

The model developed in the present work will be dealing with moderate Reynolds number flow with laminar boundary layer around the plate, $Re_L \approx 10^4$. As the lift coefficient depends on the Reynolds number, and Reynolds numbers exceeding 100 are expected during a free fall, some more investigations are required.

Investigation of Lift Coefficient using CFD

To estimate the lift coefficient at a Reynolds number corresponding to the Reynolds numbers expected during a free fall, a set of transient CFD simulations of a flat plate with $Re_L = 10000$ are made. These simulations are described in details in Appendix A and the results are presented in Figure 3.15, showing the lift coefficient C_L as function of Reynolds number Re_L .

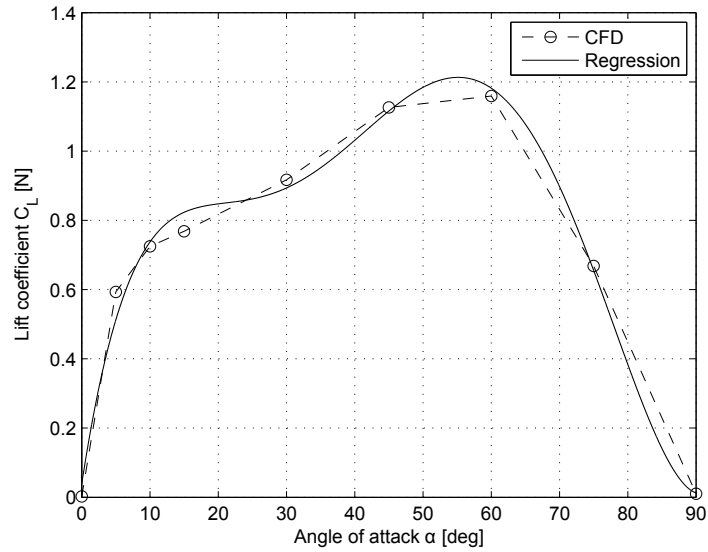


Figure 3.15. Lift coefficient as function of angle of attack for a flat plate found by CFD with $Re_L = 10000$.

Based on the results shown in Figure 3.15, the regression given in Equation (3.24) is made.

$$C_L(\alpha) = -7.076 \cdot |\alpha|^5 - 28.942 \cdot |\alpha|^4 + 41.390 \cdot |\alpha|^3 - 25.745 \cdot |\alpha|^2 + 7.390 \cdot |\alpha| + 0.03754 \quad (3.24)$$

A comparison of Figure 3.14 and Figure 3.15 shows that the shapes of the curves are very alike despite the difference in Reynolds number. Additionally, the values of the lift coefficient at all angles of attack are very similar. Therefore it is assumed that the regression in Equation (3.24) can be used to predict the lift coefficient at various angles of attack and different Reynolds numbers.

3.2.4 Added Mass Force

Since the plate is free to fall and experiences secondary side way motion, the plate will accelerate and decelerate throughout its fall. When the plate is accelerated, the surrounding fluid will be accelerated as well. The result is an added mass force (also known as virtual mass force) damping the instantaneous plate accelerations as the plate accelerates some mass of the surrounding fluid as well (Brennen, 1982). An example of an accelerating plate accelerating a volume of surround fluid to a certain degree is shown in Figure 3.16.

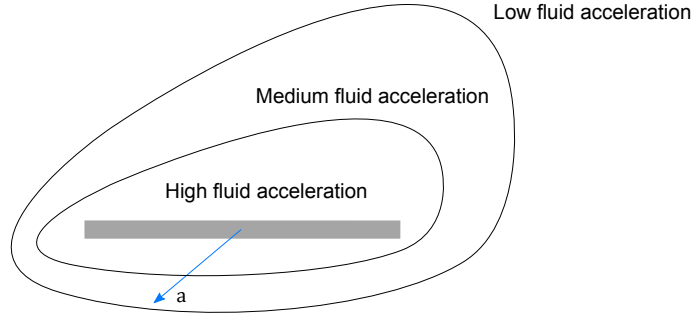


Figure 3.16. Sketch showing a volume of surrounding fluid being accelerated when the plate is accelerated with \vec{a} .

As the figure shows, the surrounding fluid will be accelerated at various degrees depending on the location around the plate. In general, the added mass force for an arbitrary shaped object can be determined from Equation (3.25), where m_a denotes the mass of the fluid being accelerated with the plate (Simcik et al., 2008).

$$\vec{F}_a = -m_a \frac{d\vec{v}}{dt} \quad (3.25)$$

As one might expect, the mass of fluid being accelerated depends on several factors including the density of the fluid and the plate orientation. Therefore added mass m_a is defined as shown in Equation (3.26), where C denotes an added mass coefficient, ρ_f denotes the density of the fluid, and V denotes the volume of fluid displaced by the object.

$$m_a = C \rho_f V_p \quad (3.26)$$

A lot of research has been done estimating the value of the added mass coefficient C . This work dates back to BBO-equation describing the motion of spherical particles, where the added mass force contribution is modelled using a constant added mass coefficient of 0.5 (Green, 1995).

The General Case with Six Degrees of Freedom

Considering an arbitrary object with six degrees of freedom, a translational acceleration might both induce a force contribution as well as a torque contribution. One way to express all dependencies relating the translational- and angular accelerations to the forces and torques, is to express the added mass as a 6×6 added mass matrix \vec{M} . In this case, a combination of Equation (3.25) and Equation (3.26) becomes Equation (3.27) (Brennen, 1982).

$$\begin{bmatrix} F_{a,x'} \\ F_{a,y'} \\ F_{a,z'} \\ T_{a,x'} \\ T_{a,y'} \\ T_{a,z'} \end{bmatrix} = \begin{bmatrix} M_{11} & M_{12} & \cdots & M_{16} \\ M_{21} & M_{22} & \cdots & M_{26} \\ \vdots & \vdots & \ddots & \vdots \\ M_{61} & M_{62} & \cdots & M_{66} \end{bmatrix} \begin{bmatrix} a_{x'} \\ a_{y'} \\ a_{z'} \\ \dot{\omega}_x \\ \dot{\omega}_y \\ \dot{\omega}_z \end{bmatrix} \quad (3.27)$$

The following subsection describes how such a matrix can be determined for the specific plate considered in this work. Note some coefficients describe an added moment of inertia rather than an actual mass.

Determination of Added Mass Coefficient Matrix for the Flat Plate using CFD

When a flat plate in two dimensions is considered, some simplifications of the \bar{M} matrix can be made. For a two-dimensional object, the matrix is reduced to a 3×3 matrix. Furthermore for flat plates with three axis of symmetry, the matrix becomes purely diagonal, resulting in only three unknown coefficients (Brennen, 1982). Therefore the added mass coefficient matrix to be determined in this work is given by Equation (3.28), where $M_{11} = C_{11}\rho_f V$, $M_{22} = C_{22}\rho_f V$, and $M_{66} = C_{66}I_{z',f}$.

$$\begin{bmatrix} F_{a,x'} \\ F_{a,y'} \\ T_{a,z'} \end{bmatrix} = \begin{bmatrix} M_{11} & 0 & 0 \\ 0 & M_{22} & 0 \\ 0 & 0 & M_{66} \end{bmatrix} \begin{bmatrix} a_{x'} \\ a_{y'} \\ \dot{\omega}_z \end{bmatrix} \quad (3.28)$$

These three coefficients are determined using CFD simulations of the exact plate considered in this work. One approach is to simulate the motion of a plate from rest using very small time scales. When such small time scales are considered, the force contributions which are a function of the velocity, such as lift and drag, can be neglected even though the drag coefficient is expected to be high (Simcik et al., 2008). By applying a well-defined force or torque and tracking the motion of the plate, the contribution from added mass effects can be determined. This approach of using small initial time scales has been used successfully by Simcik et al. (2008) and (Simcik and Ruzicka, 2013) to numerically validate the added mass coefficient for a sphere $C = 0.5$, where an analytical solution is known.

How these simulations are configured in this work is described in details in Appendix B. The added mass coefficient matrix found by the simulations is given by Equation (3.29).

$$\bar{C} = \begin{bmatrix} \frac{M_{11}}{\rho_f V} & 0 & 0 \\ 0 & \frac{M_{22}}{\rho_f V} & 0 \\ 0 & 0 & \frac{M_{66}}{I_{z',f}} \end{bmatrix} = \begin{bmatrix} 0.0731 & 0 & 0 \\ 0 & 17.3 & 0 \\ 0 & 0 & 7.03 \end{bmatrix} \quad (3.29)$$

As the matrix in Equation (3.29) shows, the coefficients C_{11} and C_{22} are not equal, which would be the case for a perfect sphere. The coefficient C_{11} is lower than C_{22} as expected, corresponding to a plate accelerated parallel to its long axis has a lower added mass.

In the following, details on the history force will be given.

3.2.5 History Force

When a flat plate is accelerated parallel to its long side, there will be a time delay in the boundary layer build-up. This delay causes an additional force contribution commonly known as the history force (or Basset force). Figure 3.17 shows a sketch of the boundary layer build-up over a flat plate suddenly being accelerated to a certain velocity from rest.

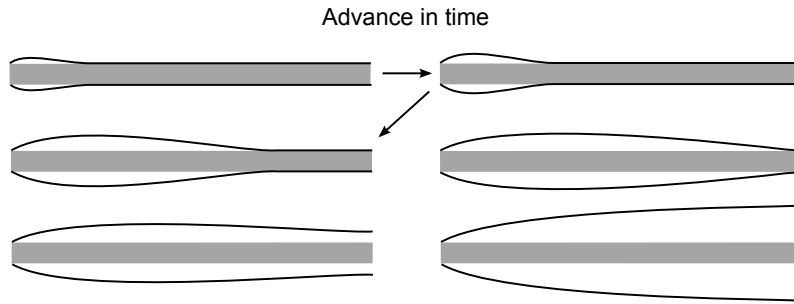


Figure 3.17. Sketch showing a delay in boundary layer build-up when a plate is suddenly being accelerated to a certain velocity.

Since the wall shear stresses are directly related to the velocity gradient normal to the plate, a delay in boundary layer build-up will cause a delay in wall shear stresses and therefore viscous force. In order to investigate the history force a series of CFD simulations have been carried out, where a flat plate orientated parallel to the direction of movement is accelerated and then decelerated. These simulations are described in details in Appendix C.

In the following the results of the simulations are presented to show the importance of the history force. Figure 3.18 shows the viscous force on a flat plate being accelerated from rest at $\vec{a} = 5.0 \text{ m/s}^2$ and $\vec{a} = 7.5 \text{ m/s}^2$ for 0.1 s and 0.667 s respectively resulting in constant velocities of 0.5 m/s.

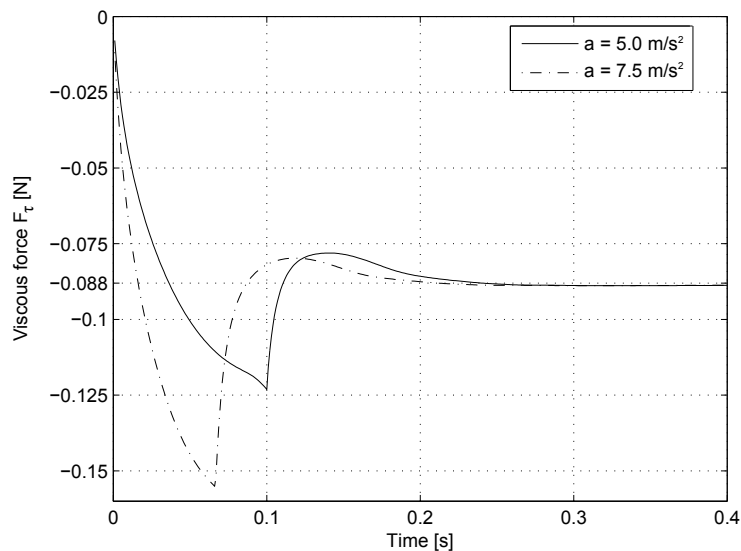


Figure 3.18. Delay in boundary layer build-up causes the viscous force to be delayed as well. The plate is accelerated to constant velocities of 0.5 m/s resulting in $Re_l = 20000$.

As seen in the figure, the viscous force peaks at different values depending on the acceleration. When the plate translates at constant velocities from $t = 0.1 \text{ s}$ and $t = 0.667 \text{ s}$, there is a delay until the boundary layer becomes stationary in time at $F_\tau = -0.088 \text{ N}$.

Likewise, for a plate moving at a constant velocity suddenly being decelerated and being

brought to a halt, there will be a delay in time before the viscous force reaches zero, since the surrounding fluid will continue past the plate. Figure 3.19 shows the viscous force as function of time for a plate begin brought to halt by accelerations $a = -5.0 \text{ m/s}^2$ and $a = -7.5 \text{ m/s}^2$.

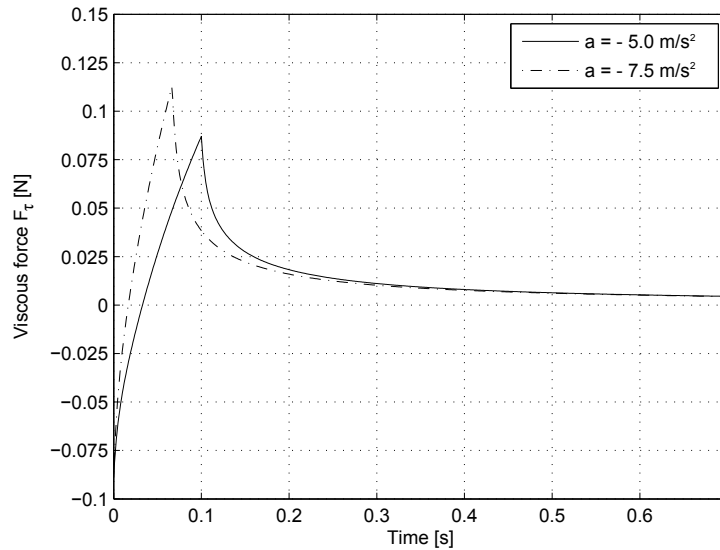


Figure 3.19. The fluid surrounding the plate continues as the plate is brought to a halt, causing the viscous force to slowly decrease towards zero.

As the figure shows, the fluid continues past the plate and results in a positive viscous force as expected. As the above figures show, the viscous force is highly time dependent and even though attempts to describe the history force dates back to the BBO-equation, no general model has yet been proposed. The importance of the history force in relation to flat plates in free fall will be investigated by visualisation of the CFD simulations presented in Chapter 6.

3.2.6 Buoyancy Force

When an object is immersed in a fluid with different density, there will be a resultant force acting on the object, commonly denoted buoyancy force. This conservative force is due the variation of pressure with the depth. The resulting buoyancy force can be determined by integrating the hydrostatic pressure field around a plate as given by Equation (3.30) (Cengel et al., 2008).

$$\vec{F}_b = \int p_h d\vec{A} \quad (3.30)$$

Figure 3.20 gives an overview of how the hydrostatic pressure distribution varies around a plate at rest and Figure 3.21 shows the sum of the forces on each side of the plate.

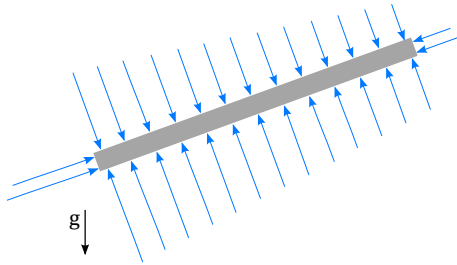


Figure 3.20. Buoyancy explained by the pressure in a fluid increasing with depth.

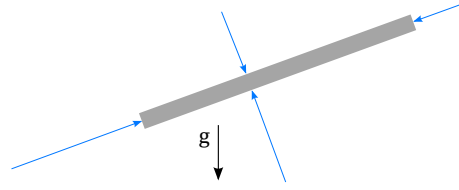


Figure 3.21. Sum of the forces acting on each side of the plate. The resulting force in the x-direction is always zero.

When the four resulting forces in Figure 3.21 are summed up, the result is an upward pointing force. As seen in the Figure 3.21 the resulting force will not act through the centre of gravity but at a distance away from the centre of gravity. The result is a net force contribution which will be further described in Subsection 3.3.4.

When the hydrostatic pressure distribution around the plate is integrated as shown in Equation (3.30), the result is an upward pointing force proportional to the mass of fluid displaced by the object and independent on the orientation of the plate. This is as given by Equation (3.31).

$$\vec{F}_b = -V_p \rho_f \vec{g} \quad (3.31)$$

3.2.7 Gravity Force

The gravity force will be modelled using a constant gravitational acceleration as shown in Equation (3.32). The gravitational acceleration is constant at all times and hence it will be considered a conservative force.

$$\vec{F}_g = m \vec{g} \quad (3.32)$$

The above mentioned force contributions will be used to find the translational acceleration based on Equation (3.1). Since some of the forces act in a point different from the centre of gravity, there will be a resultant torque causing an angular acceleration. The various torque contributions are described in the following.

3.3 Physical Mechanisms Resulting in Torque Contributions

The following section describes the different torque contributions to T_z used in Equation (3.5) to update both the rotational velocity and orientation of the plate. The contributions to the total net torque on a flat plate in free fall are assumed to consist of the following:

- Torque due to rotational resistance \vec{T}_{resist} caused by the plate rotating in a non-rotating fluid. The result is a damping net torque trying to decelerate the rotation of the plate. A detailed explanation of this phenomenon as well as a modelling strategy are given in Section 3.3.2.

- Torque due to the centre of pressure off-set \vec{T}_o for the aerodynamic forces caused by a non symmetrical pressure distribution around the plate. The result is the aerodynamic forces acting through the centre of pressure rather than the centre of gravity, which leads to a new torque. This contribution and its modelling strategy is explained in details in Subsection 3.3.3.
- Torque due to buoyancy force off-set \vec{T}_b caused by the hydrostatic pressure distribution around the plate. The result is a torque contribution from the buoyancy force, which depends on the orientation of the plate.

3.3.1 Net Torque on Plate in Free Fall

Instead of using a single centre of pressure location for all the different force contributions, they will be grouped into different categories having their own centre of pressure location. The aerodynamic forces such as lift and drag will be given the same centre of pressure location, described in Section 3.3.3, while the buoyancy force has another centre of pressure location described in Section 3.3.4. This approach is convenient as it allows a more detailed description and modelling strategy of the different torque contributions.

Furthermore, there will be a damping torque trying to stop the motion of a rotating plate. This torque contribution is explained in the following.

3.3.2 Rotational Resistance Torque

When the plate rotates in a fluid which does not rotate with the same angular velocity, the result is a torque contribution acting in the opposite direction of the plate rotation. This is illustrated in Figure 3.22, where the blue arrows show the fluid velocity experienced by the plate when it rotates in a stagnant fluid.

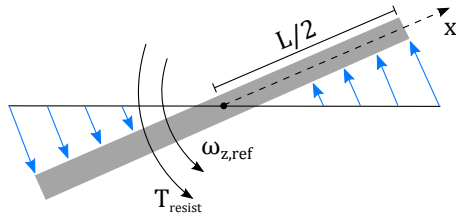


Figure 3.22. Torque due to resistance caused by difference in angular velocity of plate $\omega_{z,p}$ and fluid $\omega_{z,f}$ resulting in $\omega_{z,ref}$.

The forces on the plate due to the difference in angular velocity of plate and fluid are used to determine the torque due to rotational resistance \vec{T}_{resist} . To evaluate the torque due to resistance, the resistance forces are integrated along the length of the plate L . Assuming a symmetrical velocity field around the plate, the integral from 0 to $L/2$ only depends on distance from centre of the plate and in this case it can be written as shown in Equation (3.33) (Rosendahl, 2000).

$$\vec{T}_{resist} = 2 \int_0^{L/2} \vec{F}_{resist} dx' \quad (3.33)$$

The resistance force \vec{F}_{resist} used in Equation (3.33) can be estimated using a simple drag coefficient $C_{D,r}$. Thereby, Equation (3.33) can be rewritten as shown in Equation (3.34).

$$\vec{F}_{\text{resist}} = \frac{1}{2} \rho_f \cdot x' \cdot b \cdot C_{D,r} |\omega \cdot x'| \cdot \omega \cdot x' \quad (3.34)$$

Carrying out the integral in Equation (3.33) with the resistance force given by Equation (3.34), one obtains the expression given by Equation (3.35).

$$\vec{T}_{\text{resist}} = -\rho_f C_{D,r} |\omega| \omega \frac{1}{4} \left(\frac{L}{2}\right)^4 \quad (3.35)$$

In order to successfully utilise Equation (3.35) to model the torque due to resistance, an estimate on the drag coefficient has to be made. The drag coefficient depends on the velocity of the fluid experienced by the plate as it rotates. Since this velocity increases proportional to the distance from the centre of gravity of the plate, estimating the drag coefficient is not trivial. Moreover, fluid will pass the edge of the plate. This is expected to result in a lower local drag coefficient near the edges of the plate. For simplicity a single constant value of $C_{D,r}$ is used to estimate the torque due to resistance. a rough initial guess of $C_{D,r} = 2$ is used. This initial guess will be examined in a sensitivity analysis in Appendix D.

3.3.3 Torque Contribution from Aerodynamic Forces

When a plate is free to fall, the flow field around the plate changes throughout its fall. As the flow field around the plate is not symmetrical, the result will be the lift and drag forces not acting through the centre of gravity. Instead the drag and lift force will act through a centre of pressure. The distance between the centre of gravity and centre of pressure will be denoted cp_o . The result of a non-coincident centre of gravity and centre of pressure location is a torque trying to stabilise the plate perpendicular to the relative fluid velocity. In general, the torque contribution due to the aerodynamic forces acting through the centre of pressure can be calculated by a cross-product between a vector describing the centre of pressure location \vec{cp}_o and the sum of the aerodynamic forces $\vec{F}_D + \vec{F}_L$. This is as given by Equation (3.36).

$$\vec{T}_o = \vec{cp}_o \times (\vec{F}_D + \vec{F}_L) \quad (3.36)$$

The centre of pressure location \vec{cp}_o is typically assumed to be a function of the angle of attack α (Mandø and Rosendahl, 2010). The centre of pressure location for different plate orientations is shown in Figure 3.23.

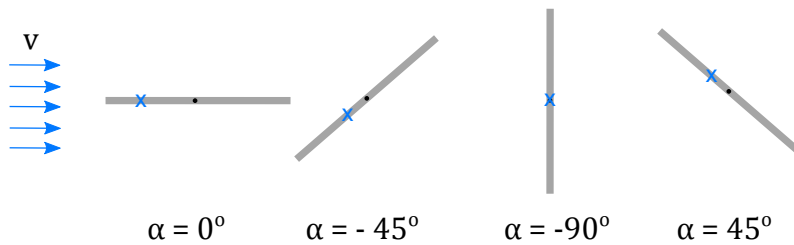


Figure 3.23. Centre of pressure location for different angles of attack α for a constant relative fluid velocity \vec{v} .

The centre of pressure location is of prime interest, when the motion of a plate in free fall is to be modelled. As the moment caused by forces not acting in the centre of gravity is

proportional to the distance between the centre of gravity and centre of pressure, this distance is important. For airfoils with angles of attack below the stall point, the centre of pressure location remains almost constant at a distance of $L/4$ away from the centre of gravity. For flat plates the blunt leading is expected to provoke separation much earlier. As separation causes a delay in boundary layer build-up, the centre of pressure is expected to be moved closer to the centre of gravity than for an airfoil. If this is actually the case will be investigated in details in Section 7.3 on page 78.

Instead of integrating the pressure field and wall shear stresses around the plate, correlations are used to estimate the centre of pressure location.

Estimating the Centre of Pressure Location Using Correlations

Numerous attempts have been done trying to estimate the centre of pressure location as function of the angle of attack for various non-spherical objects. To the authors knowledge, no such correlations have been suggested for flat plates in literature. Therefore, a set of such correlations for cylinders are presented in Table 3.2 to give an idea of such correlations.

Table 3.2. Different correlations found in literature to describe the centre of pressure location cp_o for the aerodynamic forces as function of the angle of attack α .

Function	Applied to	Author
$cp_o/L = (90 - \alpha)/480$	Cylinders	Marchildon et al. (1964)
$cp_o/L = 0.25(1 - \sin^3 \alpha)$	Cylinders	Rosendahl (2000)
$cp_o/L = 0.25\cos^3(\alpha)$	Cylinders	Yin et al. (2003)

The correlations presented in Table 3.2 are visualised in Figure 3.24.

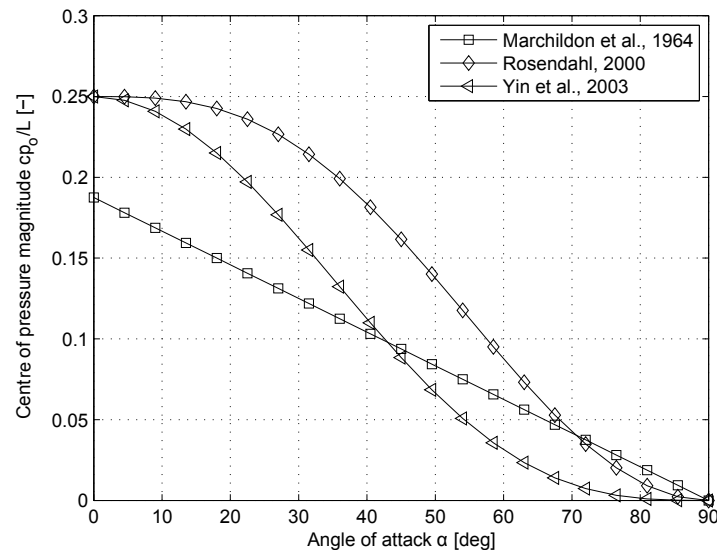


Figure 3.24. Correlations found in literature to describe the centre of pressure location as function of the angle of attack (Marchildon et al., 1964)(Rosendahl, 2000)(Yin et al., 2003).

As the figure shows, the correlations suggest a maximum value of cp_o/L in the range 0.19 to 0.25. This is in good agreement with general airfoil theory, suggesting the centre of pressure to be located at around $cp_o/L = 0.25$ (Houghton and Carpenter, 2003). It is however of interest to investigate and develop a such correlation for a flat plate specifically. Furthermore, the validity of such a correlation, and if the centre of pressure location can be described by angle of attack of alone is of interest. How such a correlation is developed is described in details in Section 7.3 in Chapter 7.

The correlations for cp_o/L only gives the absolute distance between the centre of gravity and the centre of pressure. When this is to be implemented in the model, a vector taking the actual location into account is convenient. How such a vector notation is implemented to determine the centre of pressure location in the global coordinate system following the plate is described in details in Appendix E by a piece of MATLAB code.

The following subsection gives a detailed description of the torque contribution due to the buoyancy force not acting through the centre of gravity.

3.3.4 Torque Contribution from Buoyancy

As the hydrostatic pressure varies with depth in a fluid, an inclined plate will experience a net torque \vec{T}_b trying to stabilise the plate to its horizontal position (Munson et al., 2010). This is as shown in Figure 3.25.

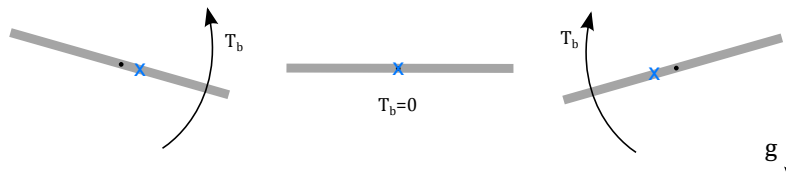


Figure 3.25. Torque contribution from buoyancy trying to stabilise the plate to its horizontal position.

This torque contribution mainly depends on the plate orientation angle θ for a specific plate falling in a specific fluid. A simple numerical model has been developed with the purpose of investigating the centre of pressure location due to buoyancy. The centre of pressure for an arbitrarily shaped object can be calculated based on Equation (3.37) taking only the hydrostatic pressure distribution around the object into account.

$$cp_{b,x'} = \frac{\int x' \cdot p_h(x') dx'}{\int p_h(x') dx'} \quad (3.37)$$

A script taking the plate dimensions, surrounding fluid density, gravitational acceleration, and a reference pressure as input and returns the centre of pressure location for buoyancy $cp_{b,x'}$ in the local coordinate system ($x'-y'$) is given in Enclosure C. Figure 3.26 presents a set of results of the script, where the plate is submerged in water at different depths, where the reference pressure at the surface is atmospheric.

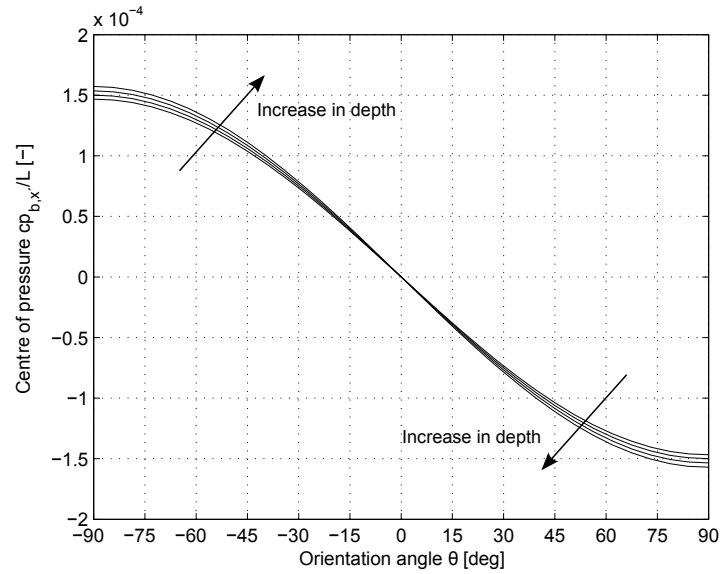


Figure 3.26. Centre of pressure for buoyancy force in the local coordinate system $cp_{b,x}$ as function orientation angle θ and depth in water. The four curves in the figure correspond to the plate being submerged 0.25 m, 0.50 m, 0.75 m, and 1.0 m.

The results in the figure suggests the centre of pressure to be approximately $1.5 \cdot 10^{-4} \cdot L$. This contribution to the total net torque is expected to be negligible and therefore this contribution is not included in the model.

3.4 Procedure of Model

This section gives a description of the modelling procedure used in the quasi-steady 2D model developed based on the theory described in this chapter. In general, the procedure can be described by the following successive steps:

- First step of the model is to specify plate dimensions and properties of plate and fluid. Furthermore the initial position and orientation of the plate as well as translational and angular velocities are specified. Initialise the time as $t = 0$ s.
- Determine the angle of attack α by Equation (3.13) with the relative fluid velocity angle φ given by Equation (3.11).
- Calculate the different force contributions acting on the plate. The drag force is calculated by Equation (3.19) with the drag coefficient given one of the blending functions presented in Table (3.1). The extreme values of the drag coefficient are found by Equation (3.12) for $C_D(0)$ and Equation (3.13) for $C_D(90)$. Calculate the lift force based on Equation (3.23) with the lift coefficient given by Equation (3.15). Calculate the added mass force by Equation (3.25) with the added mass given by Equation (3.26) and the added mass coefficient matrix given by Equation (3.29). Furthermore, calculate the buoyancy and gravity forces based on Equation (3.31) and Equation (3.32) respectively.
- Find the centre of pressure for the aerodynamic forces cp_o based on a correlation such as those presented in Table 3.2. Furthermore, the position of cp_o in the global coordinate system is found by the script presented in Appendix E based on the relative fluid velocity.

- Calculate the torque due to resistance by Equation (3.35) and the torque due to off-set of the aerodynamic forces by Equation (3.36).
- Calculate the translational and rotational acceleration of the plate by Equation (3.1) and Equation (3.5) respectively. Update the translational and rotational velocities and positions based on an appropriate numerical scheme. For this project a simple first order Euler method is used.
- Check if stopping criterion is reached. If not, advance in time and repeat - otherwise stop.

In order to visualise the procedure just described, Figure 3.27 is used.

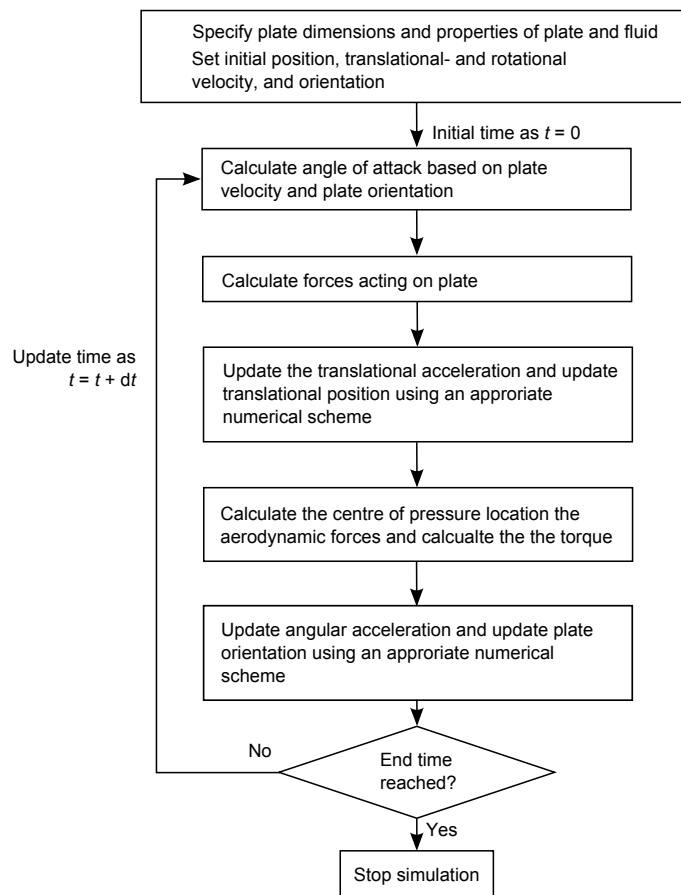


Figure 3.27. Block diagram of model structure.

The following section describes the limitations of the quasi-steady 2D model.

3.5 Limitation of Quasi-steady 2D model

As the quasi-steady 2D model relies on empirical correlations to describe the different force and torque contributions, the model has some limitations. Some of these limitations and the validity of these are described and discussed in the following.

3.5.1 Interference with Vortices Shed back in Time

As a plate is let free to fall in a stagnant fluid, the trajectory path will typically not intersect. When the plate glides almost parallel to the chord during the free fall, the plate is not expected to interfere with its own wake. In the turning points where the plate changes direction of motion, the plate will interfere with its own wake, causing the surround fluid velocity \vec{w} not to be zero even for a stagnant fluid. This phenomenon has not been included in the quasi-steady 2D model, and the exact importance remains unknown until now. Other studies such as Pesavento (2006) do however suggest, that these effects are of minor importance to the overall fall trajectory. It will be investigated in Section 7.4 using CFD results obtained by free fall simulations.

3.5.2 Saffman's Lift Force Due to Shear Velocity Field

Throughout the chapter, the relative fluid velocity has been assumed constant in time. That is, the model does not handle shear velocity fields such as the one sketched in Figure 3.28.



Figure 3.28. Shear in the velocity field around the plate.

For the case of a spherical particle, this lift force contribution is well understood and models are readily available (Saffman, 1965). Spheres will experience a lift force lifting the particle towards the higher velocity field. For other non-spherical particles things get more complicated and the direction of the lift force depends on the orientation of the particle. One such type of particle is bubbles which can deform. As the bubble size increases, the non-symmetrical wake causes the direction of the lift force to change towards the lower flow velocity side (Tomiyama et al., 1995).

For plates with aspect ratios close to unity the lift force is expected to act towards the higher velocity similar to the case of a sphere. However, when the aspect ratio of the plate increases, the lift force might change sign as it is the case for deformed bubbles. In the current work the surrounding fluid is stagnant and therefore Saffman's lift force will not be present. Expanding the model to include moving fluid with possible shear requires further work on the importance of this force for flat plates in free fall. This is out of the scope of the present work.

3.5.3 Magnus Lift Force Due to Heavy Rotational Motion

For plates falling in the tumbling motion regime, a lift contribution is expected. This contribution can be explained by the fluid moving with higher velocity on one side of the plate as shown in Figure 3.29.

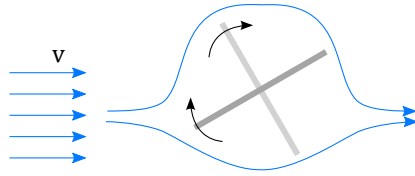


Figure 3.29. Magnus lift force due to heavy rotation of the plate.

The result is a local pressure drop on the side with the faster moving fluid resulting in a lift force in that direction. This force contribution is assumed to be especially important for auto-rotating plates in the tumbling motion regime. As long as the plate has a side-to-side way motion, this lift contribution is assumed not to be of major importance.

This chapter has been dealing with state of the art knowledge on modelling the motion of flat plates in free fall. References have been made to the CFD simulations in the appendices which have contributed to the model. The results of the model framework presented so far are presented in Chapter 7. To further expand and investigate the validity of the model, detailed CFD simulations of a plate in free fall are carried out and validated afterwards by experiments. In the two following chapters the free fall CFD simulations and the experiment are explained in details.

Chapter 4

Numerical Simulations of Freely Falling Flat Plates using Computational Fluid Dynamics

This chapter describes how CFD simulations are configured in order to simulate the free fall of a flat plate in two dimensions. The trajectory of interest can be sketched as shown in Figure 4.1.

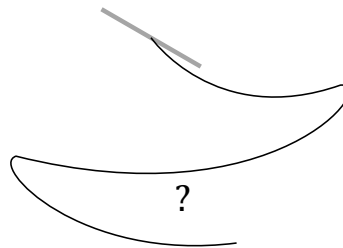


Figure 4.1. Free fall trajectory of two-dimensional plate to be determined using CFD simulations.

To model the free fall with high accuracy, a series of considerations on overall mesh topology, dynamic mesh settings, boundary layer mesh, and turbulence are made. These considerations are based on guidelines found in literature and general CFD theory. Additionally, grid-, domain- and time step independence analyses will be carried out to further ensure reliable results.

The plate simulated is made of aluminium with a density of 2700 kg/m^3 , a length of 40 mm, and a height of 2 mm.

4.1 Overall Mesh Topology

The mesh is divided into the two following zones:

- A dynamic zone where the cells are deformed and re-meshed as the plate moves.
- A non-deforming mesh zone following the motion of the plate at all times.

The pressure field near the surface of the plate is important to determine the forces on the plate as well as the centre of pressure location with high accuracy. Therefore, it is important that the mesh close to the plate is of high quality. This is ensured by a non-deforming mesh zone close to the plate, which follows the plate as it moves. Inside this zone a structured mesh consisting of quadrilateral cells is used.

Outside this region the mesh is unstructured and consists of triangular cells. This type of mesh works particularly well when the mesh is to deform and re-mesh. Figure 4.2 shows the mesh in the region near the plate as well as a small part of the unstructured mesh in the far field region. More details on the two mesh zones are presented in the following subsections.

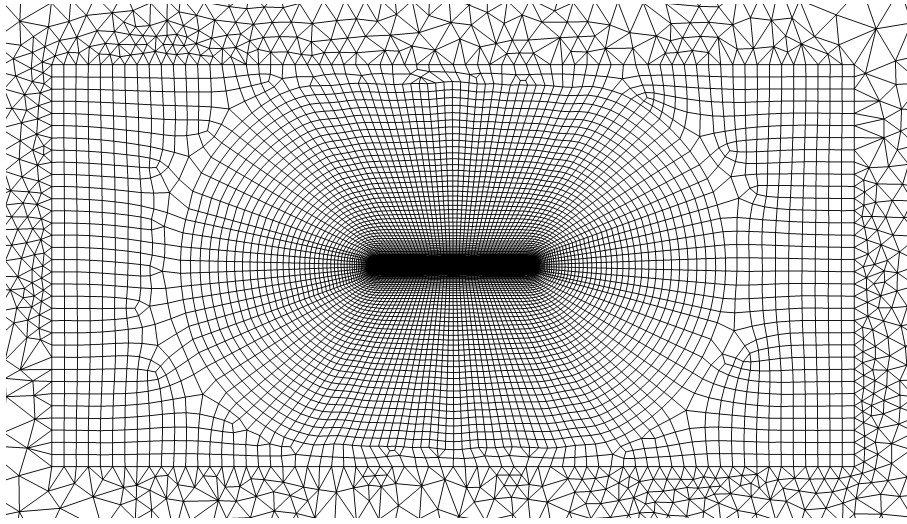


Figure 4.2. Overview of the mesh topology used near the plate and in the far field region away from the plate. The region with quadrilateral elements near the plate follows the plate at all times while the triangular elements away from the plate are re-arranged and re-meshed.

In the mesh shown above, the zone with quadrilateral elements contain 8472 elements. An analysis carried out to investigate if this number is sufficient is given in Section 4.5.

4.1.1 Dynamic Mesh Zone

Since the plate will be moving in time, the mesh must be updated automatically throughout the simulation. This is accomplished by creating a dynamic mesh with cells allowed to deform and re-mesh, when certain deformation criteria are reached. For the simulations presented in this work the following three re-meshing criteria are used:

- maximum cell length
- minimum cell length
- maximum equiangular skewness

The equiangular skewness is a measure of cell quality based on the angles in the cell. It is defined as shown in Equation (4.1), where $\theta_e = 120$ deg for triangles and θ_{\max} denotes the maximum angle in a given cell (ANSYS, Inc., 2011c).

$$\text{cell equiangular skew} = \max \left[\frac{\theta_{\max} - \theta_e}{180 \text{ deg} - \theta_e}, \frac{\theta_e - \theta_{\min}}{\theta_e} \right] \quad (4.1)$$

An example of how cells are deformed and re-meshed is shown in Figure 4.3.

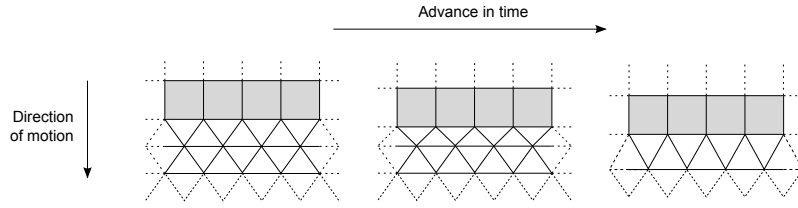


Figure 4.3. Sketch of how a deformed mesh is dynamically updated based on equiangular skewness, minimum cell length, and maximum cell length.

For the simulations presented in this work, the minimum and maximum cell lengths are chosen to be just below and just above the minimum and maximum cell length in the initial dynamic part of the mesh. Furthermore, a maximum cell equi angular skewness of 0.6 is chosen. Using too strict criteria results in unnecessary re-meshing and therefore higher computational time, while too low criteria can result in divergence since the cells might overlap when updated between two time steps. More details on the settings for the dynamic mesh and theory on the chosen methods for updating the mesh are given in Appendix F.

In the following, details on the non-deforming mesh close to the plate are presented.

4.1.2 Non-deforming Boundary Layer Mesh

A resolved boundary layer is important to capture the detailed flow phenomena close to the surface of the plate. Instead of relying on wall functions to model the flow field next to the plate, a fine mesh is made to capture these details directly. The first cell is placed at a wall distance corresponding to $y^+ = 1$. This is well within the viscous sublayer which extends to around $y^+ = 5$ (Versteeg and Malalasekera, 2007). The first cell height is calculated by Equation (4.2), where the friction velocity u_* is calculated by Equation (4.3).

$$\Delta y_1 = \frac{y^+ \mu}{\rho_f u_*} \quad (4.2)$$

$$u_* = \sqrt{\frac{\tau_w}{\rho_f}} \quad (4.3)$$

The wall shear stress τ_w is based on a friction drag coefficient C_f . This coefficient is used to evaluate the wall shear stress along the plate and can be estimated based on the Blasius Solution for flow over flat plates. This solution is assumed to be a good approximation to the boundary layer profile for the laminar part of the boundary layer next to the wall (Munson et al., 2010). The friction drag coefficient according to the Blasius Solution is given by Equation (4.4) (Munson et al., 2010).

$$C_f = \frac{0.664}{\sqrt{\text{Re}_x}} \quad (4.4)$$

Based on the above shown friction drag coefficient C_f , the required first cell height Δy_1 to resolve the boundary layer can be estimated. Figure 4.4 shows the required first cell height

as a function of the distance downstream the leading edge x and free stream velocity U_∞ in order to obtain $y^+ = 1$.

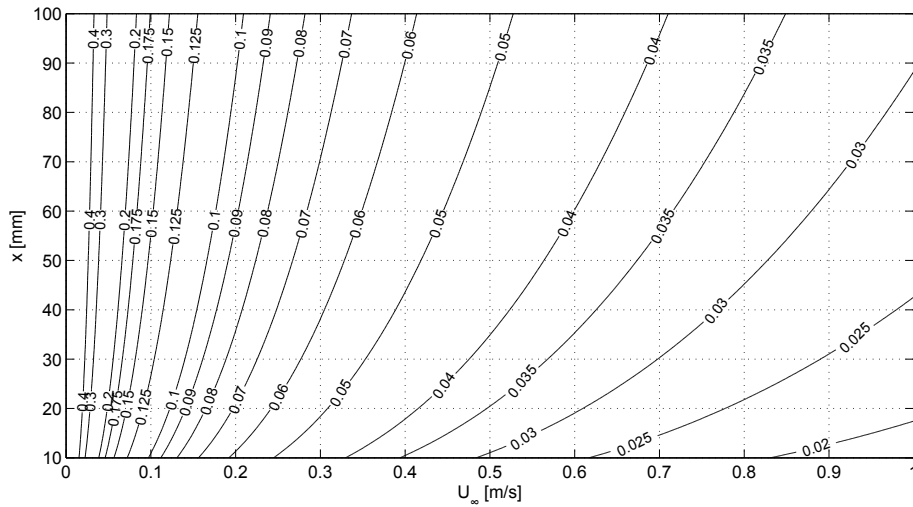


Figure 4.4. Contours showing the required height of the cell adjacent to the wall Δy_1 in millimetres in order to obtain $y^+ = 1$ as function of distance from leading edge, x , and free stream velocity U_∞ .

Since the velocity of the plate changes throughout a free fall, the thickness of the boundary layer and thereby the required first cell height Δy_1 will also change. As a rough initial guess, the first cell height is based on an apparent terminal velocity calculated by balancing out the forces and using a drag coefficient of 1.0, as suggested by Andersen et al. (2005a). The resulting terminal velocity is 0.26 m/s, which results in a first cell height $\Delta y_1 \approx 0.7$ mm to resolve the boundary layer with $y^+ = 1$ at a distance of 40 mm downstream the leading edge. The simulations presented later show y^+ -values of maximum 2, since the plate translates sideways at higher velocities than 0.26 m/s and the boundary layer is in-stationary in time and not well-described by the Blasius solution. Contour plots showing the velocity around the plate at various times are given in Section 6.2 on page 66.

To ensure a good mesh quality of the non-deforming mesh close to the plate, the equiangle skewness of the mesh should not exceed 0.5 (ANSYS, Inc., 2006). Figure 4.5 shows the equiangle skewness of this part of the mesh. Since the mesh is not deforming, the skewness will not change throughout the simulation. As indicated in the figure the maximum skewness is around 0.51, but generally in the order of 0.2. In the dynamic part of the mesh, the equiangle skew is set to a maximum of 0.6 as a re-meshing condition.

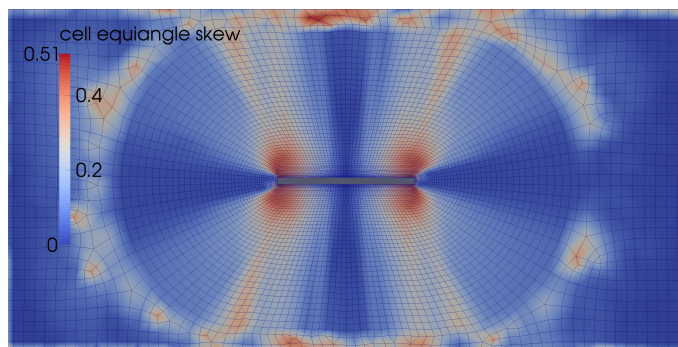


Figure 4.5. Equiangle skewness of the non-deforming mesh close to the plate

Apart from the first cell height and the mesh quality, a reasonable amount of cells in the direction perpendicular to the surface must be used. Figure 4.6 gives an overview of the mesh near the plate. A grid independence analysis to determine the required number of cells along the length and height of the plate is presented in Section 4.5.

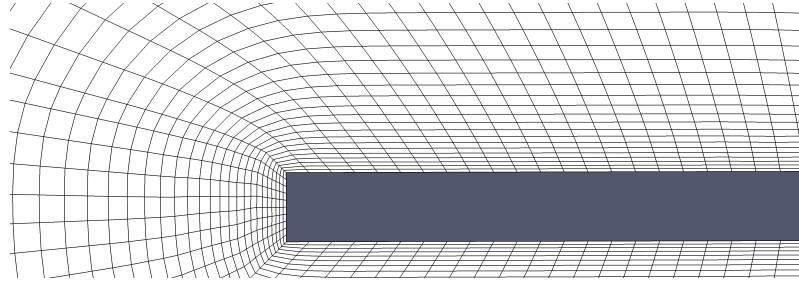


Figure 4.6. Overview of the boundary layer mesh used to model the near plate region.

The Reynolds number in the simulations will be around 10000 based on a terminal velocity of 0.26 m/s, a dynamic viscosity of $1.003 \cdot 10^{-3}$ Pa \cdot s, a density of 998.2 kg/m³, and a plate length of 40 mm. Even though the transition from laminar to turbulent boundary layer is at approximately $5 \cdot 10^5$, a turbulence model is expected to be important to model the flow correctly in the wake just behind the plate. Additionally, the blunt edges are expected to promote turbulence around the edges.

4.2 Modelling of Turbulence

Turbulence modelling is enabled in all simulations. Since flow separation is important for the pressure field around the plate, and therefore the forces acting on the plate, the ability to capture the separation is considered of uttermost importance. Best Practice Guidelines states that the SST turbulence model predicts flow separation precisely (ERCOFTAC, 2000). As large parts of the domain contain close to stagnant fluid, the turbulence model should be able to handle both laminar and turbulent flow. One such turbulence model is the SST transition turbulence model (ANSYS, Inc., 2011a). This turbulence model will be used for all the simulations presented throughout this report.

In the following section the approach used to track the plate will be described.

4.3 Degrees of Freedom

The unconfined free fall behaviour of a plate is of interest in the simulation. One approach to achieve this is to fix the plate at a point and update the boundary conditions at every time step to match calculated velocities based on the forces and torques acting on the plate. This approach has been used with success by Jin and Xu (2008) and Andersen et al. (2005a) both investigating the free fall behaviour of different objects. In the present study the well validated built-in 6DOF solver by ANSYS is used instead. This solver is capable of simulating the free fall behaviour of an object with six degrees of freedom (ANSYS, Inc., 2011b). These six degrees of freedom correspond to the plate being able to translate in three directions as well as rotate around the three axes. The two different approaches to simulate the free fall can be sketched as shown in Figure 4.7.

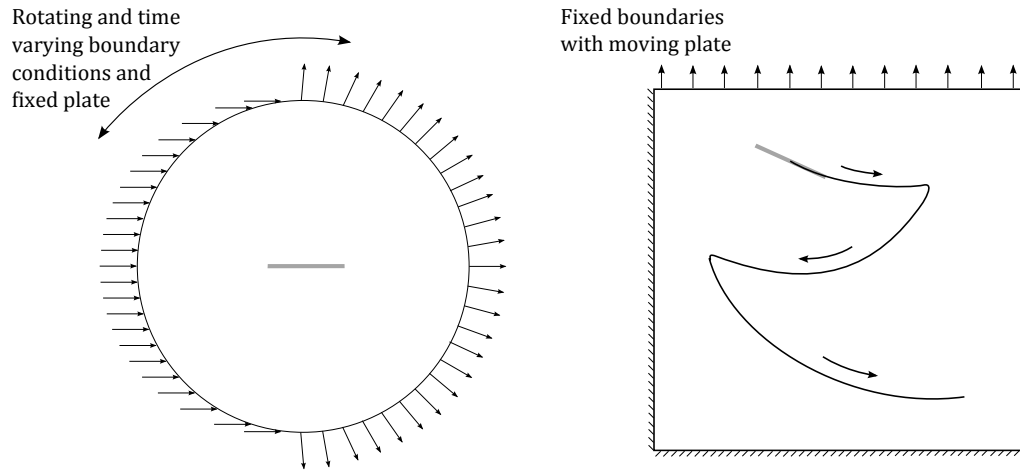


Figure 4.7. Different approaches to simulate the free fall of a flat plate in two dimensions.

The 6DOF solver generally calculates forces and moments on an object and updates translational and rotational motion accordingly (ANSYS, Inc., 2011b).

In order for the solver to calculate the translational and rotational acceleration of the plate, both the mass of the plate and the moment of inertia around the z-axis have to be passed to the solver during iterations. For the two-dimensional case, the required moment of inertia and mass of plate are calculated based on Equation (4.5) and Equation (4.6) respectively.

$$I_z = \frac{Lh\rho_p(L^2 + h^2)}{12} \quad (4.5)$$

$$m = \rho \cdot L \cdot h \cdot 1 \text{ m} \quad (4.6)$$

Furthermore, since a single phase model is used, the buoyancy force has to be included explicitly. Based on Equation (3.31) on page 32 the buoyancy force is determined to be 0.7834 N, which is added as a constant external force in the y-direction. Both the moment of inertia, mass, and buoyancy force are specified in an User Defined Function (UDF). This UDF can be found in Enclosure A. To obtain results such as viscous and pressure forces on the plate at all times during its free fall, a separate UDF for this purpose is created.

4.3.1 Extraction of Results for Moving Object

A second UDF is created to be able to get detailed results of the forces on the plate at all times. This UDF is called at the end of each time step and extracts results such as viscous, and pressure forces in both x- and y-direction and saves the results to a file. This UDF is given in Enclosure A as well.

The following section gives an overview of the computational domain and the boundary conditions used for the simulations.

4.4 Computational Domain and Boundary Conditions

Since the unconfined free fall behaviour is of interest in this study, the computational domain has to be made sufficiently large to ensure that the effects from the boundaries are negligible.

A simple rectangular domain is chosen and the plate is initially placed in the upper part of the domain. Figure 4.8 gives an overview of the domain with distances to the domain boundaries and choice of boundary conditions.

To ensure reliability of the computations, both grid, time step, and domain size independence analyses are carried out. The following section describes the grid independence analysis made to ensure the results are independent of the mesh.

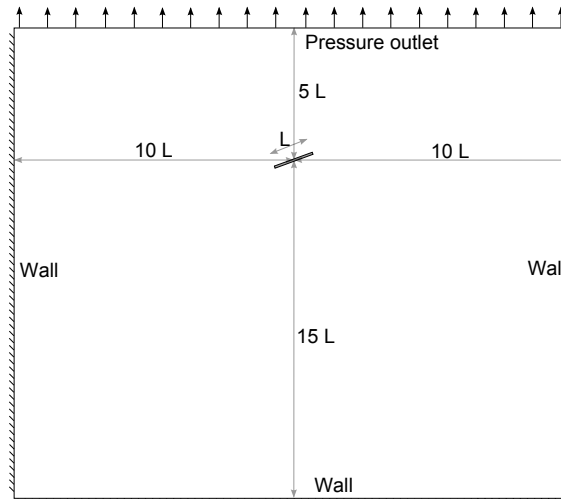


Figure 4.8. Computational domain and boundary conditions used for the free fall simulations.

4.5 Grid Independence Analysis

Initially the results of three simulations with varying fineness are analysed. The number of cells in the meshes is doubled two times from the coarsest mesh to the finest. The characteristics of the three meshes are seen in Table 4.1.

Table 4.1. Overview of the different meshes used in the initial grid independence analysis.

Parameter	Coarse	Medium	Fine
Total number of cells in domain	7601	15519	31402
First cell height near plate [mm]	0.09	0.09	0.09
Cell length along plate length [mm]	3.0	2.0	1.1
Cell length along plate height [mm]	0.5	0.5	0.33
Cell length on rotating fluid domain [mm]	8.5	6.0	4.3
Cell length in triangular section [mm]	15	10	7

The plate is dropped at an initial orientation angle θ of 10 deg. Results showing the trajectories and plate orientation as function of time are presented in Figure 4.9 and 4.10 respectively.

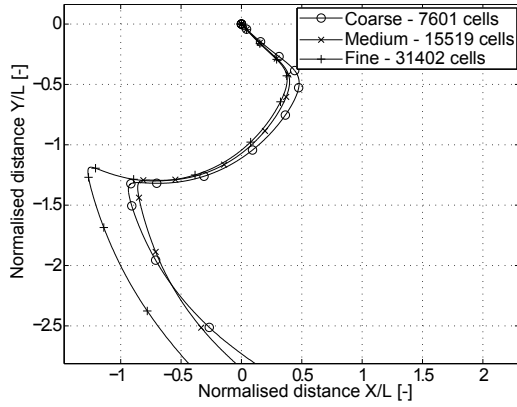


Figure 4.9. Results of trajectories for three different meshes.

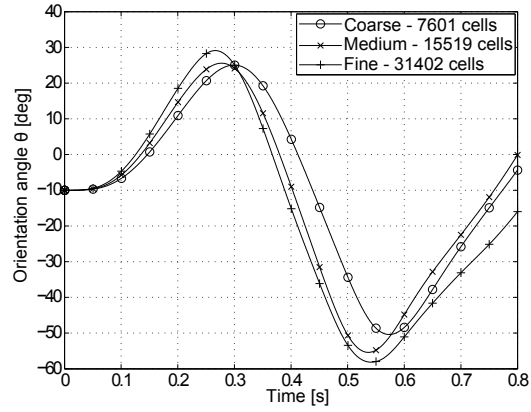


Figure 4.10. Orientation angle θ as function of time for 3 meshes.

The results suggest that the fine mesh is not sufficient to obtain grid independent results. Instead of simply doubling the number of cells and therefore increasing the computational time, the importance of the different mesh zones is investigated.

A second analysis investigates the importance of the non-deforming mesh close to the plate keeping a constant mesh size in the remaining domain. The meshes investigated in this analysis are listed in Table 4.2. Notice that the cell length in the dynamic mesh zone with triangular cells away from the plate is the same for these meshes. Note how the coarse mesh in the following table corresponds to the medium mesh in the initial analysis in Table 4.1. Furthermore, the mesh with 31402 cells in Table 4.1 has the same resolution close to the plate as the mesh with 18130 cells in Table 4.2. The only difference is the cell length in the triangular section of the mesh.

Table 4.2. Overview of the different meshes used in the second grid independence analysis.

Parameter	Coarse	Medium	Fine	Extra fine
Total number of cells in domain	15519	18130	21237	28833
First cell height near plate [mm]	0.09	0.09	0.09	0.09
Cell length along plate length [mm]	2.0	1.1	0.70	0.5
Cell length along plate height [mm]	0.5	0.33	0.20	0.15
Cell length on rotating fluid domain [mm]	6.0	4.3	3.0	2.15
Cell length in triangular section [mm]	10	10	10	10

The results of the second analysis are presented in Figure 4.11 and 4.12.

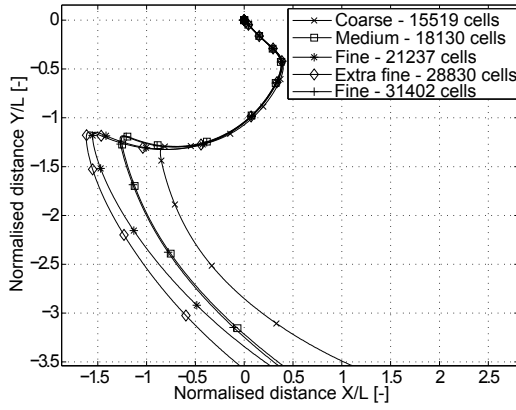


Figure 4.11. Results of trajectories for 5 different meshes.

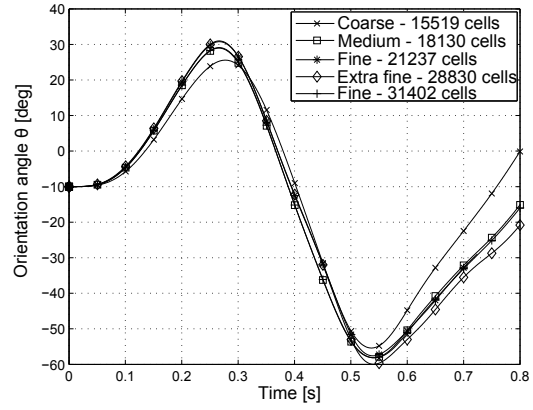


Figure 4.12. Orientation angle θ as a function of time for 5 meshes.

The results in Figure 4.11 and 4.12 show that the change in results from the mesh with 18130 cells to the mesh with 31402 cells is negligible. Therefore it is concluded that the structured mesh close to the plate is the most important part of the mesh to obtain a grid independent solution. Additionally, the results show that the mesh with 21237 cells is grid independent since the results obtained with the finer mesh with 28830 cells do not change significantly.

The following section discusses the required domain size to ensure that the solution is not influenced by the surrounding walls.

4.6 Domain Size Independence Analysis

Two different domain sizes are presented in the following. One corresponding to the one presented in Figure 4.8 and another with the total area doubled. The results in terms of trajectory and orientation angle as function of time are shown in Figure 4.13 and 4.14 respectively. The standard domain in the figures corresponds to the mesh with 21237 cells in Table 4.2. The larger domain is 28 plate lengths wide instead of the 20 plate lengths used in the standard domain.

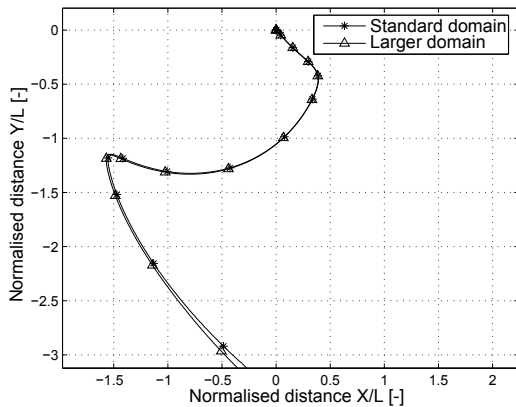


Figure 4.13. Results of trajectories for the two different domain sizes.

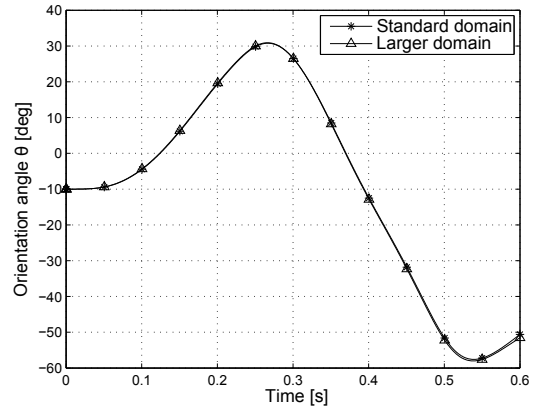


Figure 4.14. Orientation angle θ for the two different domain sizes.

As the figures indicate, doubling the domain size has no significant influence on the results. Therefore the domain presented in Figure 4.8 is used for the rest of the simulations. The

following section presents an analysis of the time step size.

4.7 Time Step Independence Analysis

The results of the simulations should not change significantly when the time step size is reduced. Therefore an analysis with three different time steps sizes with corresponding results shown in the Figure 4.15.

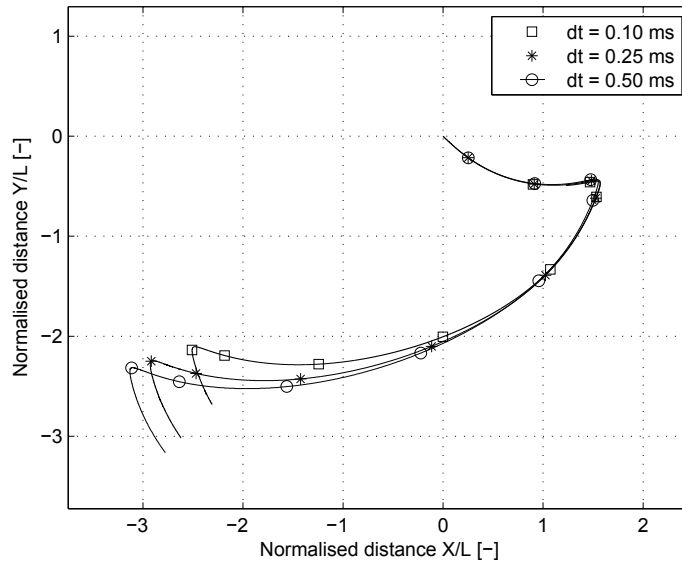


Figure 4.15. Results of trajectories with time step sizes 0.10 ms, 0.25 ms, and 0.50 ms.

The figure indicates how the trajectories differ by small amounts when the time step size is changed. Even though an analysis with even smaller time step sizes could reveal slightly different results, a time step size of 0.25 ms is chosen. This is chosen based on the experiment presented in Chapter 5, which shows a trajectory only differing by a small amount.

A parameter used as a measure for the required time step size is the Courant number. The Courant describes the local fluid movement in a time step compared to the cell size. A Courant below 1 ensures that information does not pass more cells during one time step. The Courant number can in general be calculated by Equation (4.7), where v is the flow velocity, Δt is the time step size, and Δx is the cell length (ANSYS, Inc., 2011b).

$$c = \frac{v\Delta t}{\Delta x} \quad (4.7)$$

An example of the Courant number when the plate translates at maximum velocity is given in Figure 4.16.

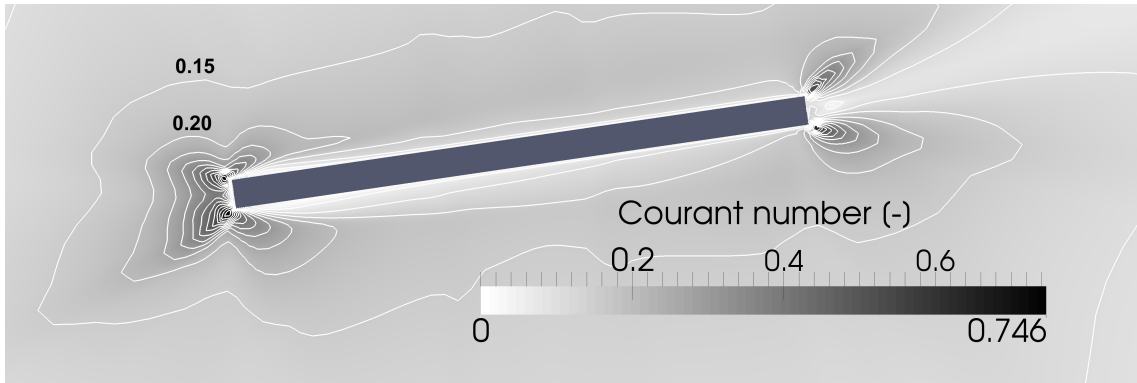


Figure 4.16. Courant number when the plates translates at high velocity. Contours show steps in Courant number of 0.05. Note how the maximum Courant number does not exceed 1.

The figure indicates that the cell Courant number does not exceed one in the mesh close to the plate when a time step size of 0.25 ms is chosen.

The following section aims to investigate the convergence within each time step in the simulations.

4.8 Convergence

To ensure reliable results, the calculated coupled velocity and pressure field has to converge to a reasonable value within each time step. To determine if the solution has converged sufficiently within each time step, the position of the plate as function of iteration number is of interest. Figure 4.17 shows the plate position as function of iteration number during the free fall. As the position is calculated based on the forces acting on the plate, this parameter is assumed to be sufficient to evaluate the required number of iterations.

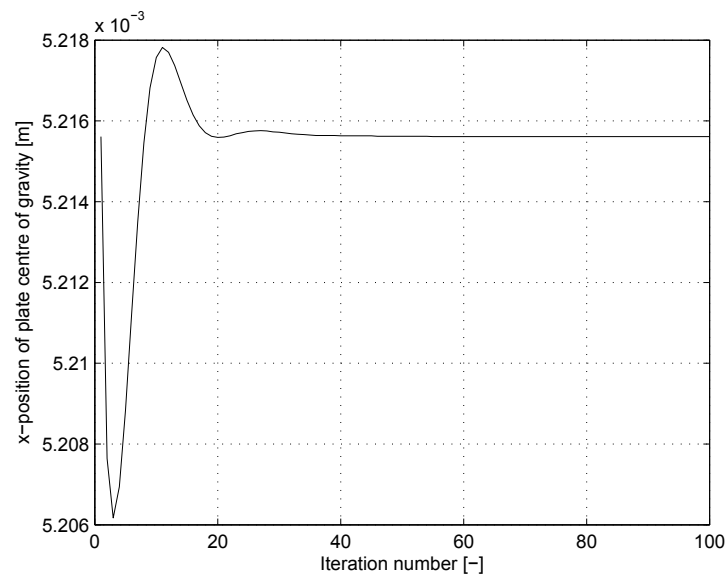


Figure 4.17. Position of plate as function of iteration number within a time step.

The figures indicates that the plate position does not change when the number of iterations is increased above 40. Even though the figure suggests 40 iterations to be sufficient, 100 iterations are used to ensure more convergent results.

Summing up, this chapter presented analyses to determine a way to configure a CFD simulation to ensure reliable results. The 6DOF solver in ANSYS Fluent with implicit mesh update and re-meshing is chosen to predict the motion of the plate. A time step size of 0.25 ms is used with a maximum of 100 iterations per time step, which proved to be sufficient. Furthermore, a mesh with 21237 cells is chosen for all further simulations of falling plates. The ANSYS Fluent files for the simulations can be found on the attached CD. An overview of the content of the CD is given in Appendix I.

Chapter 5

Experimental Investigation of Flat Plates

This chapter contains a description of experiments carried out with the purpose of validating the CFD simulations. The experiments are carried out by letting an aluminium plate fall in water and recording the trajectory using digital video camera. The following sections give an overview of how the experiment is carried out.

5.1 Description of Experiment

Plates with dimensions $L \cdot h \cdot b = 40.0 \text{ mm} \cdot 2.0 \text{ mm} \cdot 206.0 \text{ mm}$ are dropped in a glass container with water. The container has the dimension 600 mm, 350 mm, and 300 mm. The trajectories of the plates are measured using a digital video camera as shown in Figure 5.1.

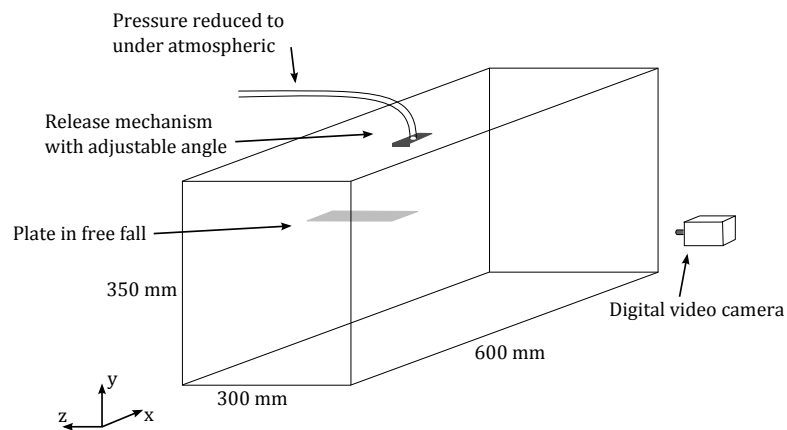


Figure 5.1. Experimental setup to record trajectories of flat plates in free fall.

The glass container is filled with water and a release mechanism is placed at a distance under the water surface to ensure well-controlled initial conditions. The release mechanism consists of a vacuum pump which holds the plate at an initial angle before it is released and let free to fall.

Video recordings are taken at 33.3 frames per second with an exposure time of 20 ms. The exposure time is chosen as a compromise between not blurring the plate during an exposure,

and allowing the sensor of the camera to capture enough reflected light from the plate to be able to filter out noise from the images afterwards.

In order to ensure close to stagnant water in the container when the plate is released, the time between two successive free falls is a couple of minutes. This allows the water to settle sufficiently. Picking up the plates from the bottom of the glass container causes disturbances to the water. Therefore, four similar plates are used to increase the time interval between plates having to be picked up.

The following gives an overview of the apparatus used for the experiments.

5.2 Apparatus and Instruments

The apparatus and instruments used for the free fall experiments are listed in Table 5.1.

Table 5.1. Overview of the apparatus and instruments used in the free fall experiment.

Apparatus	Specification
Glass container	Standard 64 L aquarium
Digital video camera	Photon Focus MV1
Light bulb	OSRAM Deluxe EL 15 W
Lens	Navitar 25 mm f1.4
Release mechanism	270 mm vacuum pump (unknown manufacturer)
Computer with software	AOS image studio and LabVIEW Vision

5.3 Processing of Results

Since each recorded trajectory consists of approximately 100 images, a way to batch process the images is used. For this purpose the LabVIEW Vision software suite is used to filter out noise and measure the plate orientation and position in each frame. An algorithm is developed within LabVIEW Vision, which can be applied directly to each frame.

Firstly, a colour plane extraction is applied to convert the picture to monochrome. Secondly, a threshold filter is applied to increase the contrast. Finally, a particle filter is applied to filter out noise. The procedure is shown in Figure 5.2 using LabVIEW Vision nomenclature.



Figure 5.2. Batch processing procedure in LabVIEW Vision nomenclature.

The exact settings used to batch process the images are given in Table 5.2.

Table 5.2. Settings used to batch process the raw images captured during the experiments.

Settings	Value
Colour plane extraction	RGB - Green plane
Manual threshold	Looks for bright objects - minimum threshold 29
Particle filter	Area > 600 pixels 250 pixels < y-position < 900 pixels

Figure 5.3 illustrates how an image is batch processed using the LabVIEW Vision algorithm presented in Figure 5.2 with the settings in Table 5.2.

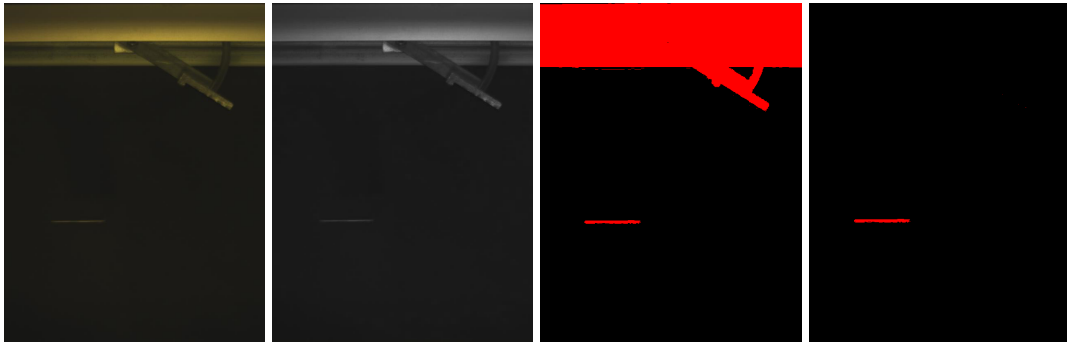


Figure 5.3. From left to right: Original image, colour plane extraction filter applied, threshold filter applied, and particle filter applied.

The successive steps in the figure indicates that the LabVIEW Vision software is capable of filtering out noise and leaving the plate behind. Figure 5.4 shows a series of frames processed by the LabVIEW Vision software.

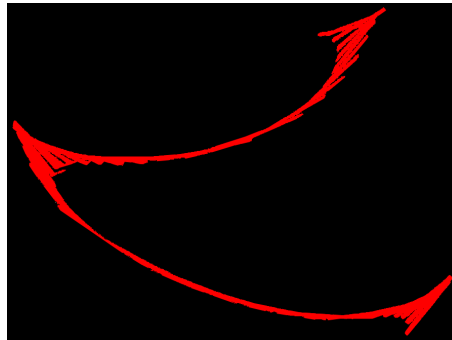


Figure 5.4. A series of frames captured during a free fall sequence and processed using LabVIEW Vision.

The raw images captured during the free fall sequences are attached on a CD as presented in Appendix I. The following presents the results obtained by nine free fall recordings.

5.4 Presentation of Results

In order to compare the results, the frame from each frame sequence corresponding to the same location has been found based on visual inspection. Figure 5.5 shows the nine free fall trajectories, while Figure 5.6 shows the plate orientation angle as function of time.

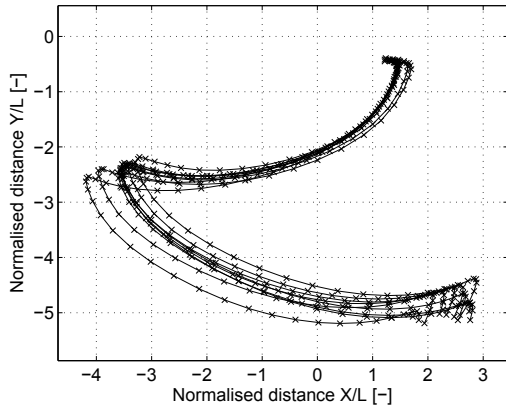


Figure 5.5. Experimental results showing the trajectories normalised by the plate length.

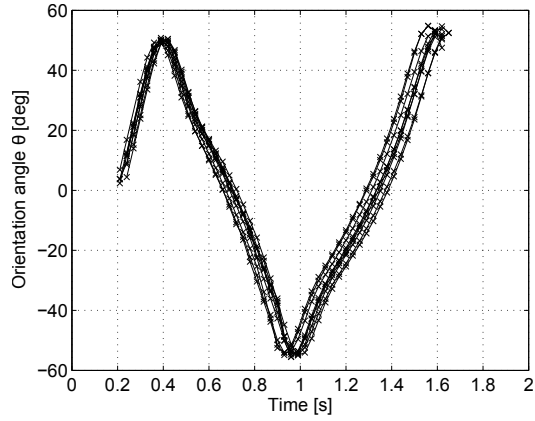


Figure 5.6. Experimental results showing the orientation angle as function of time.

The two figures indicate that the nine successive free falls are quite similar. There are however some trajectories differing considerably from the mean trajectory. One way to quantify the deviation between the nine free falls is by using statistical measures. A set of statistical considerations is given in the following subsection.

5.4.1 Statistical Considerations

Due to the time dependent motion, the overall uncertainty of the trajectory is expected to increase with time. In order to quantify the deviation between the recorded trajectories, limits corresponding to 95 % confidence interval are of interest. The limits to be determined are given in Equation (5.1), where \bar{x} is the sample mean value, n is the number of samples equal to 9, s is the sample standard deviation, and $t_{\alpha/2}$ is the critical value of the t-distribution with $\alpha = 1 - 0.95 = 0.05$. The t-distribution is used instead of the normal distribution as $n < 30$ (Walpole et al., 2012).

$$\bar{x} - t_{\alpha/2} \frac{s}{\sqrt{n}} < x_o < \bar{x} + t_{\alpha/2} \frac{s}{\sqrt{n}} \quad (5.1)$$

The critical values for the t-distribution are found in an appropriate table for a 95 % confidence interval ($\alpha/2 = 0.025$) with degrees of freedom $\nu = n - 1 = 9 - 1 = 8$ to be $t_{\alpha/2} = 2.306$. The sample mean and standard deviation to be used in Equation (5.1) are calculated based on Equation (5.2) and (5.3) respectively.

$$\bar{x} = \frac{1}{n} \sum_{i=1}^n x_i \quad (5.2)$$

$$s = \sqrt{\frac{1}{n-1} \sum_{i=1}^n (x_i - \bar{x})^2} \quad (5.3)$$

The results presented in Figure 5.7 and 5.8 show the normalised x- and y-coordinates as function of time along with a 95 % confidence interval. Figure 5.9 shows the plate orientation together with the a 95 % confidence interval.

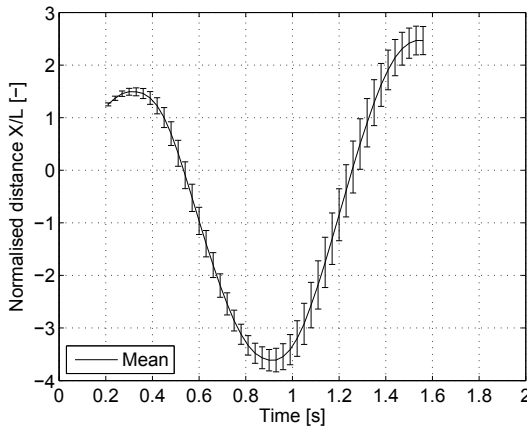


Figure 5.7. Experimental results showing the normalised x-coordinate and the limits corresponding to a 95 % confidence interval.

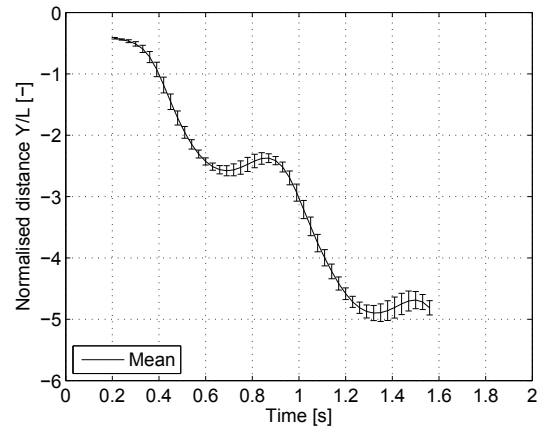


Figure 5.8. Experimental results showing the normalised y-coordinate and the limits corresponding to a 95 % confidence interval.

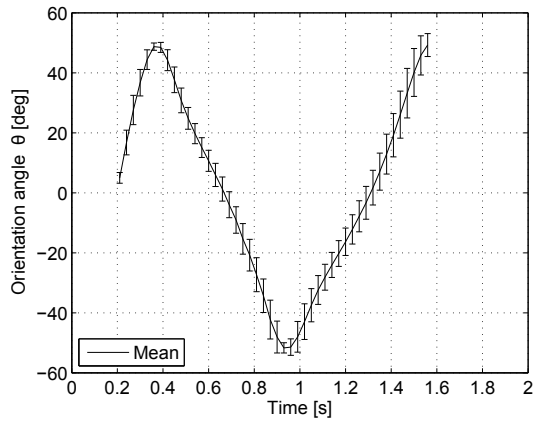


Figure 5.9. Experimental results showing the plate orientation angle and the standard deviation σ as function of time.

The figures show that the 95 % confidence interval increases with time as expected. The results presented in Figure 5.7 and 5.8 show that the limits of the 95 % confidence interval correspond to approximately 0.5 plate length at the end of the free fall. Additionally, the orientation angle is within an interval of 10-20 degrees at the end of the free fall. Even though some of the trajectories differ, the experiments generally show the same trajectory. The uncertainty can be described by a number of factors which will be listed and discussed in the following.

5.5 Sources of Error and Uncertainties

This subsection contains a discussion of the different sources of error and uncertainties encountered in the experiment. Since errors accumulate in time, a small deviation in initial condition will result in increasing deviations as the fall proceeds. The following subsections contain a list of uncertainties in the experiment.

5.5.1 Precision of Plate Release Time

The plate was released manually by turning off the vacuum pump. Therefore the only way to tell when the plate was moving, was by visual inspection of the images captured. In order to normalise the time in the sequences, the maximum orientation angle in the first turn was found and the images were normalised accordingly. The images were captured at 33.3 frames per second resulting in a time between two successive images of 0.03 s. As the images were captured at a finite rate and normalised afterwards, there might be a small shift in time corresponding to maximum half the frame rate.

5.5.2 Three-dimensional Effects

Some precautions were taken to minimise 3D effects and obtain comparable quasi 2D results. One result of undesirable 3D effects is the fact that even small rotations around x- and y-axis will become important when a long trajectory is investigated. Different approaches are used to deal with this effect in literature. One approach is to add a thin stabilising ring to each side of the plate that touches the sides of the glass container when the plate tries to rotate around the x- and y-axis. This approach has been used by Belmonte et al. (1998) to investigate the different falling regimes. These rings do however add mass to the plate, cause friction, and thereby alter the plate trajectory.

In this present experiment the plates do not extend all the way to the sides of the glass container, leaving approximately 47 mm at each side at the initial position. When the plates were released, they did not translate significantly along the long axis and they did not touch the sides throughout the fall.

Another 3D effect caused by a higher pressure below the plate than on the top of the plate. This pressure difference results in fluid to move from the lower to the upper side around the tips of the plate. This phenomenon is not taken into account in the quasi-steady 2D model or the CFD simulations. The result is the pressure on top of the plate being slightly lower, causing a lower lift force and thereby altering the trajectories. This effect is minimised since the plate width is much longer than the length $b/L = 206.0 \text{ mm}/40.0 \text{ mm} > 5$. To even further reduce 3D effects a larger glass container and longer plates could have been used.

5.5.3 Consistency of Plates and Manufacturing Flaws

The dimensions of the four plates differ by very small amounts, resulting in slightly different masses of the plates. The mass of the plates was $m = 43.51 \pm 0.05 \text{ g}$, corresponding to a mean density $\rho_p = 2640 \text{ kg/m}^3$. Throughout the report the density of aluminium has been assumed to be $\rho_{\text{alu}} = 2700 \text{ kg/m}^3$. The result is slightly faster falling plates in the simulations than in the experiments. The plates are cut out of a large aluminium plate resulting in more or less sharp edges. Figure 5.10 shows the height of the plate h and a slightly deformed edge.

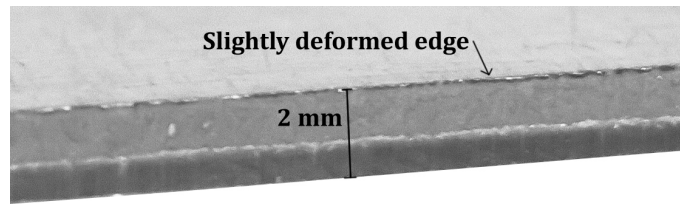


Figure 5.10. Close-up photograph of the edge of a plate.

The figure shows that the edge is close to 90 deg. A rounded edge would decrease separation at the leading edge and eventually cause the boundary layer to build up right from the edge. This would alter the pressure distribution around the plate significantly and cause the distance between the centre of pressure and centre of gravity to increase. As a result, the net torque on the plate would increase and thereby result in a different plate trajectory. The edges are however very close to 90 deg and therefore the impact of manufacturing flaws is expected to be minimal.

Furthermore, the plates have minor scratches in the surface. A high contrast photograph of a plate is shown in Figure 5.11.



Figure 5.11. High contrast photograph of a plate showing surface scratches.

These surface scratches will promote a turbulent boundary layer resulting in a lower drag coefficient leading to a different trajectory. This effect is however expected to have a minimal impact on the results, though a quantification of it has not been attempted.

Chapter 6

Results for Freely Falling Flat Plates

This chapter contains the results related to plates in free fall obtained by the CFD simulations presented in Chapter 4 and the experiment presented in Chapter 5. The purpose of the chapter is two-fold. The first part deals with validation of the CFD simulations by the experiment described in Chapter 5, while the second part presents the time dependent detailed flow field obtained by the CFD simulations.

6.1 Validation of CFD Simulations by Experiment

The results obtained by the CFD simulation of the plate in free fall are compared to results from the experiment described in Chapter 5. One simple way to validate the CFD simulations is by comparing the trajectories. In Figure 6.1, the mean trajectory of the experiment, the trajectory with best correspondence, and the trajectory with worst correspondence are compared with the CFD simulations.

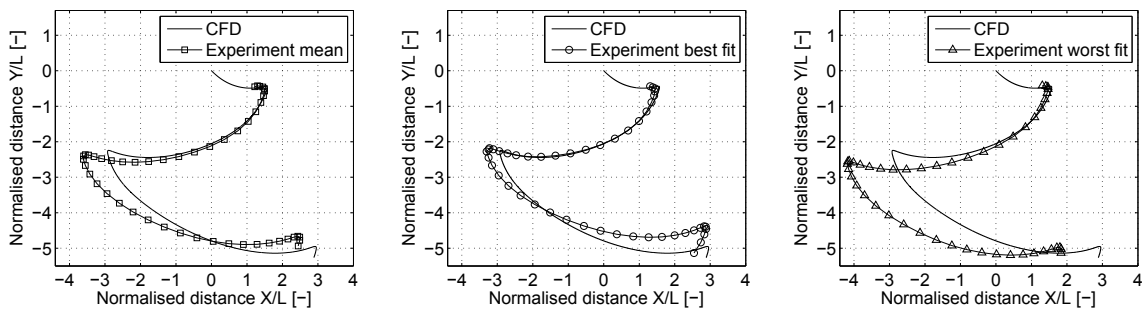


Figure 6.1. Comparing free fall trajectory measured by experiment and computed using CFD.

As Figure 6.1 clearly shows, the CFD simulation is capable of predicting the trajectory within a reasonable error of accuracy. Small errors in flow field are integrated and the error will therefore be accumulated with time as the figure shows. In order to quantify the plate orientation angle throughout the free fall, Figure 6.2 showing the plate orientation angle θ as function of time is used. In order to compare the results, two parameters are used. These are the turning angles θ_1 and θ_2 and the time between the first two turns Δt . These two parameters are sketched in the figure.

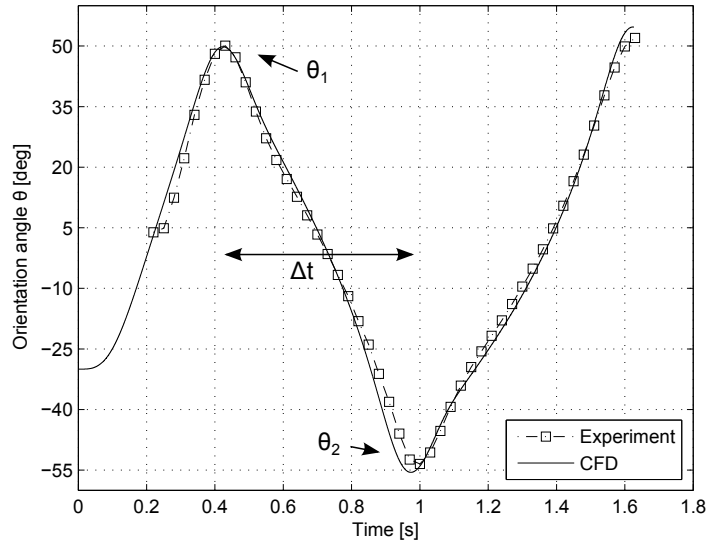


Figure 6.2. Comparison of the plate orientation angle as function of time for the experiment and the CFD simulation.

The figure indicates that the CFD simulation is capable of predicting the plate orientation angle throughout its fall. To quantify and compare the results, Table 6.1 is used. The table shows the maximum turning angles as well as the time between the first two turns.

Table 6.1. Comparison of experiment and CFD simulation by the plate orientation angle θ .

Parameter	Turning angle 1 θ_1	Turning angle 2 θ_2	Turning time Δt
Experiment	50.8 deg	- 53.5 deg	0.57 s
CFD	49.8 deg	- 55.6 deg	0.55 s
Percent deviation	2.0 %	3.9 %	3.4 %

As can be seen from the table there are only small deviations between the results of the experiment and the CFD simulations.

Another way to compare the trajectories is by comparing the location of the plate in time. For this purpose, Figure 6.3 gives the normalised x-position in the stationary global coordinate system (X-Y) as function of time. The normalised extreme positions during the free fall X_{extreme}/L as well as the time between the two extreme positions Δt are of interest in order to compare the results. These are shown in the figure as well.

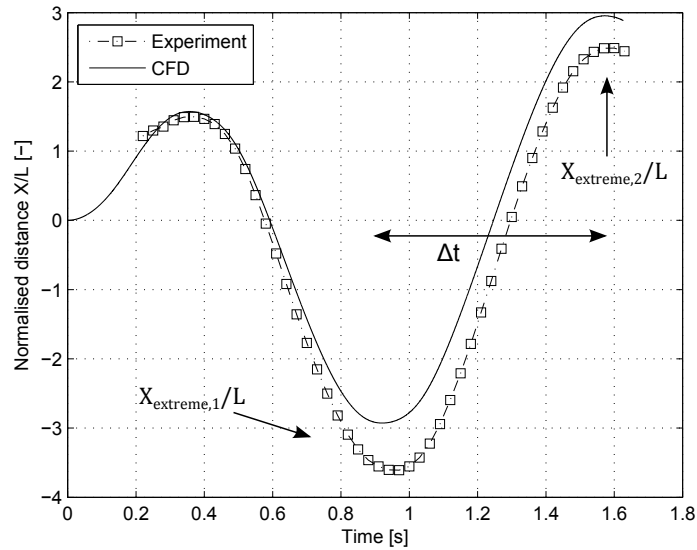


Figure 6.3. Normalised x-coordinate in the stationary global coordinate system as function of time for the CFD simulation and the experiment.

A comparison of the two parameters X_{extreme}/L and Δt is given in Table 6.2.

Table 6.2. Comparison of experiment and CFD simulation by the x-distance normalised by the plate length.

Parameter	Extreme Position 1	Extreme Position 2	Time between extreme positions
	$X_{\text{extreme},1}/L$ [-]	$X_{\text{extreme},2}/L$ [-]	Δt
Experiment	- 3.61	- 2.49	0.63 s
CFD	- 2.93	- 2.96	0.65 s
Percent deviation	18.9 %	18.7 %	3.2 %

As the table shows, the CFD simulation is capable of predicting the extreme positions within 18.9 % and 18.7 % and the time between the extreme positions within 3.2 %.

Figure 6.4 shows the normalised y-position in the stationary global coordinate system as function of time. Furthermore, the figure shows three parameters of interest. These are the distance the plate elevates at the end of each turn $\Delta(Y/L)_{\text{elev}}$, the distance the plate falls during each turn $\Delta(Y/L)_{\text{fall}}$, and the time for the fall Δt .

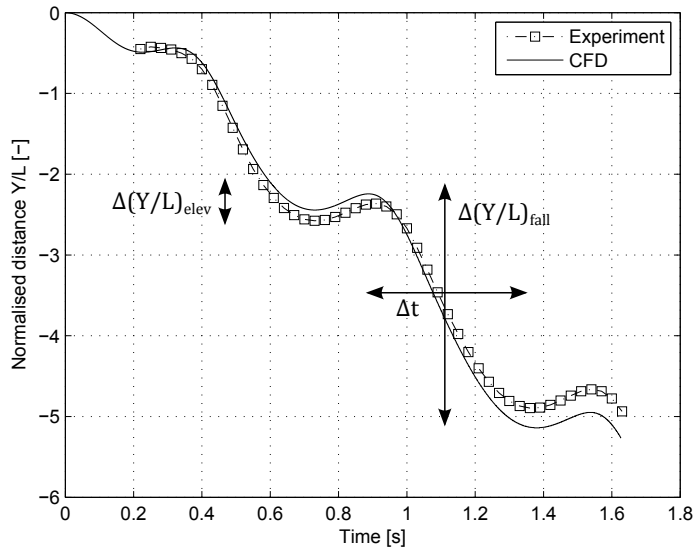


Figure 6.4. Normalised y-coordinate in the stationary global coordinate system as function of time for the CFD simulation and the experiment.

Table 6.3 shows a comparison between the experiment and CFD simulation of the y-distance. The three parameters of interest are $\Delta(Y/L)_{\text{elev}}$, $\Delta(Y/L)_{\text{fall}}$, and Δt .

Table 6.3. Comparison of experiment and CFD simulation by the y-distances normalised by the plate length.

Parameter	Elevation distance $\Delta(Y/L)_{\text{elev}}$ [-]	Fall distance $\Delta(Y/L)_{\text{fall}}$ [s]	Fall time Δt [s]
Experiment	0.21	2.53	0.45
CFD	0.20	2.90	0.49
Percent deviation	4.8 %	14.6 %	8.9 %

From the table it is seen that the CFD simulations are generally capable of predicting y-location as function of time for the free fall trajectory. The elevation distance predicted by the CFD simulation is within 4.8 % of the measured. Likewise the fall distance is within 14.6 % and the fall time deviates 8.9 % from the experiment.

To clarify in which part of the trajectory, the deviation arises, a so-called butterfly plot, showing the y-velocity as function of the x-velocity is used. This is presented in Figure 6.5.

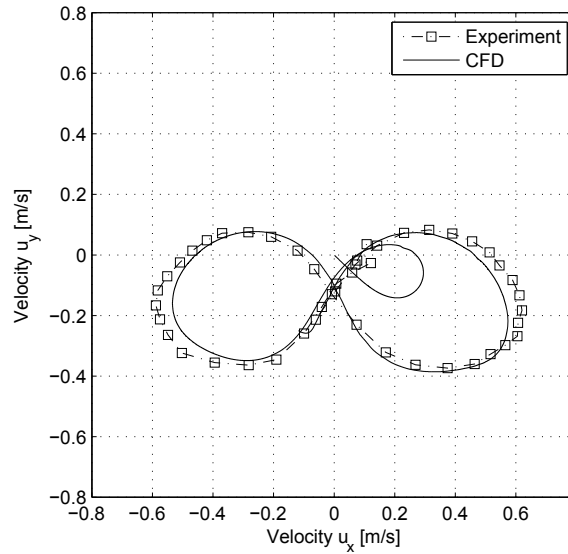


Figure 6.5. Butterfly plot showing the plate y-velocity as function of x-velocity. Note the first part corresponding to the time interval $[0;0.3]$ s is not included in the experimental results.

As indicated by the figure, the velocities deviate the most when the x-velocity is high. This can be explained by the 3D effects discussed in Section 5.5. Instead of showing integrated values such as velocities and position, the accelerations are of interest as these are directly related to the forces on the plate. To investigate in which part of the trajectory the forces on the plate deviate the most, the acceleration as function of time is of interest. Figure 6.6 and Figure 6.7 show the instantaneous accelerations for the plate throughout the free fall for both the experiment and the CFD simulation.

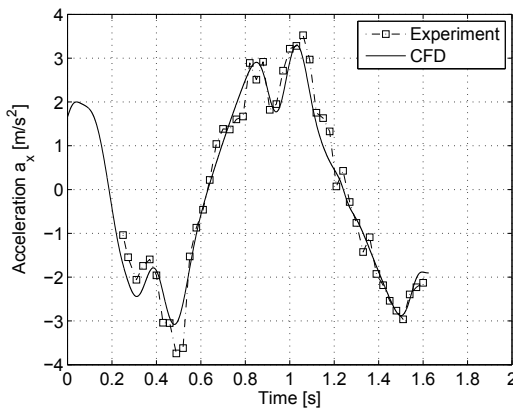


Figure 6.6. x-acceleration as function of time for the CFD simulation and the experiment.

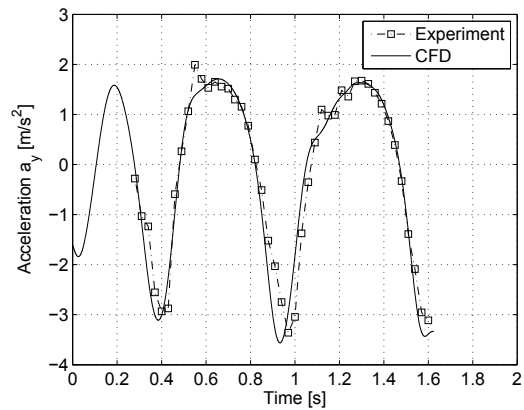


Figure 6.7. y-acceleration as function of time for the CFD simulation and the experiment.

The two figures show an overall great correspondence between the results obtained by the experiment and the CFD simulation. The experiments show local errors which can be explained by the position being differentiated twice resulting in larger deviations. Figure 6.7 show the results deviate the most when the y-acceleration is high at approximately $t = 0.4$ s and $t = 0.9$ s, corresponding to the plate is turning. This suggests the assumption of the experiment being quasi two-dimensional is most uncertain in the turns. The following section presents a visualisation of the detailed flow field obtained by the CFD simulation.

6.2 Visualisation of Flow Field

The purpose of this section is to present visualisations of the flow field in terms of velocities and pressures at different instances during a free fall. The advantage of using a visualisation technique is that it allows for the fluid dynamics to be understood in details. Therefore, the flow field is visualised at different instances which are representative for the general fall trajectory. The different locations of special interest are shown in Figure 6.8 and described below. Furthermore, Figure 6.9 to 6.15 contain contour plots showing the pressure and velocity field at the instances of interest.

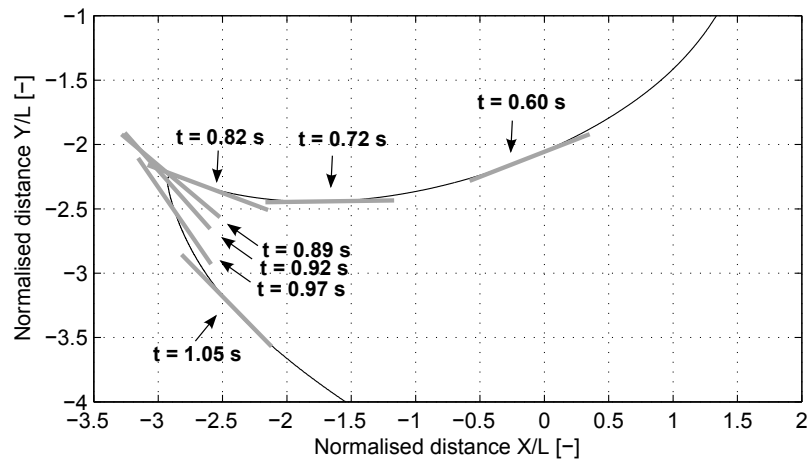


Figure 6.8. CFD simulated free fall trajectory with various instantaneous plate positions and orientations shown explicitly.

- **$t = 0.60$ s:** High plate velocity results in a high viscous drag and thin boundary layer. Plate begins to accelerate clockwise.
- **$t = 0.72$ s:** Plate aligned perfectly horizontally and the plate begins to elevate due to a high lift force, even though the angle of attack is close to zero. This lift force can be explained by the rotational motion of the plate resulting in an in-stationary boundary layer.
- **$t = 0.82$ s:** Plate elevates with maximum vertical velocity. The deceleration of the plate, which started at around $t = 0.60$ s, has caused the surrounding fluid to continue past the plate resulting in a negative viscous force. The angle of attack begins to increase dramatically.
- **$t = 0.89$ s:** Plate reached a maximum elevation height. Despite the lowest plate velocity throughout the fall, unsteady forces play a dominant role in the description of the plate motion. The plate continues to translate in the x-direction resulting in a delay between maximum y- and x-position. Furthermore the plate reaches the maximum rotational velocity.
- **$t = 0.92$ s:** Plate reaches extreme y-position. Due to the high orientation angle and zero x-velocity, the plate experiences the highest negative y-acceleration. The plate does however continue to rotate, resulting in a delay between the maximum x-position, y-position, and orientation angle.
- **$t = 0.97$ s:** Plate reaches maximum orientation angle before it begins its long horizontal gliding motion.
- **$t = 1.05$ s:** Plate reaches maximum negative y-velocity. A high net force in x-direction causes the x-velocity to increase and therefore the lift force increases as well.

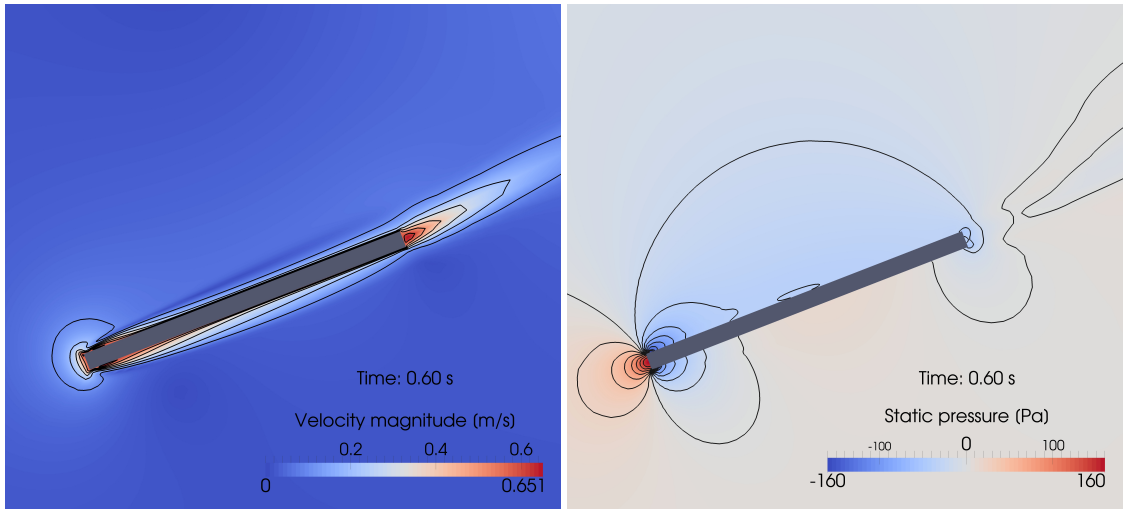


Figure 6.9. Velocity (left) and pressure (right) at $t = 0.60$ s. Red corresponds to higher values.

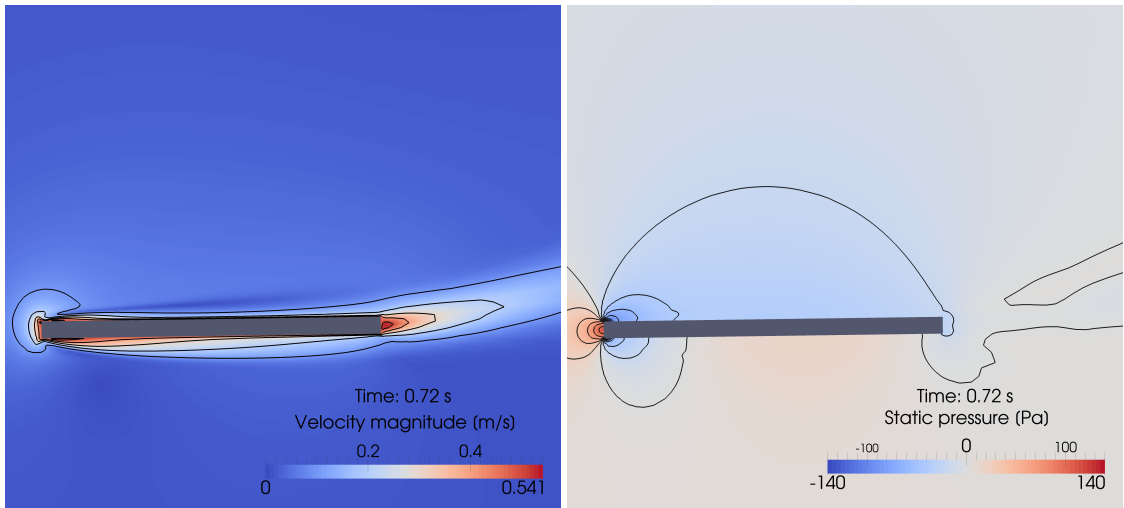


Figure 6.10. Velocity (left) and pressure (right) at $t = 0.72$ s. Red corresponds to higher values.

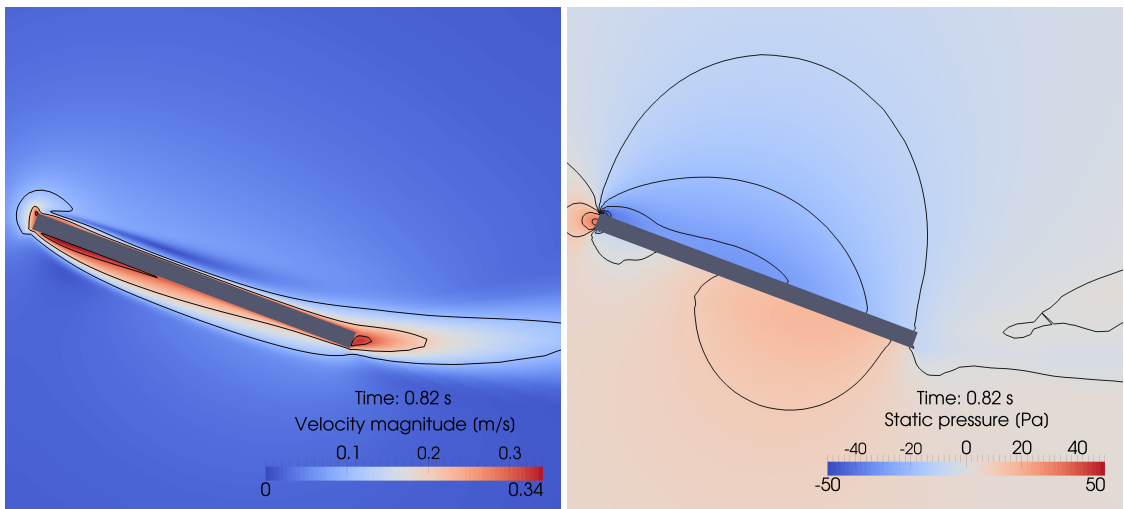


Figure 6.11. Velocity (left) and pressure (right) at $t = 0.82$ s. Red corresponds to higher values.

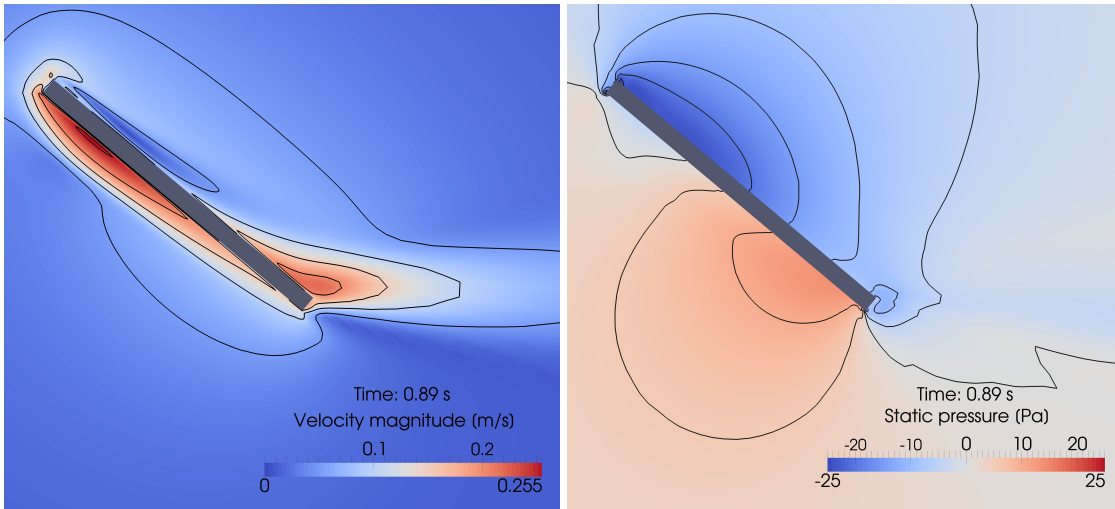


Figure 6.12. Velocity (left) and pressure (right) at $t = 0.89$ s. Red corresponds to higher values.

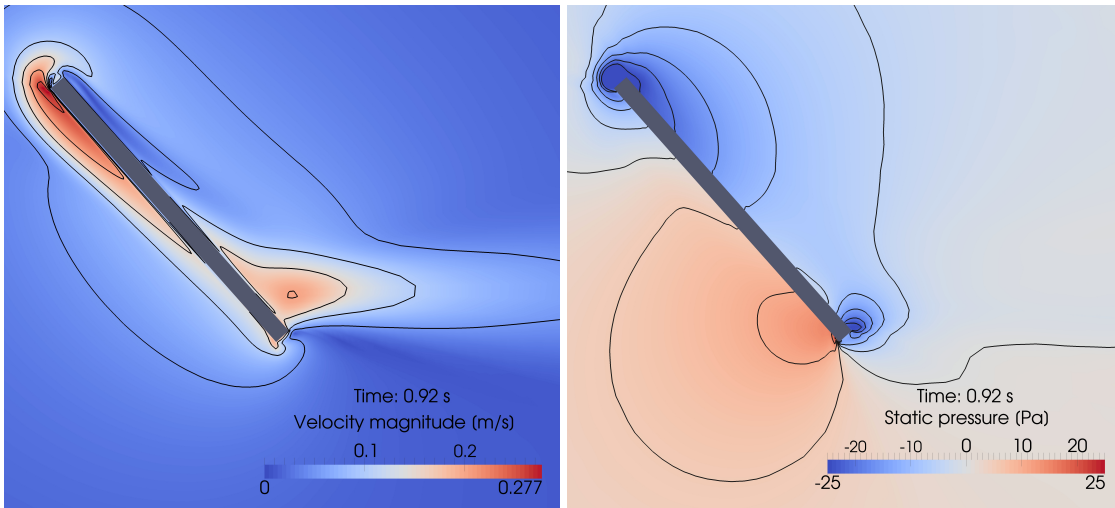


Figure 6.13. Velocity (left) and pressure (right) at $t = 0.92$ s. Red corresponds to higher values.

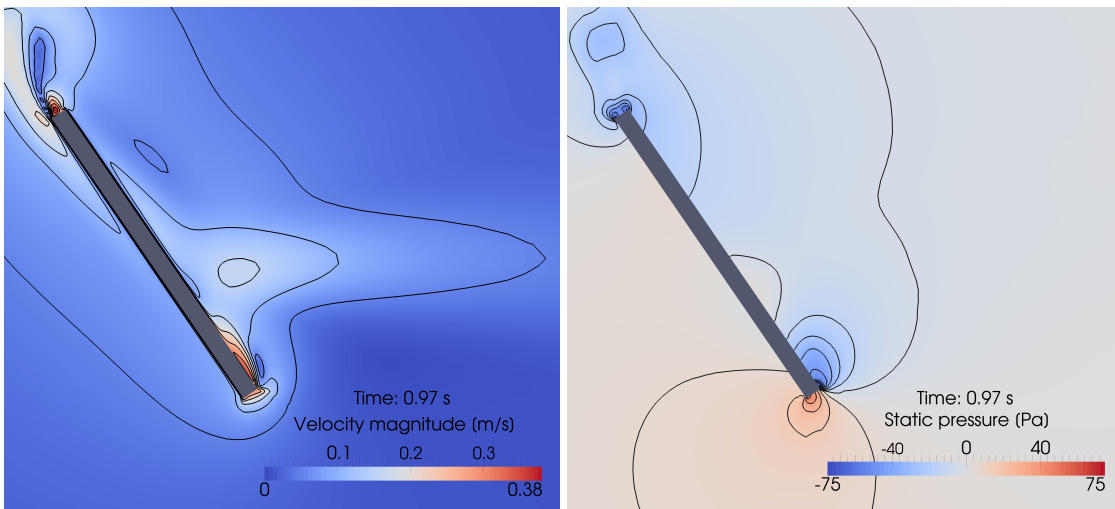


Figure 6.14. Velocity (left) and pressure (right) at $t = 0.97$ s. Red corresponds to higher values.

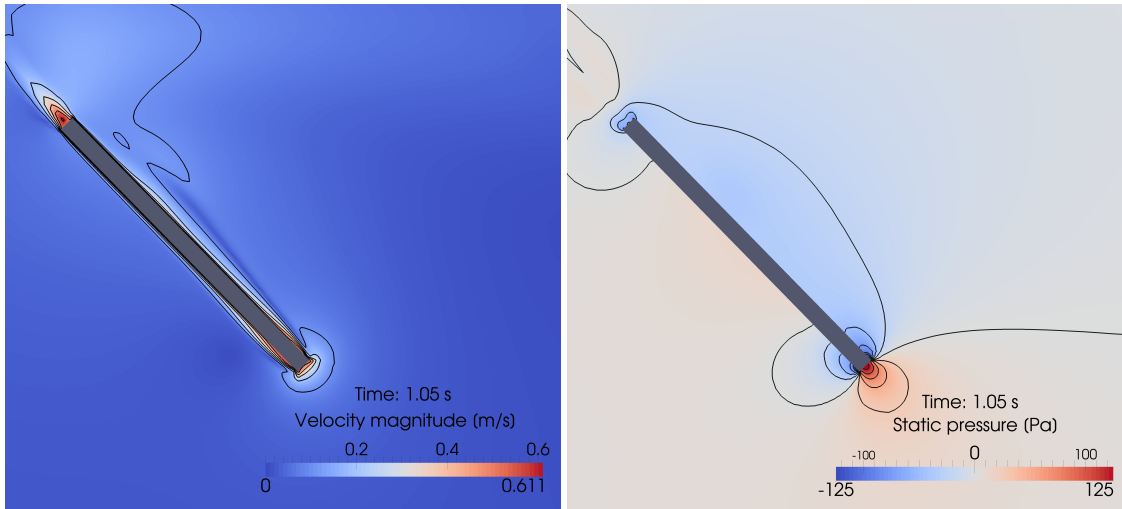


Figure 6.15. Velocity (left) and pressure (right) at $t = 1.05$ s. Red corresponds to higher values.

6.3 Terminal Velocity and Characterisation of Regime

As the figures presented throughout this chapter show, the trajectory of the plate can be characterised by the periodic oscillating motion regime. Now that the trajectory is modelled numerically and validated, the apparent terminal velocity can be evaluated and the apparent Reynolds number calculated. Based on the whole last period simulated ($t = [0.949; 1.600]$ s), the apparent terminal velocity is found to $u_{t,a} = 0.17$ m/s. This is as sketched in Figure 6.16.

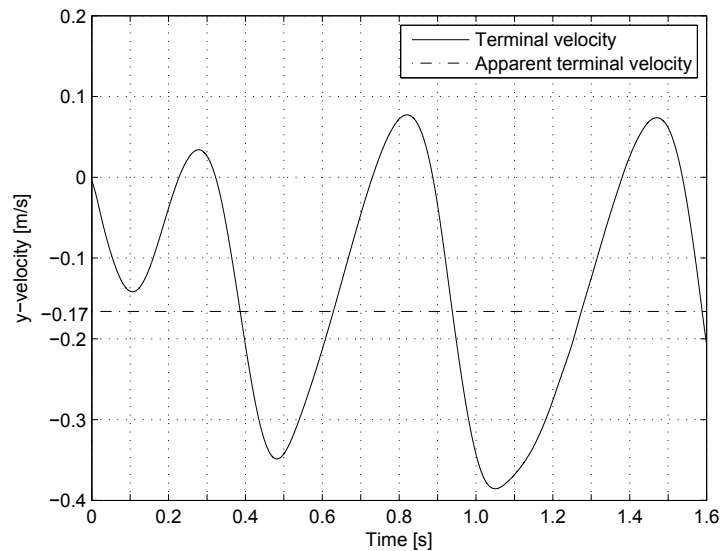


Figure 6.16. Terminal and apparent terminal velocity as function of time for the CFD simulation

A terminal velocity of 0.17 m/s corresponds to a Reynolds number of approximately 6750. Based on Equation (1.4) on page 4, the dimensionless moment of inertia is $I^* = 0.115$ for the plate considered in this work. Figure 1.4 suggests that this combination of Reynolds number and dimensionless number of inertia should result in the periodic oscillating motion regime, which is in good agreement with the trajectories observed in this work.

Chapter 7

Development of New Correlations for the Quasi-steady Two-dimensional Model

The quasi-steady model described in Chapter 3 is based on the existing modelling framework for flat plates in free fall. The results of this model along with the results of the validated CFD simulation are presented in Figure 7.1.

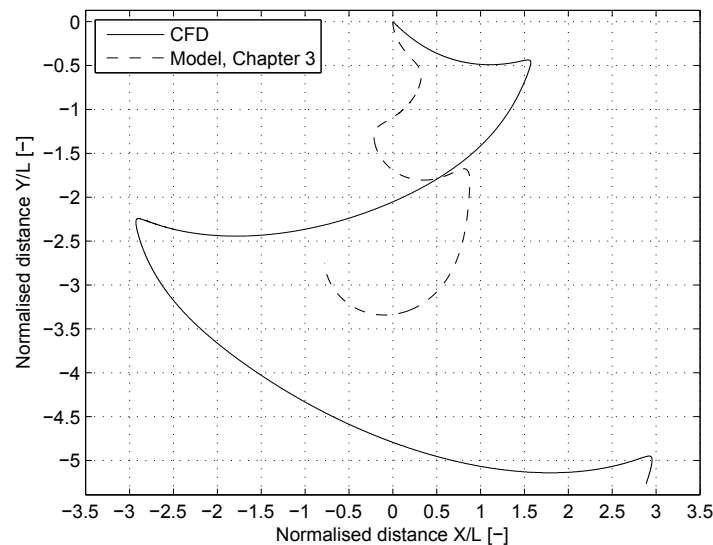


Figure 7.1. The result of the model described in Chapter 3.

The figure clearly indicates that the existing modelling framework is insufficient to model the plate trajectory. Therefore this chapter presents the development of new correlations, which can contribute to the modelling framework for flat plates in free fall. The chapter is split into different sections dealing with separate new correlations as follows:

- A new lift coefficient C_L correlation described in Section 7.1.
- A new drag coefficient C_D correlations described in Section 7.2.
- A new correlation for the centre of pressure location for the aerodynamic forces cp_o described in Section 7.3.

To establish new correlations, the experimental validated results presented in Chapter 6 will be used. These results provide a considerable amount of details related to the complex dynamics of a free fall. Furthermore, a set of unsteady CFD simulations of a fixed rotating plate will be used to extend the modelling framework.

Furthermore, Section 7.4 contains a comparison of the results obtained by the revised model and the results obtained by CFD and experiments. Finally, Section 7.5 outlines the model capabilities by predicting the motion of other flat plates with different dimensions, mass, and moment of inertia.

In the following, the term *turn* denotes the time at which the angle of attack changes sign. The turning points are located at $t = 0.34$ s, $t = 0.90$ s, and $t = 1.55$ s and are of interest in the description of the centre of pressure location, drag, and lift. The following section gives details on the lift coefficient for a flat plate in free fall and how a new correlation can be developed.

7.1 New Lift Coefficient Correlations

In Chapter 3 the lift coefficient was modelled as a function of the angle of attack only, that is $C_L = f(\alpha)$. This section presents the development of a new correlation for the lift coefficient. The correlation should enable a more precise prediction of the lift force acting on a plate in free fall. A PhD thesis on the unsteady aerodynamics of flat plates by Pesavento (2006) concluded that a simple quasi-steady 2D model is unable to explain the plate trajectories, since the lift on a falling plate is dominated by a rotational contribution. Due to this radical statement, rotational lift will be investigated further in the present work.

Rotational lift can be explained by highly unsteady effects. One such effect is a leading edge vortex moving along the plate surface, lowering the pressure locally resulting in enhanced lift. The vorticity of this leading edge vortex depends on the angular velocity and acceleration of the plate. Studies on these effects include Ericsson and Reding (1988), Panda and Zaman (1994), Granlund and Michael (2013), Lee and Gerontakos (2004), and Gharali and Johnson (2013).

The total net force perpendicular to the relative fluid velocity \vec{F}_{per} is extracted from the CFD simulation at all time steps. This force is used to determine a force coefficient C_{per} which is defined by Equation (7.1).

$$C_{\text{per}} = \frac{\vec{F}_{\text{per}}}{\frac{1}{2}\rho_f \cdot L \cdot b \cdot \vec{v}|\vec{v}|} \quad (7.1)$$

This net perpendicular force \vec{F}_{per} is a summation of different contributions all acting perpendicular to the relative fluid velocity. These contributions include translational lift, rotational lift, and unsteady effects such as added mass and history force. The total net perpendicular force coefficient as function of time for the free fall CFD simulation is shown in Figure 7.2.

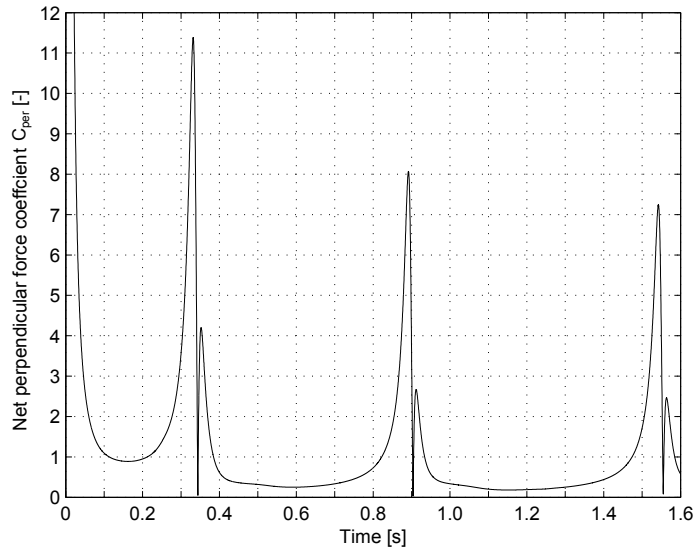


Figure 7.2. Net perpendicular force coefficient as function of time for the CFD simulation. Note that the net perpendicular force changes sign at $t = 0.34$ s, $t = 0.90$ s, and $t = 1.55$ s.

The figure shows high change in net perpendicular force coefficient, when the plate turns at $t = 0.34$ s, $t = 0.90$ s, and $t = 1.55$ s. Furthermore, the figure suggests a low coefficient when the plate translates at high velocity. In order to visualise the results in Figure 7.2 in a general manner independent of time, Figure 7.3 is used. Figure 7.3 shows the net perpendicular force coefficient as function of the angle of attack throughout the fall. The vertical line at $\alpha \approx -15$ deg corresponds to the initial time steps of the simulations.

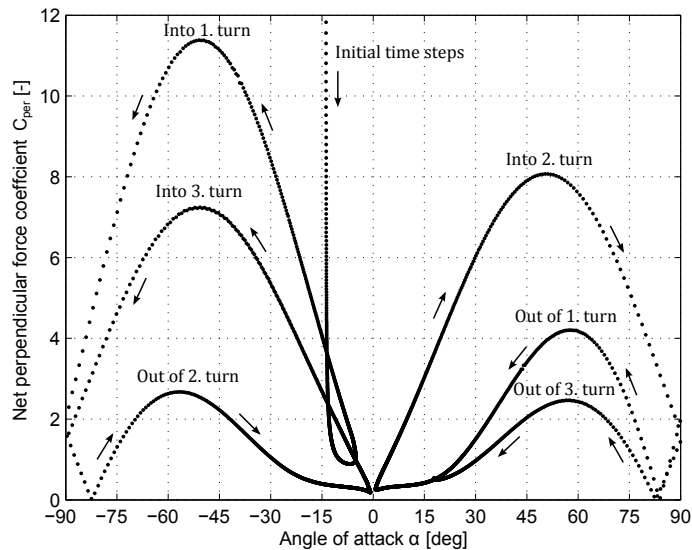


Figure 7.3. Net perpendicular force coefficient as function of angle of attack for the CFD simulation.

As the figure indicates, the angle of attack is insufficient to describe the net perpendicular force coefficient alone. Furthermore, the figure suggests the coefficient to be generally higher when the plate enters a turn than when it leaves a turn. As the plate is symmetrical around the chord, the coefficient is not expected to be a function of the sign of the angle of attack but rather the motion history. Figure 7.4 shows the net perpendicular force coefficient as function

of the absolute angle of attack $|\alpha|$ for $t > 0.60$ s, corresponding to the free fall without initial effects. That is, the first turn from the previous figure has been left out.

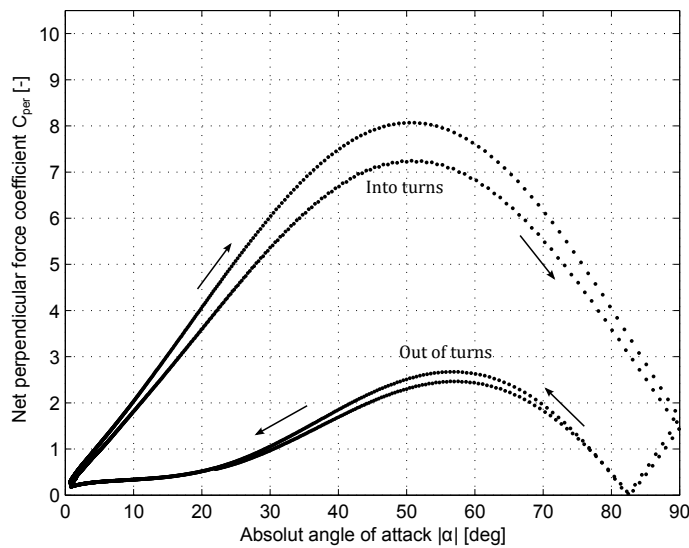


Figure 7.4. Net perpendicular force coefficient as function of absolute angle of attack for the CFD simulation of the flat plate in free fall for $t > 0.60$ s.

The figure shows, the four curves fall into two distinct curves of the net perpendicular force coefficient as function of angle of attack. These two curves correspond to the plate moving into a turn and out of a turn, as shown with arrows in Figure 7.4. This can be explained by the boundary layer being altered when the plate stops up and continues in the opposite direction. The result is a hysteresis lift curve also shown in Figure 7.4, where two similar angles of attack can result in different lift coefficients. One parameter of importance to describe this phenomena is the change in angle of attack in time $d\alpha/dt$.

As a result, a set of transient CFD simulations, presented in Appendix G, have been carried out to investigate the importance of the change in angle of attack in time $d\alpha/dt$. The CFD simulations consist of a series of simulations of flat plates rotating around the front edge with varying angular velocity between 0 deg/s and 90 deg/s with an interval of 5 deg/s. The Reynolds number throughout the fall varies from 2500 to 25000 as shown in Figure H.14. Therefore the CFD simulations are carried out at $Re_L = 10000$ as a compromise. The results of the simulations are shown in Figure 7.5 on the following page, with details presented in Appendix G.

It is clearly indicated in Figure 7.5 that the lift coefficient depends heavily on the angular velocity of the plate. Thus, an increased angular velocity of the plate results in an increased lift coefficient. The dashed lines in the figure are regressions of the results of the CFD simulations presented in Appendix G. These regressions are implemented in the quasi-steady model to include rotational lift as suggested by Pesavento (2006). The base curve in Figure 7.5 corresponds to the already presented lift curve in Subsection 3.2.3 on page 27.

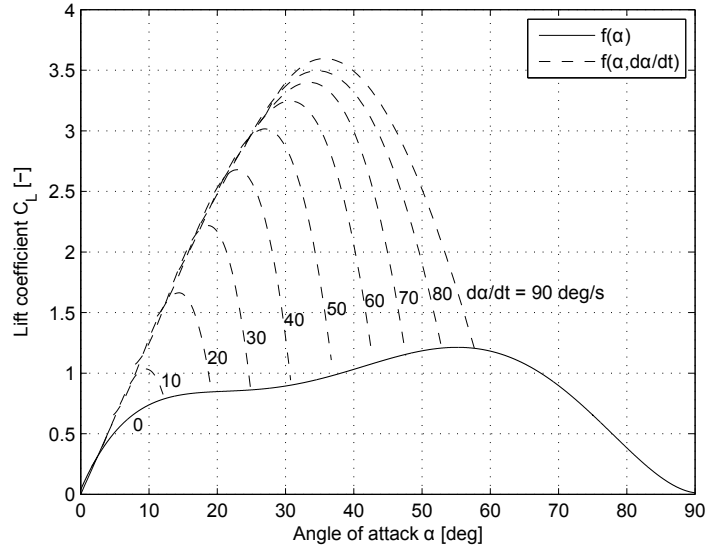


Figure 7.5. Lift coefficient as function of angle of attack and change in angle of attack found by the transient CFD simulations described in Appendix G at $Re_L = 10000$. The base-line curve for $da/dt = 0$ deg/s is found by the CFD simulations presented in Appendix A.

By comparing the maximum lift coefficient in Figure 7.2 and Figure 7.5 it is clear that the maximum net perpendicular force coefficient obtained from the CFD simulations of a falling plate will not be reproduced in the model by the regressions presented in Figure 7.5. However, the time span in which the net perpendicular force coefficient in Figure 7.2 exceeds the maximum values in Figure 7.5 is limited to around 0.05 s/turn. The maximum net perpendicular force coefficients occurs when the plate turns. In a turn the velocity of the plate is at a minimum and thereby the effect of the force coefficient will also be at a minimum. As a result, the lift coefficient description is expected to be significantly improved by including the results in Figure 7.5.

7.2 New Drag Coefficient Correlations

The purpose of this section is to present a new drag coefficient correlation able to improve the existing modelling frame work for flat plates in free fall.

The net tangential force coefficient C_{tan} is used to obtain information on the drag coefficient. It is defined as shown in Equation (7.2).

$$C_{tan} = \frac{\vec{F}_{tan}}{\frac{1}{2}\rho_f \cdot L \cdot b \cdot \vec{v}|\vec{v}|} \quad (7.2)$$

The net tangential force is a summation of all the forces acting tangential to the relative fluid velocity. Thus, all unsteady contributions are included as well. The total net tangential force coefficient as function of time for the free fall simulation is shown in Figure 7.6.

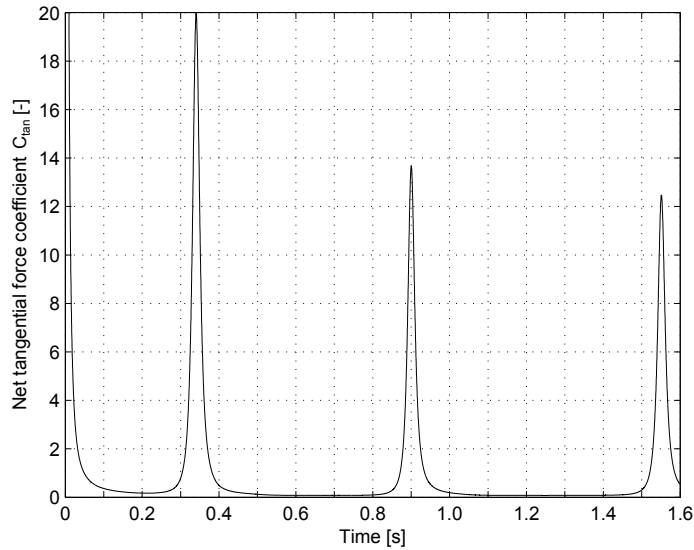


Figure 7.6. Net tangential force coefficient as function of time for the CFD simulation.

The figure indicates high net tangential force coefficients around the turning points at $t = 0.34$ s, $t = 0.90$ s, and $t = 1.55$ s. Additionally the drag coefficient is low when the plate is translating at high velocity parallel to its longer axis and thereby has an angle of attack close to 0 deg. This is in good agreement with Equation (3.21) on page 24. In order to express the drag coefficient as function of the angle of attack, Figure 7.7 is used. The figure shows the net tangential force coefficient as function of the angle of attack. The vertical line at $\alpha = -15$ deg corresponds to the initial time steps.

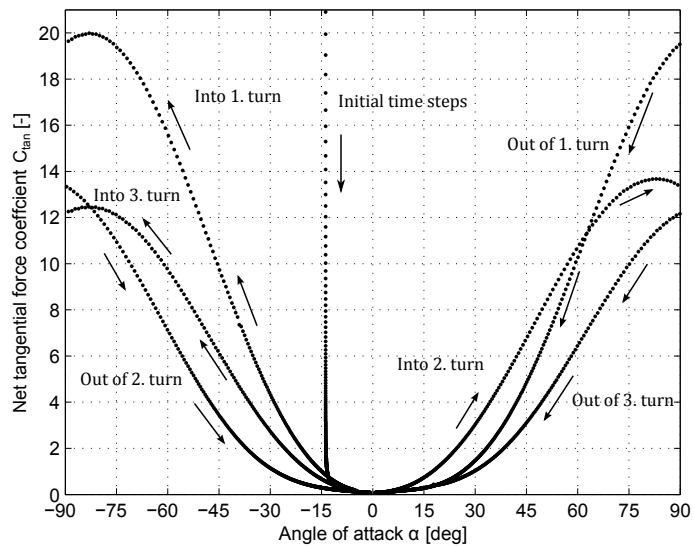


Figure 7.7. Net tangential force coefficient as function of angle of attack for the CFD simulation.

Figure 7.7 indicates the angle of attack to be insufficient in the description of the net tangential force coefficient alone, as different angles of attack result in the same coefficient. This suggests the tangential force coefficient not only to be a function of the angle of attack, but rather a combination of different factors such as the translational and angular velocities and

accelerations. As the plate is symmetrical around its chord, the tangential force coefficient should be independent on the sign of the angle of attack. Figure 7.8 shows the net tangential force coefficient as function of the absolute angle of attack $|\alpha|$ for $t > 0.60$ s, corresponding to the free fall without initial effects. That is, the first turn from the previous figure has been left out.

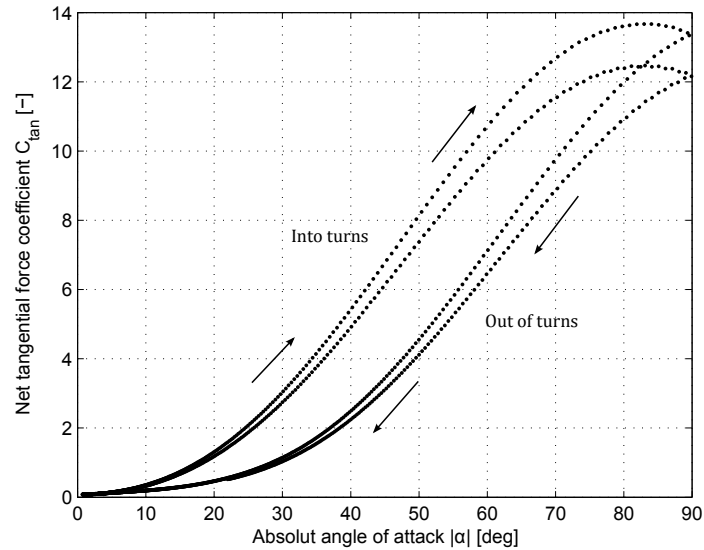


Figure 7.8. Net tangential force coefficient as function of absolute angle of attack for the CFD simulation for $t > 0.60$ s.

As described previously in Section 7.1 the unsteady CFD simulations presented in Appendix G investigates the importance of the change in angle of attack in for the lift coefficient. The same has been investigated for the drag coefficient. The results of these unsteady simulations for the drag coefficient at different angular velocities are presented in Figure 7.9.

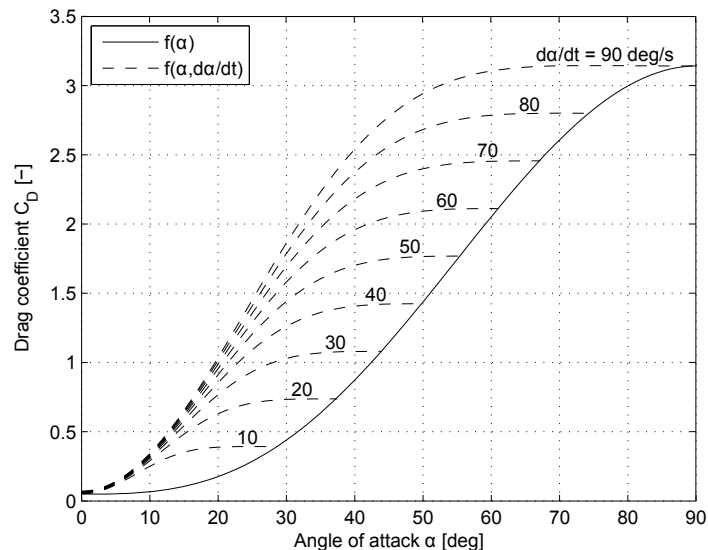


Figure 7.9. Drag coefficient as function of the angle of attack and change in angle of attack found by the unsteady CFD simulations presented in Appendix G at $Re_L = 10000$. The base-line curve $da/dt = 0$ deg/s corresponds to the correlation proposed in Chapter 3.

The dashed lines in Figure 7.9 are approximations to the raw results presented in Appendix G. These approximations are formulated in a general manner using a trigonometric function. This is given by Equation (7.3) with coefficients a_1 and a_2 given by Equation (7.4).

$$C_D = \frac{\pi}{a_2} + C_D(0) - \frac{C_D(0)}{a_2} \cdot \cos\left(a_1|\alpha| + \frac{\pi}{2}\right)^2 - \frac{C_D(90)}{a_2} \cdot \sin\left(a_1|\alpha| + \frac{\pi}{2}\right)^6 \quad (7.3)$$

$$a_1 = \left(\frac{\pi}{2\left|\frac{d\alpha}{dt}\right|}\right)^{1/2}, \quad a_2 = \frac{\pi}{2\left|\frac{d\alpha}{dt}\right|} \quad (7.4)$$

By including Equation (7.3) in the description of the drag coefficient, the drag coefficient becomes a function of both angle of attack α , change in angle of attack $d\alpha/dt$, and Reynolds number Re_L , thus $C_D(\alpha, d\alpha/dt, Re_L)$. The already existing modelling framework only included two variables. Namely the angle of attack and Reynolds number. The new formulation above does as well take the change in angle of attack into account and thus results in an improved formulation.

7.3 New Centre of Pressure Correlation

This section describes how a new correlation for the centre of pressure location of the aerodynamic forces is developed based on the validated CFD simulations presented in Chapter 6. A correlation able to predict the centre of pressure location for the aerodynamic forces during a free fall is of interest. Correlations presented in literature typically suggest the centre of pressure to be a function of the angle of attack only, that is $cp_o = f(\alpha)$. Figure 7.10 shows the centre of pressure location for the aerodynamic forces normalised by the plate length L as function of time for the free fall CFD simulations.

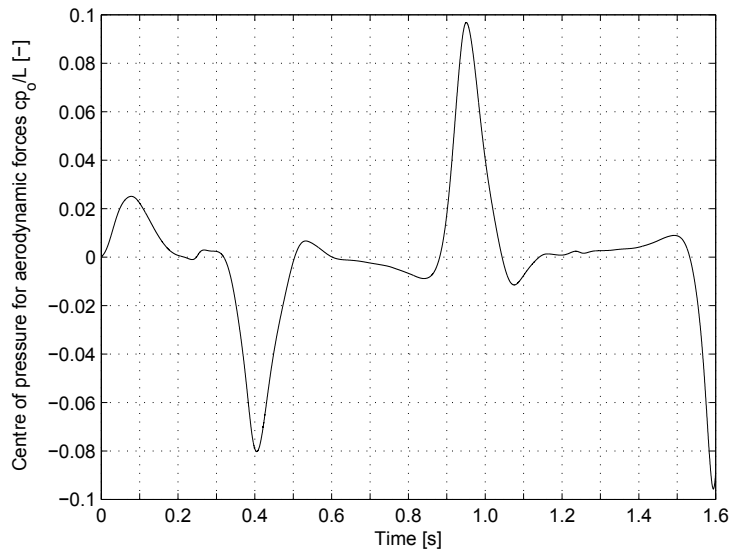


Figure 7.10. Normalised centre of pressure location for the aerodynamic forces as function of time for the free fall CFD simulations.

The figure indicates a high centre of pressure offset just after the turning points at $t = 0.34$ s, $t = 0.90$ s, and $t = 1.55$ s. Furthermore, the results presented in the figure suggest a normalised centre of pressure location at a distance of maximum $cp_o/L = 0.1$ away from

the geometric centre. The correlations, found in literature and presented in Figure 3.24 on page 35, suggest the centre of pressure distance to be maximum at $\alpha = 0$ deg with a value of between $cp_o/L = 0.18$ and $cp_o/L = 0.25$. This can be explained by the object considered, where the values of $cp_o/L = 0.18$ and $cp_o/L = 0.25$ are found for cylindrical objects. As the peaks in Figure 7.10 are found just after the turning points where $\alpha \neq 0$ deg, it is of interest to investigate at which angles of attack the centre of pressure location is at its maximum.

The correlations for the centre of pressure location presented earlier were a function of the angle of attack only, that is $cp_o/L = f(\alpha)$. Figure 7.11 is made based on this assumption. The figure shows the centre of pressure location for the aerodynamic forces cp_o/L as function of the angle of attack during the free fall CFD simulations.

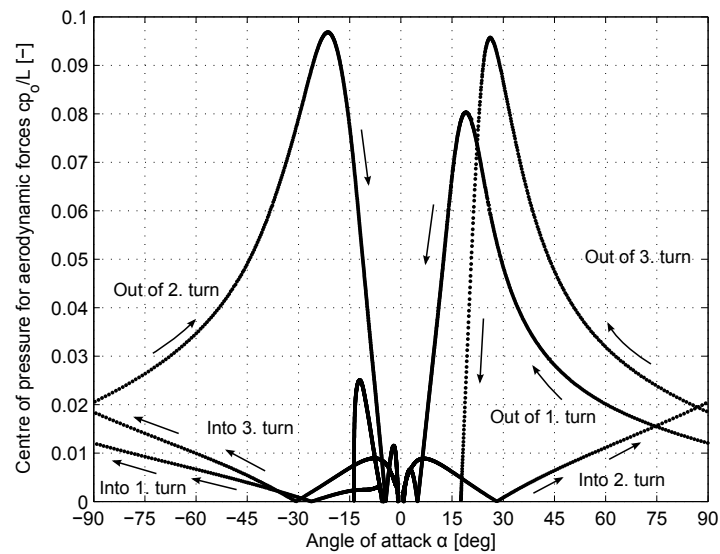


Figure 7.11. Normalised centre of pressure location for the aerodynamic forces as function of angle of attack for the free fall CFD simulations.

Based on the results presented in the figure, the angle of attack alone seems insufficient to describe the centre of pressure location for the aerodynamic forces, as the same angle of attack results in different centre of pressure locations throughout the fall. The three peaks in the figure at $cp_o/L \approx 0.95$, $cp_o/L \approx 0.95$, and $cp_o/L \approx 0.80$ are found just after the plate has left each turn, suggesting unsteady forces to play a dominant role in the description of the peaks. Using the detailed free fall CFD results presented in Appendix H, effort has been put into finding a correlation between the centre of pressure location and a variety of different factors such as translational velocity and acceleration, angle of attack, and the change in angle of attack in time. No such correlation has been found and therefore the centre of pressure is modelled using the traditional approach with a modified constant. Assuming the maximum centre of pressure location is found at $\alpha = 0$ deg and has magnitude $cp_o/L = 0.015$ based on Figure 7.11, the correlation in Equation (7.5) is made.

$$cp_o/L = 0.015 \cdot (1 - \sin(|\alpha|)^3) \quad (7.5)$$

A visualisation of the correlation presented in Equation (7.5) is shown in Figure 7.12.

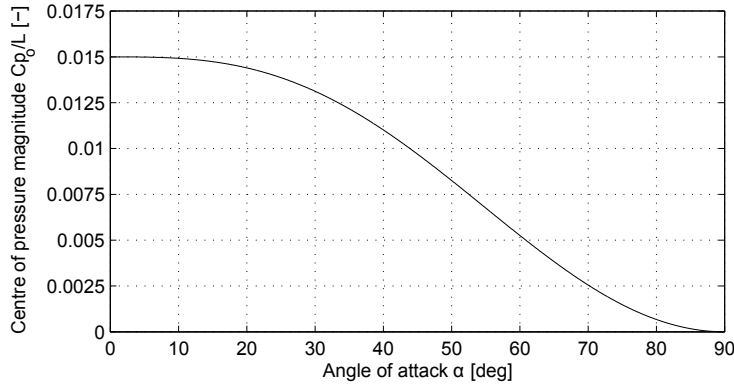


Figure 7.12. Correlation developed in the present work for the centre of pressure location for the aerodynamic forces.

A sensitivity analysis investigating the value of 0.015 and the shape of the function is given in Appendix D. The following section presents a comparison between the free fall CFD simulations and the model. The model formulation presented in Chapter 3 has been extended with the new correlations presented in this chapter, thus resulting in a revised model.

7.4 Results and Validation of Revised Model

To validate the revised model, a part of the trajectory is compared to the already experimentally validated CFD simulation. When the plate initially is let free to fall at zero velocity, unsteady forces play a dominant role (Simcik et al., 2008). These initial effects are not of major concern to be able to model correctly, and therefore the trajectories are compared after the first turn at $t = 0.60$ s. Furthermore, the inclusion of the added mass coefficient matrix found in Chapter 3 has not been included in the revised model, since it failed to improve the model. Additional information is given in a sensitivity analysis in Appendix D.

The model is initiated at $t = 0.60$ s with the position, orientation, translational and rotational velocities of the CFD simulation. The model is compared to the CFD simulations in the time interval ranging from $t = 0.60$ s to $t = 1.60$ s. This part of the trajectory, with time annotations, is visualised in Figure 7.13.

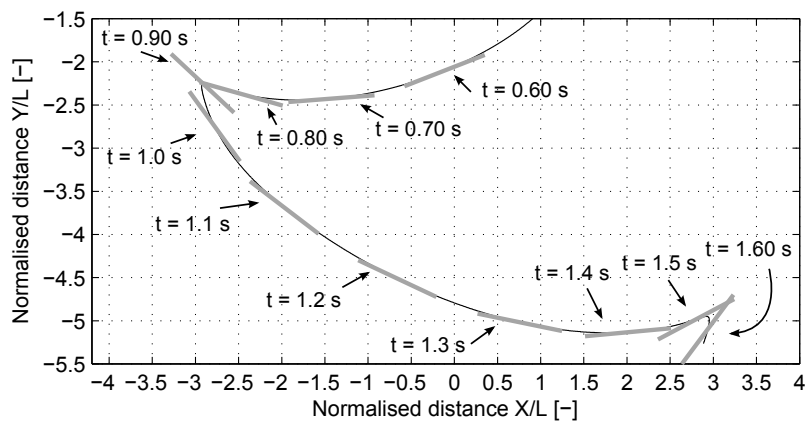


Figure 7.13. Part of the trajectory containing all characteristics of a free fall and therefore used to validate the revised model.

To investigate if the model is capable of predicting the free fall behaviour of a flat plate, the model is compared to the validated CFD simulations in terms of free fall trajectory and time dependent orientation angle and normalised x- and y- positions. The following four figures show these comparisons, where the trajectory is shown in Figure 7.14, the orientation angle in Figure 7.15, the x-position in Figure 7.16, and the y-position in Figure 7.17.

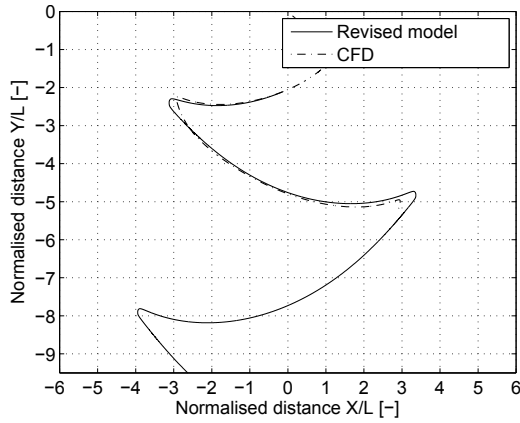


Figure 7.14. Free fall trajectory for CFD and revised model.

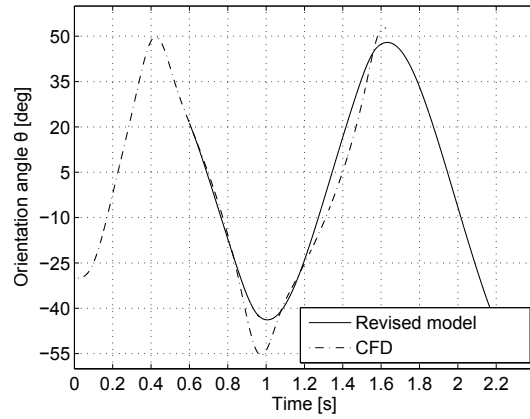


Figure 7.15. Orientation angle as function of time for CFD and revised model.

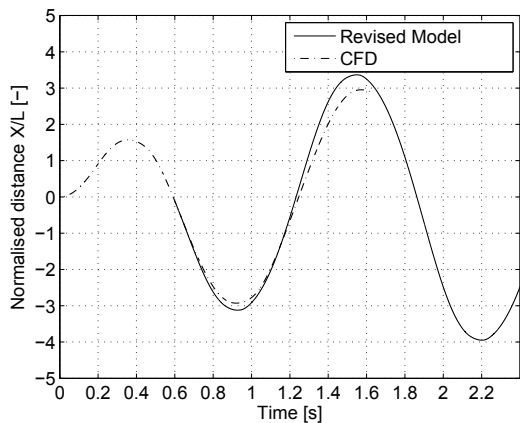


Figure 7.16. Normalised x-coordinate as function of time for CFD and revised model.

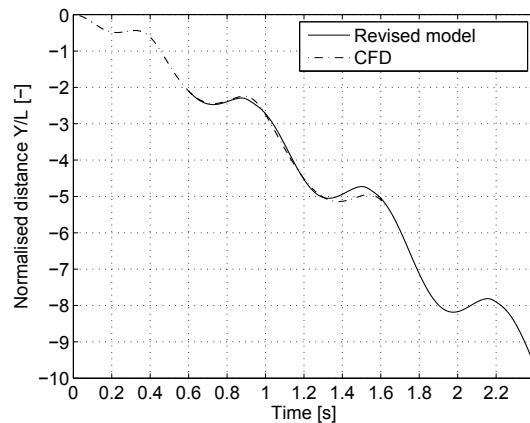


Figure 7.17. Normalised y-coordinate as function of time for CFD and revised model.

7.4.1 Deviations in x-position as function of time

Figure 7.14 presents how the model is fully capable of predicting most of the trajectory with high accuracy. The model does however underestimate the extreme x-positions during the turns. This is evident from Figure 7.16. Figure 7.18 shows the deviation in terms of the normalised x-position as function of time for the free fall in the time interval between $t = 0.6$ s and $t = 1.6$ s.

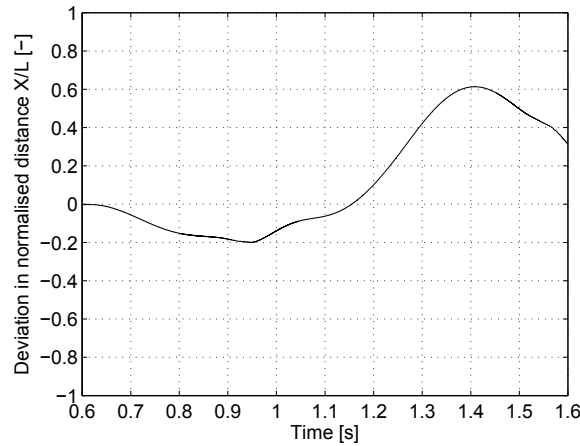


Figure 7.18. Deviation in normalised x-position between CFD and revised model.

Figure 7.18 indicates a maximum deviation of $X/L = 0.62$ between the CFD simulation and model at $t = 0.4$ s, even though the deviation is generally in the order of $X/L = 0.2$ to $X/L = 0.3$. These small deviations can be explained by unsteady effects which have not been included in the model. Such effects include vortices being shed from the plate edges as the plate turns, and the fluid continuing past the plate as it is decelerated before the turn. The CFD simulations presented in Figure 3.18 and Figure 3.19 suggest these effects to be important when the plate is translational accelerated or decelerated.

7.4.2 Deviations in y-position as function of time

Both the revised model and CFD simulation predict the centre of mass to elevate during the free fall, as visualised in Figure 7.17. For the second turn, the CFD model suggests a normalised elevation height $\Delta(Y/L)_{\text{elev}}$ of $Y/L = 0.20$, whereas the model predicts an elevation height of $Y/L = 0.18$. The deviation in the normalised y-position as function of time is shown in Figure 7.19.

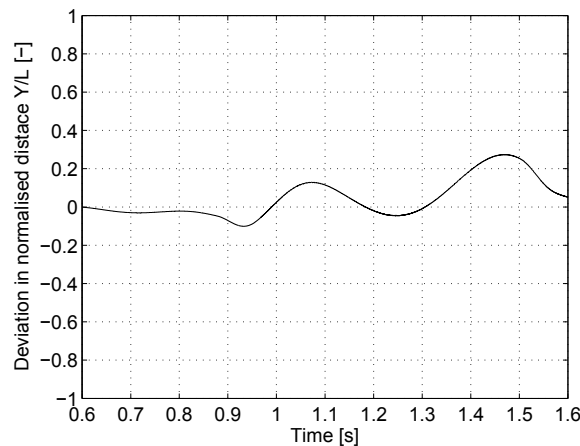


Figure 7.19. Deviation in normalised y-position between CFD and revised model.

Figure 7.19 shows how the revised model is capable of predicting the normalised y-position within a deviation of $Y/L = 0.3$ from the CFD simulation.

The fact that the model generally predicts a higher centre of mass elevation than the CFD simulation, suggests that the lift coefficient might be overestimated in the model. One way to

cope with this is by performing a set of even more detailed rotational lift simulations varying the rotational velocities and accelerations at different translational velocities.

7.4.3 Deviations in orientation angle as function of time

Figure 7.15 is used for comparing the orientation angle as function of time for the CFD simulation and the model. The figure shows how the model systematically underestimates the turning angles. This is also evident from Figure 7.20 showing the deviation in orientation angle between the revised model and the free fall CFD simulation.

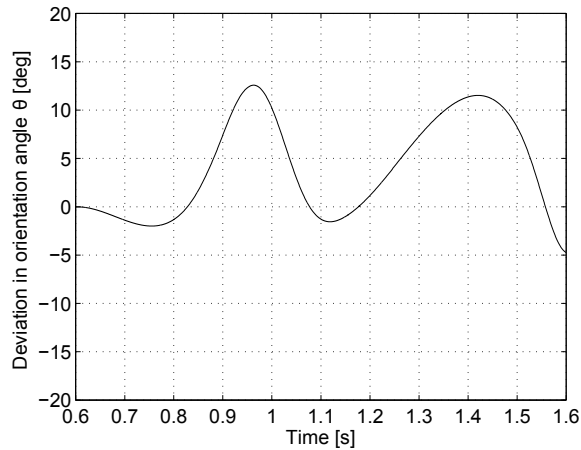


Figure 7.20. Deviation in orientation angle between CFD and revised model.

As Figure 7.20 indicates, the orientation angle predicted by CFD and the revised model deviates at maximum 12.5 deg. The turn angle in the first turn deviates approximately 12.5 deg suggesting the model not being fully capable of predicting the torques on the plate. This deviation can be explained by unsteady effects such as fluid moving with the plate as it translates during its long horizontal gliding motion and continuing as the plate is decelerated. This effects is illustrated in Figure 7.21 by a contour plot of x-velocity for the CFD simulation during the turn at $t = 0.90$ s. The plate has entered from the right-hand side.

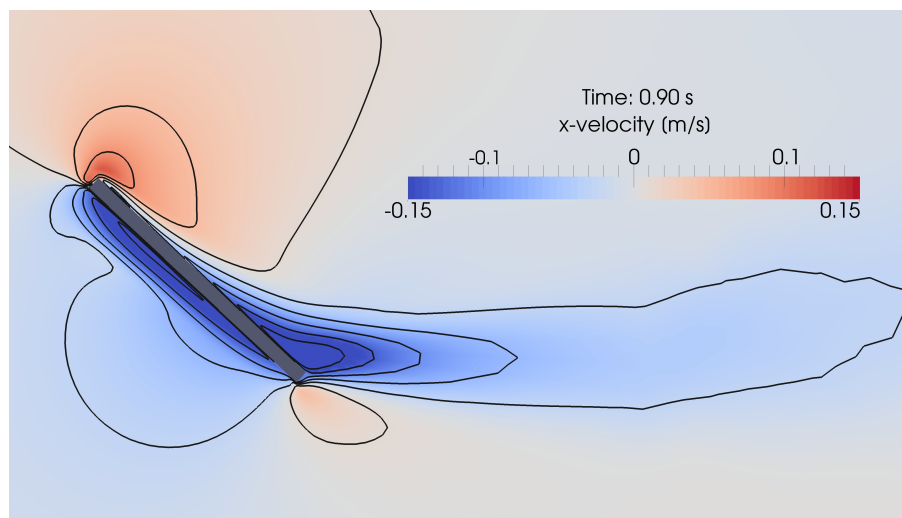


Figure 7.21. Fluid continuing past the plate as it is decelerated during a turn resulting in a negative torque and a higher turning angle than predicted by the revised model.

The fluid moving in the negative x -direction as shown in the figure is expected to contribute with a negative torque resulting in a higher turning angle before the plate moves in the opposite direction. Even though the revised model could be improved by inclusion of different unsteady effects, it is generally considered capable of predicting the free fall trajectory. The code of the revised model is attached in Enclosure B and on the CD presented in Appendix I.

So far, the free fall trajectory of a single plate with well-defined dimensions and density moving in a specific fluid has been investigated experimentally, by CFD simulations, and by a revised model. In the following, the model is used to predict the free fall behaviour of other plates falling in different media.

7.5 Extending the Model Capabilities to Other Flat Plates

This work has until now been focused on the motion of a specific aluminium plate with density $\rho_p = 2700 \text{ kg/m}^3$, length $L = 40 \text{ mm}$, and height $h = 2 \text{ mm}$ falling freely in water at $T = 20^\circ\text{C}$.

To extend the modelling of a framework for flat plates in general, the validity of the revised model has to be investigated for a wide range of flat plates with different densities, dimensions, and falling in different fluids. As experimental based validation would require a substantial amount of experiments, it is out of scope of this present work.

Even though the model has only been validated for the exact aluminium plate investigated in this project, it is of interest if the revised model is able to simulate the motion of different plates. In the figure on the following page, free fall trajectories of plates with different densities falling in water at 20°C are shown. Along with the trajectories are the Reynolds number defined by Equation (1.5) and the dimensionless moment of inertia defined by Equation (1.4). Note the trajectories remain non-validated but simply serve to show different types of trajectories.

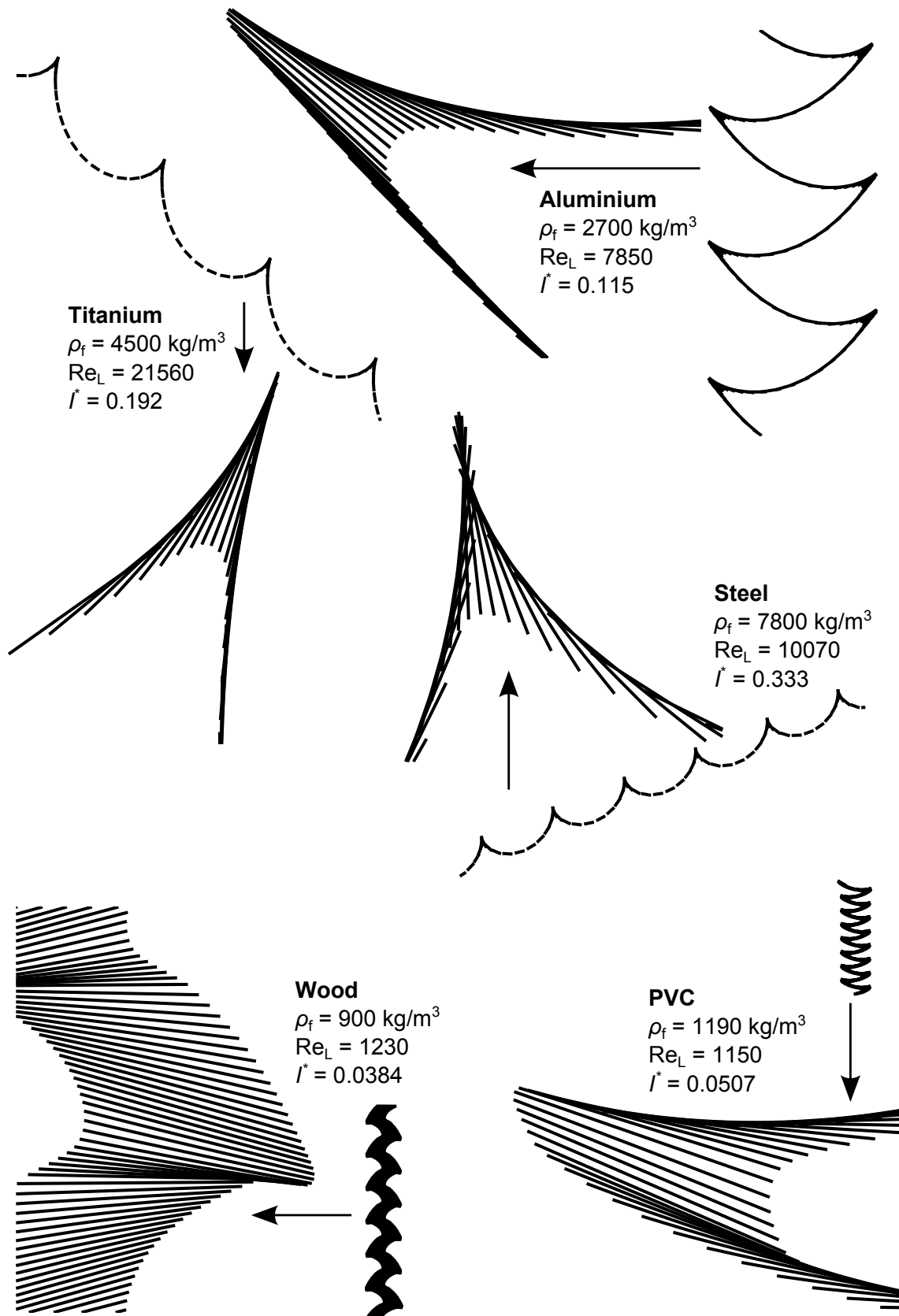


Figure 7.22. Examples of free fall or rise trajectories for different materials in water. The Reynolds number is based on the apparent terminal velocity and the plate length. The dimensionless moments of inertia are calculated by Equation (1.4) on page 4. All plates have a length of 40 mm and an aspect ratio of 20. Note that the trajectories are not equally scaled so a exact comparison should not be made.

The different trajectories in Figure 7.22 show that the model is capable of modelling the motion of flat plates falling in different regimes. Even though experimental validation will not be carried out in this present study, the transitions between periodic oscillation motion, tumbling motion, and steady falling motion can be compared to motion regimes maps found in literature. This comparison will be based on two dimensionless number, namely the Reynolds number and dimensionless moment of inertia. A such study is presented in the following subsection.

7.5.1 On the Validity of the Revised Model Using Motion Regimes

As presented in the introduction, the trajectories for flat plates in free fall can in general be classified into different categories. To generalise the trajectories, the dimensionless Reynolds number and non-dimensionalised moment of inertia are used. The model presented in throughout this work has been used to make an extensive parameter variation and investigate the type of motion for different plates. Figure 7.23 shows the results of the parameter variation in terms of Reynolds number, dimensionless moment of inertia and the corresponding type of motion.

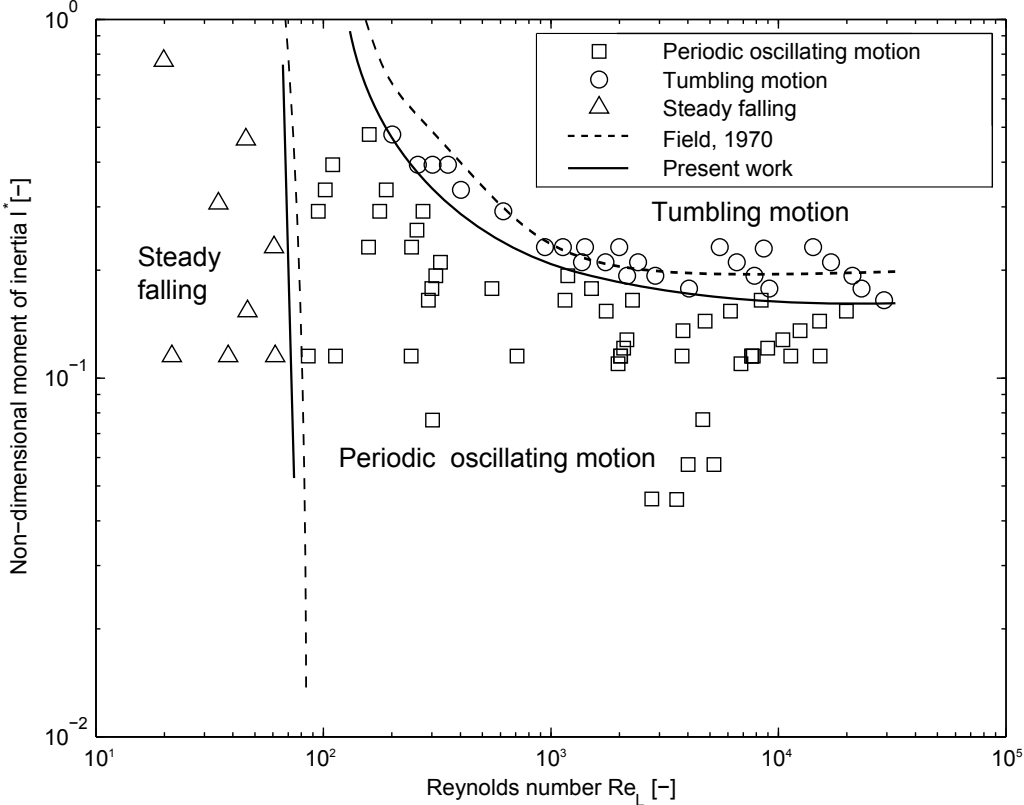


Figure 7.23. Motion regime plot suggested by the revised model presented throughout this work.

The figure indicates that the model is generally capable of recreating the motion regime map presented by Smith (1970). Even though the exact borders are not coincident, the general pattern is the same. Furthermore, the borders presented by Smith (1970) rely on a limited number of experiments as shown in Figure 1.4 on page 5. To further validate the exact borders, the capabilities of the model in relation to different plates will have to be quantified through experimental work. Such an extensive experimental validation is out scope of this present work.

Chapter 8

Closure

8.1 Conclusions

This work presents a numerical and experimental investigation of unsteady aerodynamics related to flat plates. Based on existing modelling framework for flat plates, a revised 2D model has been proposed. The existing modelling framework has proven to be insufficient to predict the plate trajectories within a reasonable margin of accuracy. The deficiencies in the model using the existing modelling framework are found to be rotational lift and rotational drag. Furthermore, the centre of pressure location for a flat plate have been found to differ significantly from the commonly used value of $0.25 \cdot L$ for airfoils. These three parameters of lift, drag and location of centre of pressure have been investigated in details and new correlations have been proposed. This has resulted in a model capable of predicting the motion regime for a wide range of flat plates in free fall.

Conventionally, the drag coefficient for non-spherical particles is modelled using a blending function including both the angle of attack and the Reynolds number. The shape of a blending function suggested by Rosendahl (2000) for cylindrical objects has been validated for a flat plate by a set of CFD simulations. It was found applicable for the modelling of flat plates. Thus, this approach has been used to model the drag coefficient on flat plates in free fall. Furthermore, a set of CFD simulations were carried out to determine the drag coefficient for a plate at $\alpha = 0$ deg and $\alpha = 90$ deg for Reynolds numbers ranging from 5 to 20000. This resulted in a new set of correlations, which have contributed to the model developed in this work. Additionally, based on a conclusion by Pesavento (2006), the traditional drag coefficient formulation, has been extended to include the rotational velocity of the plate by taking the time derivative angle of attack into account.

Similarly, the results of a set of CFD simulations were used to describe the translational lift coefficient as function of angle of attack at a fixed Reynolds number of 10000. The results of the simulations show good correspondence with the results presented by Brunton and Rowley (2011) at a Reynolds number of 100. Therefore, no further work has been dedicated to investigate the Reynolds number dependency of the translational lift coefficient. To include rotational dependencies as suggested by Pesavento (2006), a set of CFD simulations were carried out. The results of the CFD simulations suggested a delay in the stall point when the rotational velocity is increased and thereby enhanced lift compared to the traditional formulation. The traditional lift coefficient formulation has therefore been extended by a set of new correlations to take the enhanced lift due to rotation into account.

It was attempted to determine an added mass coefficient matrix formulation for a flat plate using an approach suggested by Simcik et al. (2008), who successfully validated the added mass coefficient for a sphere using this approach. The matrix coefficients for the plate were found to be $C_{11} = 0.0731$, $C_{22} = 17.3$, and $C_{66} = 7.03$ based on a CFD simulation. This indicates added mass effects to be important when the plate is accelerated perpendicular to its long edge and almost negligible when the plate is accelerated parallel to its long edge. Furthermore, the high C_{66} value suggests added mass effects to be important to successfully describe the rotational motion of the plate. However, inclusion of the matrix failed to improve the model and was not used further.

CFD simulations of a falling plate using the 6DOF solver with a dynamic mesh showed great correspondence with experimental results obtained by digital video camera recordings of the trajectory. The orientation angle in the second and third turn deviates by 2.0 % and 3.9 % respectively, suggesting the CFD model to be fully capable of simulating a flat plate in free fall. When comparing the normalised x-distance as function of time, the CFD simulation deviates by 18.9 % and 18.7 %, which can be explained by the experiment not being fully two-dimensional. Overall, the CFD simulation is considered capable of predicting the detailed time dependent coupled velocity and pressure field around the plate in free fall, hence resulting in reliable details on the net force and torque on the plate.

Based on the validated free fall CFD simulation, details on the centre of pressure location were extracted. The aerodynamic forces on a flat plate act through a point close to $0.015 \cdot L$ instead of the traditionally accepted $0.25 \cdot L$ for translating airfoils. Based on this information alone, a new correlation was proposed to describe the centre of pressure location for various angles of attack.

The new correlations for rotational lift, rotational drag, and centre of pressure were included in the revised model. These new correlations significantly improved the ability of the model to successfully model the free fall trajectory. The revised model under-estimates the orientation angles in the turns, suggesting unsteady forces to add a torque contribution not taken into account. Both the normalised x- and y-position are predicted within reasonable accuracy suggesting the model to be capable of predicting a larger part of the trajectory.

To investigate the capability of the model to predict the free fall trajectory for flat plates in general, the results were compared to the regime map presented by Smith (1970). The revised model generally validated the transitions from periodic oscillation, tumbling motion and steady falling motion suggested by Smith (1970). Further validation is needed to ensure accuracy of the model in all regimes. However, the agreement between the regime plot by Smith (1970) indicates that the model generally enables computationally inexpensive prediction of the motion of flat plates in free fall, and thereby improves the existing modelling framework significantly.

8.2 Suggestions for Further Work and Discussion

This section gives suggestions on future work to be done in relation to the work presented in this project.

Extensive Experimental Validation for Various Plates

The modelling framework presented throughout the present work has only been validated for an aluminium plate with an aspect ratio of 1/20 falling in water. Figure 7.23 on page 86 does however suggest that the model is capable of predicting the motion of different plates due to the general formulation used in the model. To include the modelling framework presented in this work in a Euler-Lagrange formulation in a CFD software suite, more in depth validation is required. Especially the motion in the different regimes will have to be validated experimentally.

Inclusion of Proposed Modelling Framework in CFD Software

To successfully utilise the modelling framework presented in this work in a CFD software suite some coding is required. Since the source code is not available in the commercial software from ANSYS, an UDF could be written for this purpose. Another approach would be to include it in the open-source CFD toolbox OpenFOAM, where the modelling framework can be included directly in the source code (OpenFOAM Foundation, 2014).

Investigation of Magnus and Saffman's Lift Force

The Magnus lift force due to rotation of an object has not been included in the modelling framework proposed in this work. Even though this lift force contribution can be neglected for the periodic oscillation motion, it might play a more dominant role when the plate rotates heavily while translating at a low velocity. Additionally, the Saffman's lift force has not been included. This contribution is not important for flat plates in a stagnant fluid, but if the flow has a shear velocity, it is expected to play a major role.

Investigation of Torque due to Resistance Towards Rotation

A simple constant coefficient of 2 has been used in the proposed modelling framework to include a torque contribution due to the rotational motion of the plate. Just like the drag and lift coefficients, this coefficient is not expected to be constant but rather a function of a rotational based Reynolds number. Further investigation into this coefficient of resistance towards rotation are of utmost importance, since the sensitivity analysis in Appendix D shows changes in the result with a change of the coefficient of $\pm 10\%$. The result indicates that larger changes in the coefficient will significantly affect the results of the revised model.

Further Investigation of Rotational Effects

In this present work, rotational lift and drag coefficient correlations have been proposed. These correlations can be improved to take rotational velocities higher than 90 deg/s into account. The CFD model suggests the rotational velocity to be much higher in the turns, suggesting that the revised model can be even further improved by including a wider range of rotational velocities. This could explain the deficiencies in the revised model to predict the exact trajectory during the turns.

References

- Andersen, Pesavento, and Wang, 2005a.** A. Andersen, U. Pesavento, and Z. Jane Wang. *Unsteady aerodynamics of fluttering and tumbling plates*. J. Fluid Mech, 541, 65–90, 2005.
- Andersen, Pesavento, and Wang, 2005b.** A. Andersen, U. Pesavento, and Z. Jane Wang. *Analysis of transition between fluttering, tumbling and steady descent of falling cards*. J. Fluid Mech, 541, 91–104, 2005.
- ANSYS, Inc., 2006.** ANSYS, Inc. *Chapter 14 - Reporting Mesh Statistics*, 2006.
- ANSYS, Inc., 2011a.** ANSYS, Inc. *Turbulence Modeling*. 275 Technology Drive, Canonsburg, PA 15317, U.S.A., 2011. Brochure attached on the CD.
- ANSYS, Inc., 2011b.** ANSYS, Inc. *ANSYS FLUENT Theory Guide*, 2011.
- ANSYS, Inc., 2011c.** ANSYS, Inc. *ANSYS FLUENT User's Guide*, 2011.
- Baker, 1983.** A. J. Baker. *Finite Element Computational Fluid Mechanics*. Hemisphere Publishing Company, 1983. ISBN: 978-0-070-03465-5.
- Belmonte, Eisenberg, and Moses, 1998.** Andrew Belmonte, Hagai Eisenberg, and Elisha Moses. *From Flutter to Tumble: Inertial Drag and Froude Similarity in Falling Paper*. Physical Review Letters, 81, 345–348, 1998.
- Brennen, 1982.** C. E. Brennen. *A Review of Added Mass and Fluid Inertial Forces*, Naval Civil Engineering Laboratory, 1982. Report number: CR 82.010.
- Brunton and Rowley, 2011.** Steven L. Brunton and Clarence W. Rowley. *Low-dimensional state-space representation for classical unsteady aerodynamic models*. Princeton University, 2011.
- Cengel, Turner, and Cimbala, 2008.** Yunus A. Cengel, Robert H. Turner, and John M. Cimbala. *Fundamentals of Thermal-Fluid Sciences*. McGraw-Hill, 2008. ISBN: 978-007-126631.
- Clift, Grace, and Weber, 1978.** Roland Clift, John Grace, and Martin E. Weber. *Bubbles, Drops and Particles*. Dover Publications, 1978. ISBN: 0-486-44580-1.
- Crowe, Sommerfeld, and Tsuji, 1998.** Clayton Crowe, Martin Sommerfeld, and Yutake Tsuji. *Multiphase Flows with Droplets and Particles*. CRC Press, 1998. ISBN: 0-8493-9469-4.
- ERCOFTAC, January 2000.** ERCOFTAC. *Best Practice Guidelines*, European Research Community On Flow, Turbulence and Combustion, January 2000.

- Ericsson and Reding, 1988.** L. E. Ericsson and J.P. Reding. *Fluid mechanics of dynamic stall part 1 - Unsteady flow concepts*. Journal of Fluids and Structures, 2, 1–33, 1988.
- Field, Klaus, Moore, and Nori, 1997.** Stuart B. Field, M. Klaus, M. G. Moore, and Franco Nori. *Chaotic dynamics of falling disks*. Nature, 388, 252–254, 1997.
- Gharali and Johnson, 2013.** Kobra Gharali and David A. Johnson. *Dynamic stall simulation of a pitching airfoil under unsteady freestream velocity*. Journal of Fluids and Structures, 42, 228–244, 2013.
- Granlund and Michael, 2013.** Kenneth O. Granlund and Michael. *Unsteady pitching flat plates*. J. Fluid. Mech., 733, R5 1–13, 2013.
- Green, 1995.** Sheldon I. Green. *Fluid Vortices - Fluid Mechanics and Its Applications*. Kluwer Academic Publishers, 1995. ISBN: 0-7923-3376-4.
- Haider and Levenspiel, 1989.** A. Haider and O. Levenspiel. *Drag coefficient and Terminal Velocity of Spherical and Nonspherical Particles*. Powder Technology, 58, 63–70, 1989.
- Hargreaves, Kakimpa, and Owen, 2014.** D. M. Hargreaves, B. Kakimpa, and J. S. Owen. *The computational fluid dynamics modelling of the autorotation of square, flat plates*. Journal of Fluids and Structures, 46, 111–133, 2014.
- Hoerner, 1965.** Sighard F. Hoerner. *Fluid-Dynamic Drag*. Published by the Author, 1965. no ISBN.
- Houghton and Carpenter, 2003.** E. L. Houghton and P. W. Carpenter. *Aerodynamics for Engineering Students*. Elsevier, 2003. ISBN: 0-7606-5111-3.
- Iversen, 1979.** J. D. Iversen. *Autorotating flat-plate wings: the effect of the moment of inertia, geometry and Reynolds number*. Journal of Fluid Mechanics, 92, 327–348, 1979.
- Jin and Xu, 2008.** Changqiu Jin and Kun Xu. *Numerical Study of the Unsteady Aerodynamics of Freely Falling Plates*. Commun. Comput. Phys., 3, 834–851, 2008.
- Lee and Gerontakos, 2004.** T. Lee and P. Gerontakos. *Investigation of flow over an oscillating airfoil*. J. Fluid. Mech., 512, 313–341, 2004.
- Mandø and Rosendahl, 2010.** Mathias Mandø and Lasse Rosendahl. *On the motion of non-spherical particles at high Reynolds numbers*. Powder Technology, 202, 1–13, 2010.
- Marchildon, Clamen, and Gauvin, 1964.** E. K. Marchildon, A. Clamen, and W. H. Gauvin. *Drag and Oscillatory Motion of Freely Falling Cylindrical Particles*. Canadian Journal of Chemical Engineering, 42, 178–182, 1964.
- Maxwell, 1853.** James Clerk Maxwell. *On a particular case of the descent of a heavy body in a resisting medium*. Cambridge and Dublin Mathematical Journal, 9, 115–118, 1853.
- Meriam and Kraige, 2007.** J. L. Meriam and L. G. Kraige. *Engineering Mechanics - Dynamics*, volume 2. John Wiley & Sons, 6. edition, 2007. ISBN: 978-0-471-78703-7.
- Morsi and Alexander, 1972.** S. A. Morsi and A. J. Alexander. *An investigation of particle trajectories in two-phase flow systems*. J. Fluid Mech., 55, 193–208, 1972.

- Munson, Young, Okiishi, and Huebsch, 2010.** Bruce R. Munson, Donald F. Young, Ted H. Okiishi, and Wade W. Huebsch. *Fundamentals of Fluid Mechanics*. John Wiley & Sons, 2010. ISBN: 978-0-470-39881-4.
- OpenFOAM Foundation, 2014.** OpenFOAM Foundation. *OpenFOAM - The Open Source CFD Toolbox - User Guide*, 2014. Version 2.3.0, 5th February 2014.
- Panda and Zaman, 1994.** J. Panda and K.B.M.Q. Zaman. *Experimental investigation of the flow field of an oscillating airfoil and estimation of lift from wake surveys*. *J. Fluid. Mech.*, 265, 65–95, 1994.
- Pesavento, 2006.** Umberto Pesavento. *Unsteady Aerodynamics of Falling Plates*. Cornell University, 2006. PhD thesis.
- Riabouchinsky, 1935.** D. P. Riabouchinsky. *Thirty years of theoretical and experimental research in fluid mechanics*. *Journal of Royal Aeronautical Society*, 39, 282–348, 1935.
- Richter and Nikrityuk, 2013.** Andreas Richter and Petr A. Nikrityuk. *New correlations for heat and fluid flow past ellipsoidal and cubic particles at different angles of attack*. *Powder Technology*, 249, 463–474, 2013.
- Rosendahl, 1998.** Lasse Rosendahl. *Extending the Modelling Framework for Gas-particle Systems - Applications of Multiparameter Shape Descriptions to Non-conventional Solid Fuels in Reacting and Non-reacting Environment*. Aalborg University, Institute of Energy Engineering, 1998. PhD thesis, ISBN: 87-89179-25-0.
- Rosendahl, 2000.** Lasse Rosendahl. *Using a multi-parameter particle shape description to predict the motion of non-spherical shapes in swirling flow*. *Applied Mathematical Modelling*, 1, 11–25, 2000.
- Saffman, 1965.** P. G. Saffman. *The lift on a small sphere in a slow shear flow*. *J. Fluid Mech.*, 22, 385–400, 1965.
- Simcik and Ruzicka, 2013.** M. Simcik and M.C. Ruzicka. *Added mass of dispersed particles by CFD: Further results*. *Chemical Engineering Science*, 97, 366–375, 2013.
- Simcik, Ruzicka, and Drahos, 2008.** M. Simcik, M.C. Ruzicka, and J. Drahos. *Computing the added mass of dispersed particles*. *Chemical Engineering Science*, 63, 4580–4595, 2008.
- Smith, July 1970.** Edmund H. Smith. *Autorotating Wings: An Experimental Investigation*, The University of Michigan, Department of Aerospace Engineering, July 1970.
- Tanabe and Kaneko, 1994.** Yoshihiro Tanabe and Kunihiko Kaneko. *Behaviour of a Falling Paper*. *Physical Review Letters*, 73, 1372–1377, 1994.
- Tanabe and Kaneko, 1995.** Yoshihiro Tanabe and Kunihiko Kaneko. *Comment on Behaviour of a Falling Paper*. *Physical Review Letters*, 75, 1420, 1995.
- Tomiyama, Sou, Zun, Kanami, and Sakaguchi, 1995.** A. Tomiyama, A. Sou, I. Zun, N. Kanami, and T. Sakaguchi. *Effects of Eötvös Number and Dimensionless Liquid Volumetric Flux on Lateral Motion of a Bubble in a Laminar Duct Flow*. *Multiphase Flow*, pages 3–15, 1995.

- Versteeg and Malalasekera, 2007.** H. K. Versteeg and W. Malalasekera. *An Introduction to Computational Fluid Dynamics - The Finite Volume Method*. Pearson Prentice Hall, 2007. ISBN: 978-0-13-127498-3.
- Wadell, 1935.** Hakon Wadell. *Volume, Shape, and Roundness of Quartz Particles*. *Journal of Geology*, 1, 250–280, 1935.
- Walpole, Myers, Myers, and Ye, 2012.** Ronald E. Walpole, Raymond H. Myers, Sharon L. Myers, and Keying Ye. *Probability & Statistics - For Engineers and Scientists*. Pearson, 2012. ISBN: 978-0-321-74823-2.
- Willmarth, Hawk, and Harvey, 1964.** William W. Willmarth, Norman E. Hawk, and Robert L. Harvey. *Steady and Unsteady Motions and Wakes of Freely Falling Disks*. *The Physics of Fluids*, 7, 197–208, 1964.
- Yin, Rosendahl, Kær, and Condra, 2004.** Chugen Yin, Lasse Rosendahl, Søren K. Kær, and Thomas J. Condra. *Use of numerical modeling in design for co-firing biomass in wall-fired burners*. *Chemical Engineering Science*, 59, 3281–3292, 2004.
- Yin, Rosendahl, Kær, and Sørensen, 2003.** Chungen Yin, Lasse Rosendahl, Søren Knudsen Kær, and Henrik Sørensen. *Modelling the motion of cylindrical particles in a nonuniform flow*. *Chemical Engineering Science*, 58, 3489–3498, 2003.
- Zastawny, Mallouppas, Zhao, and Wachem, 2012.** Marian Zastawny, George Mallouppas, Fan Zhao, and Berend van Wachem. *Derivation of drag and lift force and torque coefficients for non-spherical particles in flows*. *International Journal of Multiphase Flow*, 39, 227–239, 2012.

List of Appendices

- A Numerical Investigation of Translational Drag and Lift Coefficients
- B Numerical Investigation of Added Mass Coefficient Matrix
- C Numerical Investigation of History Force
- D Sensitivity Analysis of Revised Model Results
- E Logical Statements to Determine the Sign of Centre of Pressure Location
- F Details on Dynamic Meshes
- G Numerical Investigation of Rotational Drag and Lift Coefficients
- H Detailed CFD Results
- I CD Content

Appendix A

Numerical Investigation of Translational Drag and Lift Coefficients

This appendix contains information on a numerical investigation of the translational drag- and lift coefficients for flat plates. Both the dependency of angle of attack and Reynolds number will be investigated.

The purpose of the simulations is twofold. Firstly, the lift- and drag coefficients for flat plates at different angles of attack and a Reynolds number of 10000 are determined. Secondly, the lift- and drag coefficients at angles of attack of 0 deg and 90 deg are found for a wide range of Reynolds numbers. The two investigations are presented in Section A.1 and Section A.2 respectively.

The simulations are configured in a way similar to the one presented in Chapter 4. That is, the SST transition turbulence model is used to model turbulence, the boundary layer mesh is the same with the same first cell height, and the time step size is the same. The domain does however vary. Figure A.1 shows the domain along with the boundary conditions used for these simulations.

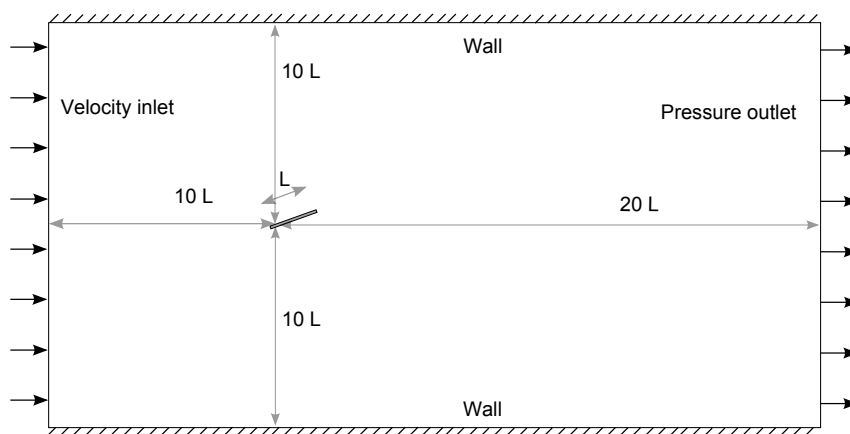


Figure A.1. Domain used for simulations to determine the lift- and drag coefficients of the plate at different angles of attack and Reynolds numbers.

A.1 Translational Lift and Drag as Function of Angle of Attack

To estimate the lift coefficient as a function of the angle of attack, seven simulations are made, each simulation with a different angle of attack ranging from 0 deg to 90 deg and at a Reynolds number of 10000. Figure A.2 illustrates how the plate is inclined to the fluid flow resulting in an angle of attack α .

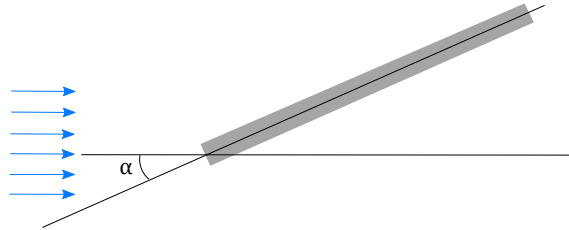


Figure A.2. Plate inclined to the flow resulting in an angle of attack α .

The results in terms of drag and lift coefficients as a function of the angle of attack are presented in Figure A.3 and Figure A.4 respectively.

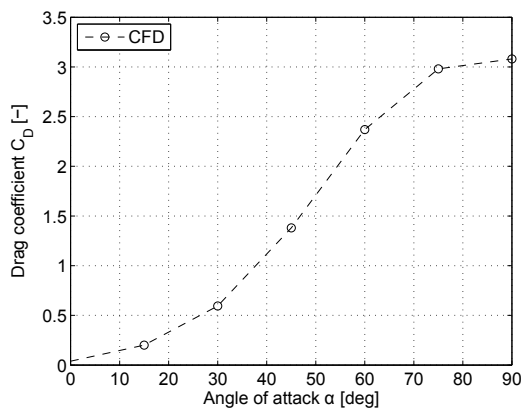


Figure A.3. Drag coefficient as a function of angle of attack at $Re_L = 10000$.

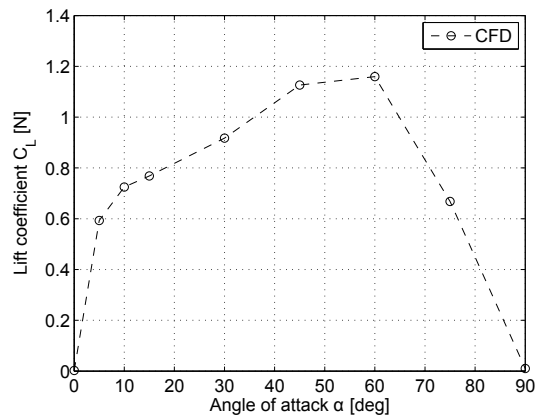


Figure A.4. Lift coefficient as a function of angle of attack at $Re_L = 10000$.

The shape of the functions correspond quite well to the one presented in literature and referred to in Chapter 3.

When the plate was inclined to over 30 deg, vortex shedding occurred. As a results, the simulations did not fully converge to the criteria set resulting in residuals oscillating in time instead.

In order to model the drag coefficient at different angles of attack as well as Reynolds numbers, the blending functions presented in Chapter 3 on page 21 are used. To increase the accuracy of this approach, the drag coefficients at $\alpha = 0$ deg and $\alpha = 90$ deg are of interest for a wide range of Reynolds numbers. The following section describes a such set of simulations.

A.2 Translational Lift and Drag as Function of Reynolds Number

The previous section suggests the drag coefficient as a function of the angle of attack to have a shape similar to the shape of the blending functions suggested by Pesavento (2006) and Rosendahl (2000). Therefore, it is assumed that these blending functions can be used in the quasi-steady model developed in the present work. The correlations by Pesavento (2006) and

Rosendahl (2000) are a function of the drag coefficient at angles of attack of 0 deg and 90 deg, thus $C_D(0)$ and $C_D(90)$ are of interest for different Reynolds numbers Re_L . These two extreme positions are illustrated in Figure A.5.

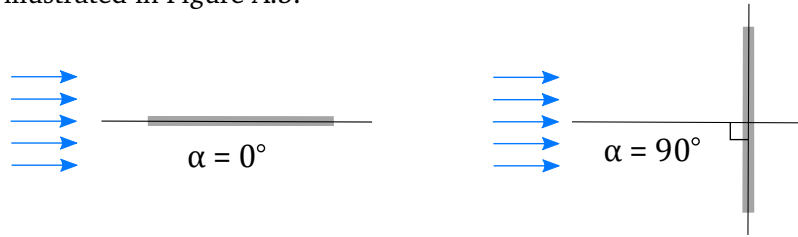


Figure A.5. Extreme position at $\alpha = 0$ deg and $\alpha = 90$ deg of interest in the CFD simulations for different Reynolds numbers.

The investigated Reynolds numbers range from $Re_L = 5$ to $Re_L = 20000$. The results of the simulations are presented in Figure A.6 for $\alpha = 0$ deg and Figure A.7 for $\alpha = 90$ deg.

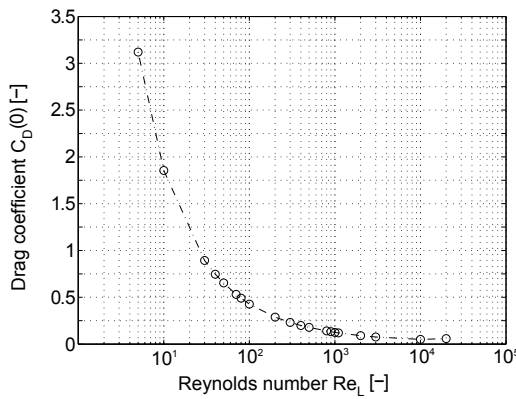


Figure A.6. Drag coefficient for $\alpha = 0$ deg as function of Reynolds number Re_L .

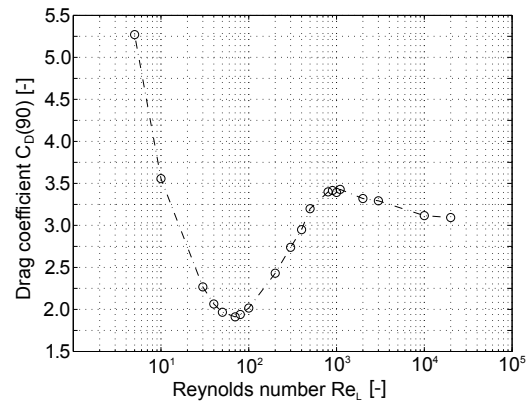


Figure A.7. Drag coefficient for $\alpha = 90$ deg as function of Reynolds number Re_L .

The drag coefficient is high for low Reynolds numbers approaching Stokes flow for both 0 deg and 90 deg angle of attack. $C_D(0)$ decreases as the Reynolds number increases. $C_D(90)$ decreases to a local minimum around $Re_L = 100$. After this it increases and reaches an almost constant value for $Re_L > 1000$.

In Chapter 3 regressions are found for $C_D(0)$ and $C_D(90)$. These regressions are included in the quasi-steady model along with the blending function developed by Rosendahl (2000).

Appendix B

Numerical Investigation of Added Mass Coefficient Matrix

Added mass effects are caused by the surrounding fluid being accelerated with the plate. This appendix describes how a set of numerical CFD simulations are carried out to determine the added mass matrix coefficients. The approach used to determine the coefficients in this appendix is suggested by Simcik et al. (2008) and Simcik and Ruzicka (2013), who suggest applying a well-defined force and measuring the acceleration in the very initial time steps in the order $t = 10^{-4}$ s to $t = 10^{-5}$ s. Since the very initial time steps are considered, the velocity of the plate is sufficiently small so that drag and lift forces can be neglected (Simcik et al., 2008).

The simulations are in general configured in a way similar to the one presented in Chapter 4. The SST transition turbulence model is used to model turbulence, and the boundary layer mesh is the same with the same first cell height. However, the domain and time step size are different in the present simulations. The domain used to determine the added masses and added moment of inertia are presented in Figure B.1 and B.2 respectively. In Figure B.1 a well-defined force is applied to the plate, while in Figure B.2 a well-defined torque is applied on the plate.

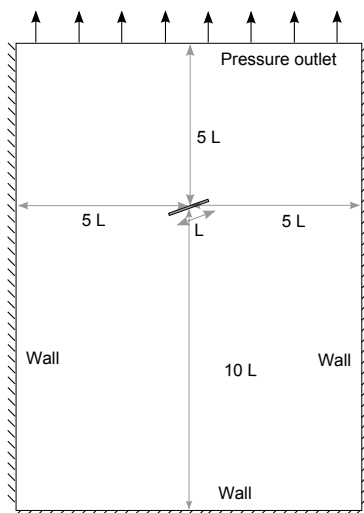


Figure B.1. Domain used to determine the added mass coefficients C_{11} and C_{22} .

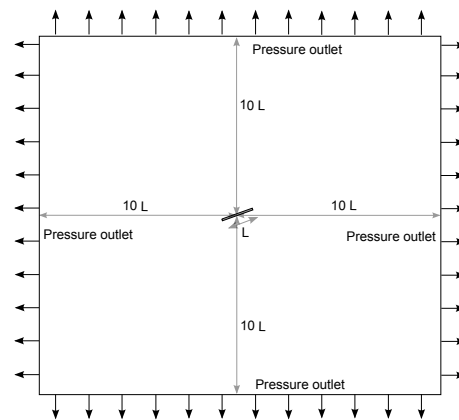


Figure B.2. Domain used to determine the added mass coefficient C_{66} corresponding to an added moment of inertia.

B.1 Added Mass Coefficients C_{11} and C_{22}

A well-defined force is applied to a plate orientated both parallel and perpendicular to the force. The force chosen corresponds to the sum of the buoyancy and gravity force. The results of the simulations are presented in Figure B.3 and Figure B.4. These figures show the position and velocity of the plate as function of time.

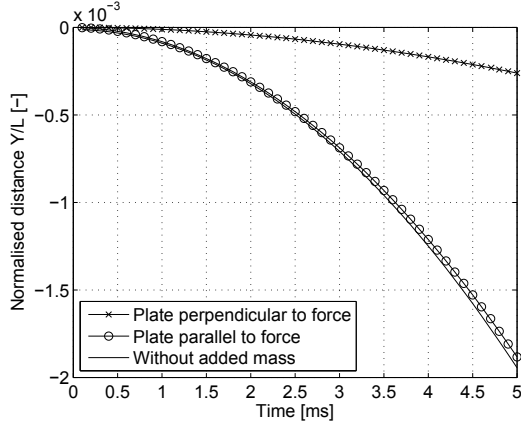


Figure B.3. y-position as function of time for the two plate orientations.

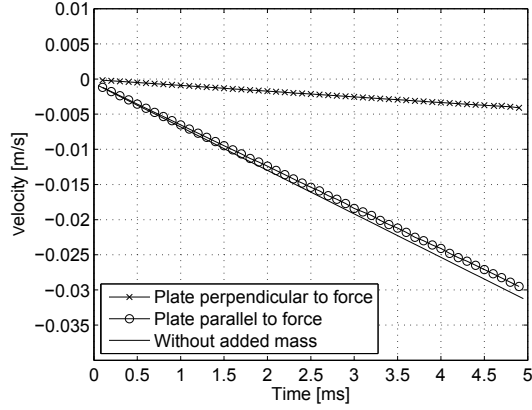


Figure B.4. y-velocity as function of time for the two plate orientations.

Figure B.4 indicates a constant acceleration suggesting drag and lift forces to play a negligible role in the considered initial time steps. For the plate perpendicular to the force the acceleration is -0.84 m/s^2 and for the plate parallel to the force the acceleration is -6.0 m/s^2 . Balancing out the gravity- and buoyancy force, the acceleration without added mass effects would be -6.18 m/s^2 . The decrease in plate acceleration is assumed to be solely due to added mass.

The added mass force is determined from Equation (B.1).

$$\vec{F}_a = -(\vec{F}_b - \vec{F}_g) + m \cdot \vec{a} \quad (\text{B.1})$$

Knowing the added mass force, the added mass coefficient can be determined from Equation (B.2).

$$C = -\frac{\vec{F}_a}{\rho_f \cdot V \cdot \vec{a}} \quad (\text{B.2})$$

The coefficients found are given in Equation (3.29) on page 29. The added mass matrix contains contributions due to both added masses and added moments of inertia. The added moment of inertia coefficient is determined in the following section.

B.2 Added Mass Coefficient C_{66}

A well-defined torque is applied to a plate causing it to rotate about its centre. The free fall CFD simulation results presented in Appendix H suggests torques in the order of 0.001 Nm on the plate in free fall. Therefore, a torque of 0.001 Nm is applied to the plate in the present simulations. The results of the simulations are shown in Figure B.5 and Figure B.6 in terms of orientation angle and angular velocity.

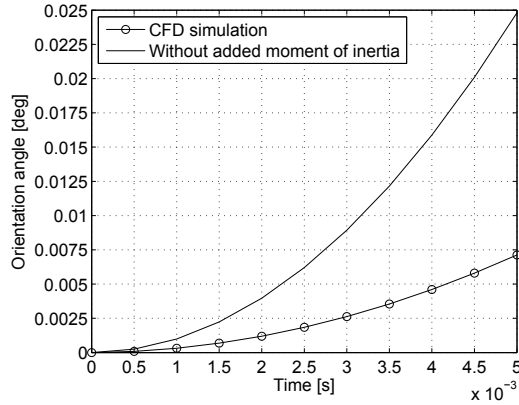


Figure B.5. Orientation angle as function of time.

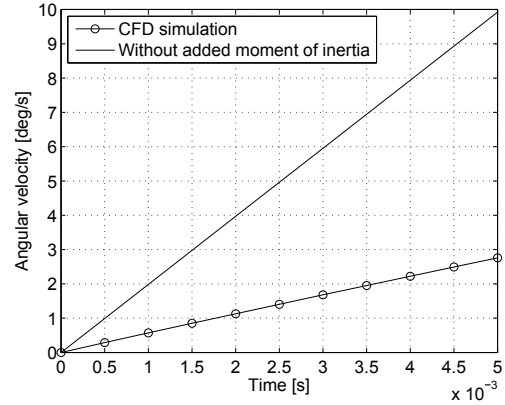


Figure B.6. Angular velocity as function of time.

Figure B.6 indicates a constant angular acceleration suggesting the resistance torque to be negligible in the small time steps considered. The CFD simulation shows an angular acceleration of 551.2 deg/s², whereas the plate would accelerate with 1985 deg/s² without added mass effects. The torque contribution due to an added moment of inertia is found by Equation (B.3).

$$\vec{T}_a = -\vec{T} + I_z \cdot d\omega/dt \quad (\text{B.3})$$

Knowing the added torque, the added moment of inertia coefficient can be determined from Equation (B.4).

$$C_{66} = -\frac{\vec{T}_a}{I_{z,f} \cdot d\omega/dt} \quad (\text{B.4})$$

The coefficient found is given in Equation (3.29) on page 29.

Appendix C

Numerical Investigation of History Force

C.1 Computational Domain and Boundary Conditions

The simulations are configured in a way similar to the one presented in Chapter 4. The SST transition turbulence model is used to model turbulence, and the boundary layer mesh is the same with the same first cell height. The domain used for the simulations is shown in Figure C.1.

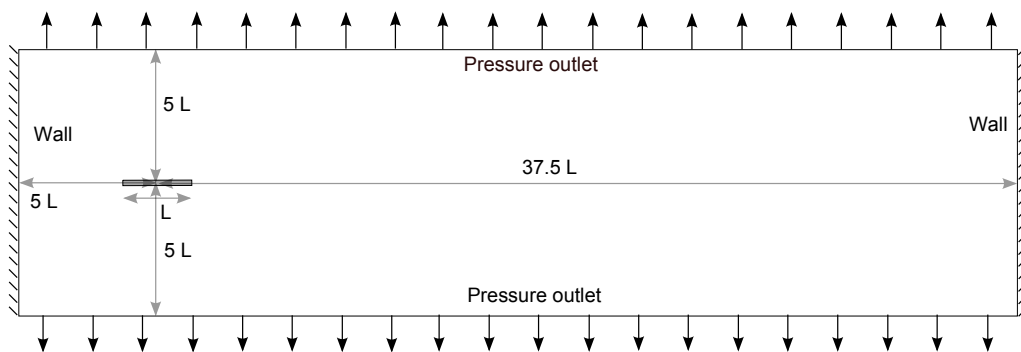


Figure C.1. Domain used to investigate history force effects.

Using the domain in Figure C.1, a plate is accelerated at different accelerations. The following subsection gives an overview of how the motion is prescribed in ANSYS Fluent.

C.1.1 Prescribing the Translational Motion of the Plate

To describe the translational motion of the plate, an UDF is used. This UDF is attached in Enclosure A. Two simulations with different accelerations are made.

In the first simulation the UDF accelerates the plate at 5 m/s^2 for 0.1 s, keeps a constant velocity for 0.5 s, and then decelerates with -5 m/s^2 for 0.1 s. In the second simulation the plate accelerates at 7.5 m/s^2 for 0.0667 s, keeps a constant velocity for 0.5 s, and then decelerates with -7.5 m/s^2 for 0.0667 s. The motion prescribed for the two simulations is shown in Figure C.2. As figure 3.18 and 3.19 on page 30 31 show, the increase in acceleration

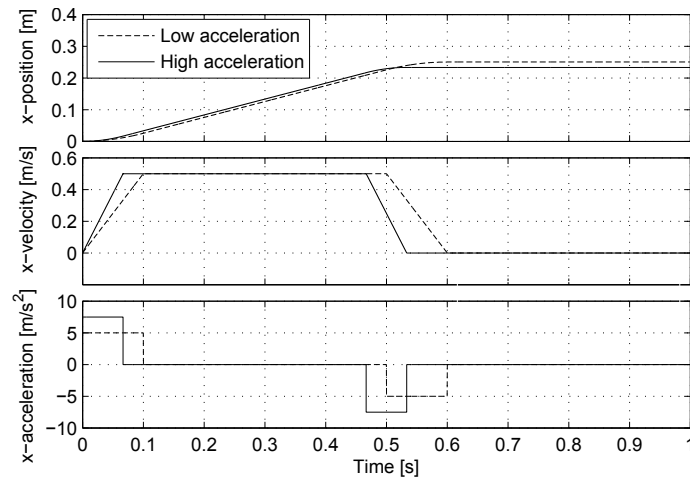


Figure C.2. Prescribed motion for the two CFD simulations.

results in a higher viscous drag. This suggests a deformed boundary layer to play a major role in the description of the viscous forces as expected.

Appendix D

Sensitivity Analysis of Revised Model Results

D.1 Sensitivity Analysis

In the model, the value of a set of parameters remains uncertain. Therefore this appendix presents a sensitivity analysis where the importance of these parameters is investigated in details. Of interest is the magnitude of the maximum centre of pressure location, the shape of the centre of pressure correlation, the resistance torque coefficient, and the added mass.

D.1.1 Magnitude of Maximum Centre of Pressure Location

In literature, the magnitude of the maximum centre of pressure location of airfoils is typically estimated to 25 % of the chord length (Houghton and Carpenter, 2003). However, the results of the simulation of the freely falling plate indicates that the magnitude of the maximum centre of pressure location for the plate in free fall does not exceed 1.5 %. Therefore, this value of 1.5 % is used in the revised model. To investigate the importance of this parameter Figure D.1 is used. In the figure, the parameter is varied by $\pm 10\%$ and shown together with the results of the validated CFD simulation.

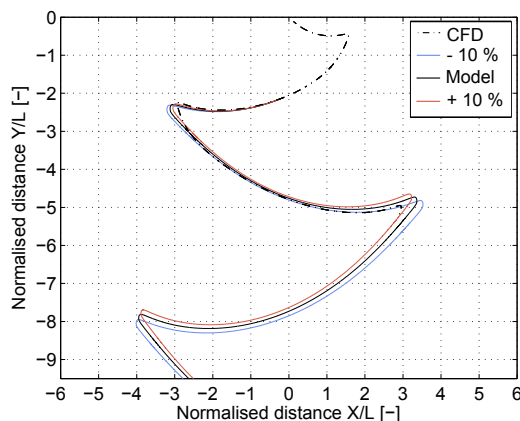


Figure D.1. Plate trajectories obtained by changing the magnitude of the centre of pressure location $\pm 10\%$ from a base of 0.015.

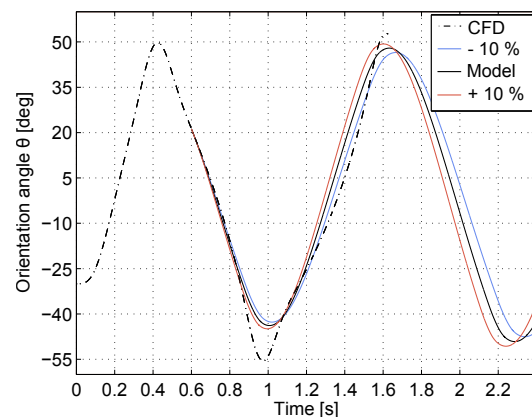


Figure D.2. Orientation angle as function of time changing the magnitude of the centre of pressure location $\pm 10\%$ from a base of 0.015.

As seen in the figures, an increase in the magnitude of the centre of pressure location results in sharper turns. Furthermore, the turning angles are increased as Figure D.2 indicates.

D.1.2 Shape of Centre of Pressure Function

The correlation by Rosendahl (2000) presented in Section 3.3 is used in the model to describe the location of the centre of pressure as a function of the angle of attack. The correlation by Yin et al. (2003) is tested in the model to determine the importance of the choice of correlation. Figure D.3 and D.4 indicate the importance of the function used.

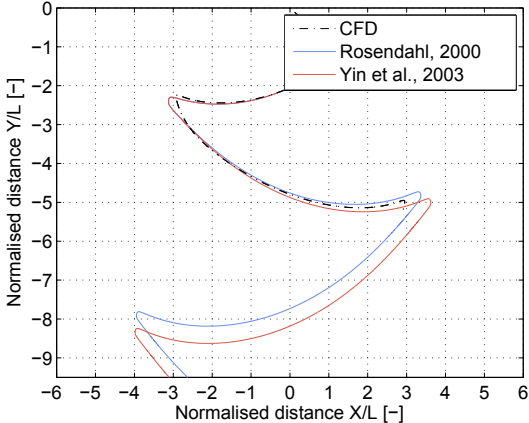


Figure D.3. Plate trajectory as function of time using either the correlation by Rosendahl (2000) or Yin et al. (2003).

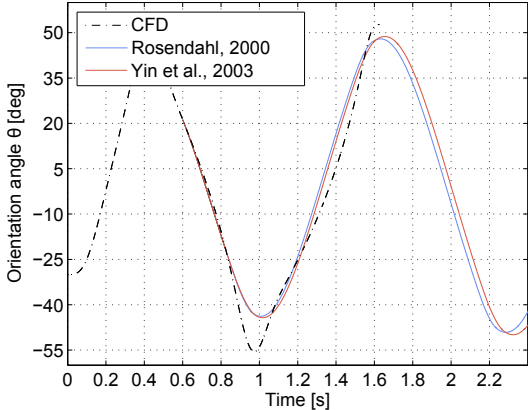


Figure D.4. Orientation angle as function of time using either the correlation by Rosendahl (2000) or Yin et al. (2003).

As the figure shows, the correlation by Rosendahl (2000) generally results in sharper turns. Likewise, it results in lower turning angles.

D.1.3 Coefficient of Resistance Towards Rotation

The coefficient of resistance towards rotation has been changed $\pm 10\%$ from a value of 2. The results are shown in Figure D.5 and Figure D.6.

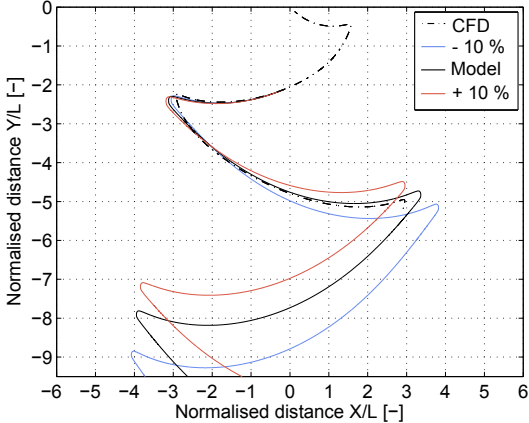


Figure D.5. Plate trajectory changing the coefficient of resistance $\pm 10\%$ from a base of 2.

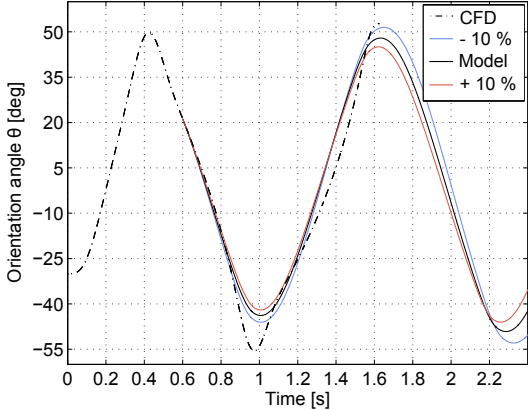


Figure D.6. Orientation in time changing the coefficient of resistance $\pm 10\%$ from a base of 2.

As the figure indicates, decreasing the resistance towards rotation results in less sharp turns as expected. Furthermore, the orientation is decreased throughout the turns.

D.1.4 Inclusion of Added Mass

The added mass force has not been included in the revised model. However, it is investigated how inclusion of the added mass coefficient will affect the results of the model.

The result of the model with an added mass coefficient of 0.5 based on the BBO-equation is shown with blue in Figure D.7. The red curve is the result of including the added mass coefficients determined in Section 3.2.4 to $C_{11} = 0.0731$, $C_{22} = 17.3$, and $C_{66} = 7.03$.

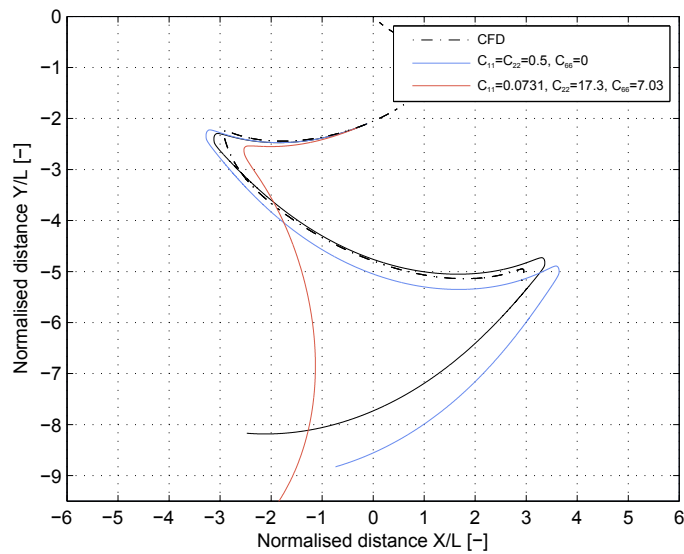


Figure D.7. Plate trajectory including an added mass coefficient of 0.5 from the BBO-equation is shown with blue and the plate trajectory including added mass coefficients obtained by the method presented in Chapter 3 is shown with red.

As the figure clearly indicates, the added mass coefficient matrix determined using the approach suggested by Simcik et al. (2008), does not seem to work for a flat plate in free fall. Using an added mass coefficient of 0.5 as suggested by the BBO-equation gives more reasonable results. However, a model neglecting the added mass effects is capable of predicting the trajectory of a falling plate within a reasonable margin of accuracy. This is in good agreement with Pesavento (2006) who concluded that unsteady effects such as added mass force and history force can be neglected for flat plates in free fall.

Appendix E

Logical Statements to Determine the Sign of Centre of Pressure Location

This appendix presents a function consisting of a set of logical statements developed to determine the location of the centre of pressure offset cp_o , due to the aerodynamic forces lift and drag. The function takes the plate orientation angle θ and the relative fluid velocity \vec{v} as input and returns the sign of the location of the center of pressure offset. Correlations such as those presented in Subsection 3.3.3 on page 35 can be used to estimate the length of the cp_o vector, while the direction is determined based on the script presented below. The following serves to give an overview of the script presented further below.

E.1 Examples of Centre of Pressure Location

Figure E.1 shows different relative fluid velocities and their angles calculated by Equation (3.11) on page 15. The relative fluid velocity vectors presented in the figure are $\vec{v} = (3, 0)$, $\vec{v} = (3, 1)$, and $\vec{v} = (-1, 3)$ respectively.

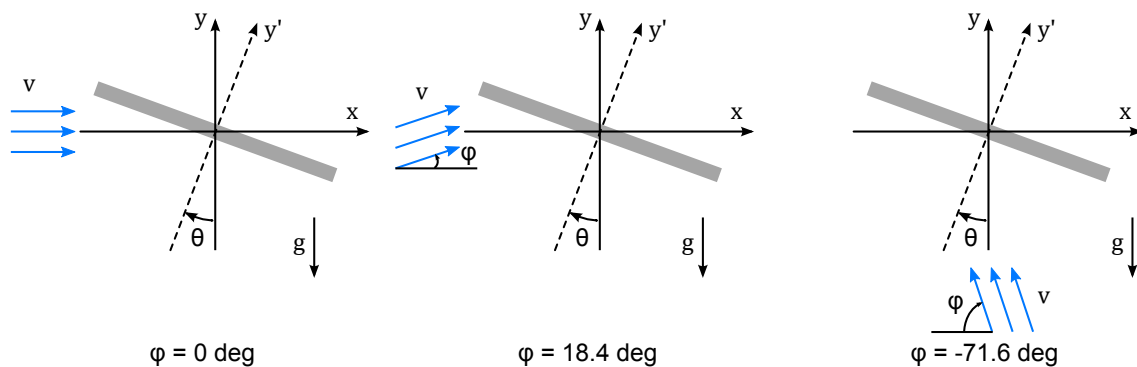


Figure E.1. Different relative fluid velocities and their respective angles ϕ .

Based on the MATLAB script presented further below, Figure E.2, Figure E.3, and Figure E.4 present the sign of the centre of pressure location for different relative fluid velocities as function of orientation angle θ .

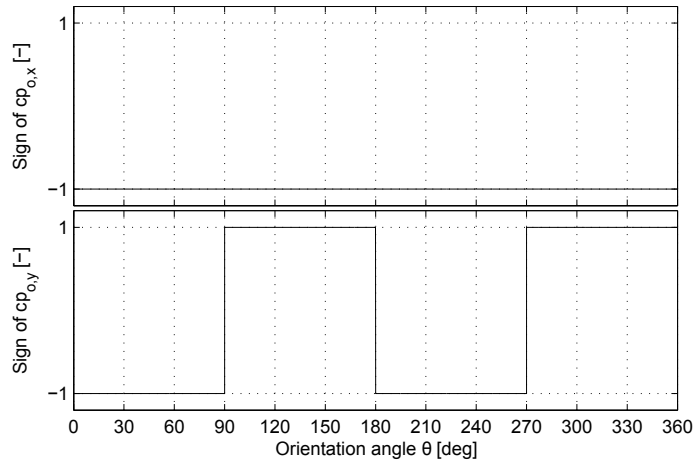


Figure E.2. Sign of the centre of pressure cp_o location as function of plate orientation angle at a constant relative fluid velocity $\vec{v} = (3,0)$ resulting in a relative fluid velocity angle $\varphi = 0.0$ deg.

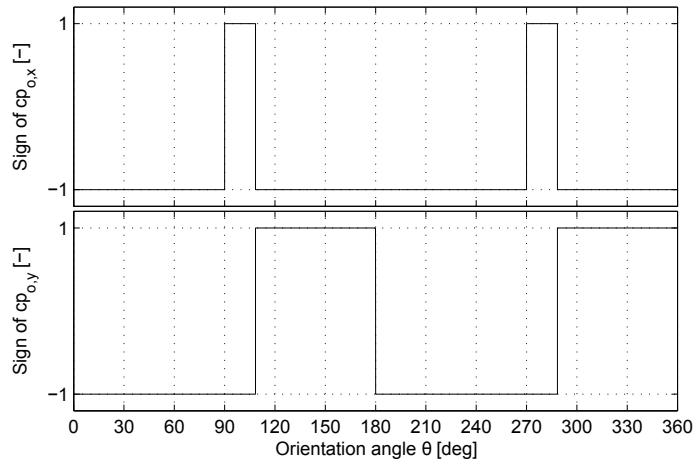


Figure E.3. Sign of the centre of pressure cp_o location as function of plate orientation angle at a constant relative fluid velocity $\vec{v} = (3,1)$ resulting in a relative fluid velocity angle $\varphi = 18.4$ deg.

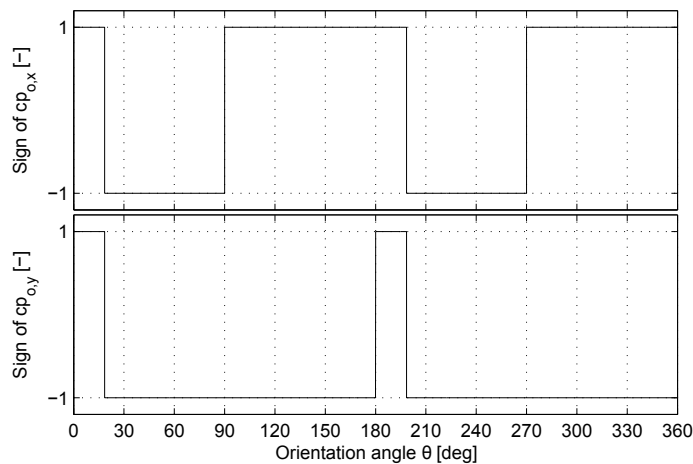


Figure E.4. Sign of the centre of pressure cp_o location as function of plate orientation angle at a constant relative fluid velocity $\vec{v} = (-1,3)$ resulting in a relative fluid velocity angle $\varphi = -71.6$ deg.

In the following the script used to determine the centre of pressure location is presented.

```

% function determining the sign of the centre of pressure.
function sign_cp = sign_cp_fcn(theta,v)
    phi = atan(v(2)/v(1))*180/pi; % angle between v and the global x-axis
    theta_scaled = mod(theta*180/pi,180)-180; % scaled to period of 180 deg

    if v(2) > 0
        if v(1) > 0
            if theta_scaled > -90 && theta_scaled < -90+phi
                sign_cp(1) = 1;
            else
                sign_cp(1) = -1;
            end
        else
            if theta_scaled < -90 && theta_scaled > -90+phi
                sign_cp(1) = -1;
            else
                sign_cp(1) = 1;
            end
        end
    end

    elseif v(2) < 0
        if v(1) > 0
            if theta_scaled < -90 && theta_scaled > -90+phi
                sign_cp(1) = 1;
            else
                sign_cp(1) = -1;
            end
        else
            if theta_scaled > -90 && theta_scaled < -90+phi
                sign_cp(1) = -1;
            else
                sign_cp(1) = 1;
            end
        end
    end

    if v(2) > 0
        if v(1) > 0
            if theta_scaled < 0 && theta_scaled > -90+phi
                sign_cp(2) = 1;
            else
                sign_cp(2) = -1;
            end
        else
            if theta_scaled < 0 && theta_scaled > -90+phi
                sign_cp(2) = -1;
            else
                sign_cp(2) = 1;
            end
        end
    end

    elseif v(2) < 0
        if v(1) > 0
            if theta_scaled > -90+phi && theta_scaled < 0
                sign_cp(2) = 1;
            else
                sign_cp(2) = -1;
            end
        end
    end
end

```

```
else
  if theta_scaled > -90+phi && theta_scaled < 0
    sign_cp(2) = -1;
  else
    sign_cp(2) = 1;
  end
end
end
end
```

Appendix F

Details on Dynamic Meshes

This appendix gives an overview of how the dynamic meshes are configured for the CFD simulations presented in this report. Figure F.1 shows a close-up of the mesh near the plate. Close to the plate the mesh consists of quadrilateral elements. This part of the mesh follows the motion of the plate. Outside the quadrilateral region the mesh consists of triangular elements. This part of the mesh is dynamic and updated according to the motion at each iteration.

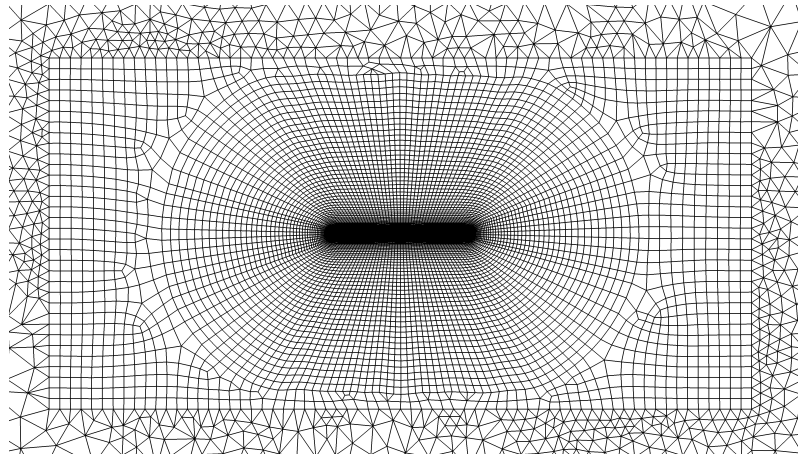


Figure F.1. Mesh close to plate used in all CFD simulations.

The free fall CFD simulations use the Six Degrees of Freedom (Six DOF) solver with implicit mesh update. Furthermore, smoothing, and re-meshing are enabled. When re-meshing is enabled, it is recommended to also enable smoothing (ANSYS, Inc., 2011c). These options are explained further in the following sections.

F.1 Six DOF Solver

The different zones of the mesh must be defined and coupled to a Six DOF UDF. In this work the quadrilateral cell zone around the plate is defined as a rigid body following the plate. This means that the quadrilateral mesh around the plate is not updated. By enabling *passive* in the Six DOF options, the forces and torques on the fluid zone moving with the plate will not be taken into account when updating the position of the plate. The plate is defined as a rigid body as well. For the plate *on* is enabled in the Six DOF options, and thereby the motion of the plate will be based on forces and torques on the plate itself.

E.2 Implicit Update

Implicit mesh update means that the dynamic mesh is updated during a time step. This option is advantageous for calculations where the mesh motion is dependent on the flow field. This is the case for a freely falling plate. Enabling Implicit update leads to a stronger coupling between mesh motion and the flow solution. Using Implicit Update makes it possible to run simulation which could not be solved without it and furthermore it is possible to use a higher time step than without Implicit update (ANSYS, Inc., 2011c). In this work the mesh is updated at every iteration to avoid divergence even though the computational time is increased significantly.

E.3 Smoothing

The dynamic mesh is updated using a spring based smoothing method. This method is normally used for zones with triangular mesh. It assumes the edges of the mesh to be an idealised network of springs. The equilibrium state of the mesh is the initial mesh before any motion. When a boundary node is displaced there will be a force proportional to the displacement on all the springs connected to the node. The spring constant factor controls the stiffness of the spring where 0 means that there is no damping on the springs (ANSYS, Inc., 2011c).

Table F.1. Overview of the setting used in the smoothing mesh method for updating the dynamic mesh.

Parameter	Setting
Method	Spring/Laplace/Boundary Layer
Spring Constant Factor	0.5
Convergence Tolerance	0.001
Number of Iterations	20
Elements	Tri in Tri Zones
Laplace Node Relaxation	1

For non-triangular cell zones the spring based method is recommended when the modelled motion is mostly perpendicular to the boundary zone and when the cell zone is moving mostly in one direction. This is not the case in the modelling of a falling plate. This is one of the reasons why the dynamic mesh zone is chosen to be meshed with triangular cells (ANSYS, Inc., 2011c).

E.4 Re-meshing

When the spring-based smoothing method is used, the cell sizes and cell quality can become very poor and result in negative cell volumes and convergence problems. This problem is solved by enabling the re-meshing option.

Re-meshing is done by joining cells which violate a skewness or size criteria chosen by the user. If the joined cells satisfy the criteria the mesh is updated locally with the joined cells.

The local cell re-meshing method is chosen in this work. This method only can only be used for triangular cells. This is one of the reasons that a triangular mesh is chosen in the dynamic mesh zones (ANSYS, Inc., 2011c).

Table F.2. Overview of the setting used for re-meshing to update the dynamic mesh.

Re-meshing Methods	Local Cell
Sizing Function	on
Minimum Length Scale [m]	0.0025
Maximum Length Scale [m]	0.001
Maximum Cell Skewness	0.6
Size Re-meshing Interval	1

Appendix G

Numerical Investigation of Rotational Drag and Lift Coefficients

This appendix contains information on a numerical investigation of the behaviour of drag and lift on rotating flat plates. The importance of the angular velocity will be investigated with the purpose of including rotational drag- and lift coefficients in the revised model.

In general, the configuration of the simulations corresponds to the configuration of the free fall simulation presented in Chapter 4. That is, the SST transition turbulence model is used to model turbulence, the mesh topology is the same, the first cell height is the same, and the time step size is the same. However, the domain is different, and the domain used is sketched in Figure G.1.

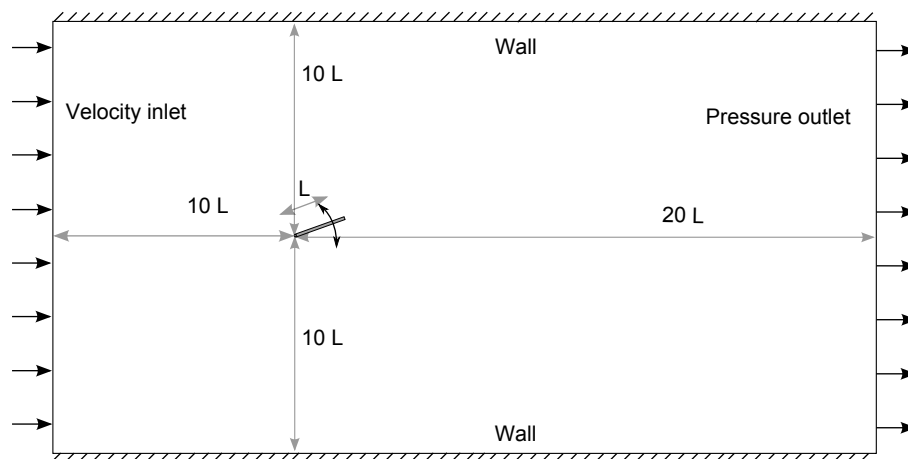


Figure G.1. Computational domain used for the simulations of a rotating plate.

The plate is rotated with the leading edge as the centre of rotation as visualised in the figure. The exact angular velocity of the plate is prescribed by an UDF, which is further described in Enclosure A. Using the UDF, angular velocities ranging from 5 deg/s to 90 deg/s are prescribed to the plate. The forces parallel and perpendicular to the fluid velocity, corresponding to drag and lift, are measured and the drag and lift coefficients are calculated. The results of the simulations are given in the following sections.

G.1 Rotational Lift as Function of Angle of Attack and Change in Angle of Attack

The lift coefficient as a function of angle of attack at different constant angular velocities is presented in Figure G.2. The dashed curve in the plot corresponds to a non-rotating plate, that is $d\alpha/dt = 0$ deg/s, and is presented in Figure 3.15 on page 27.

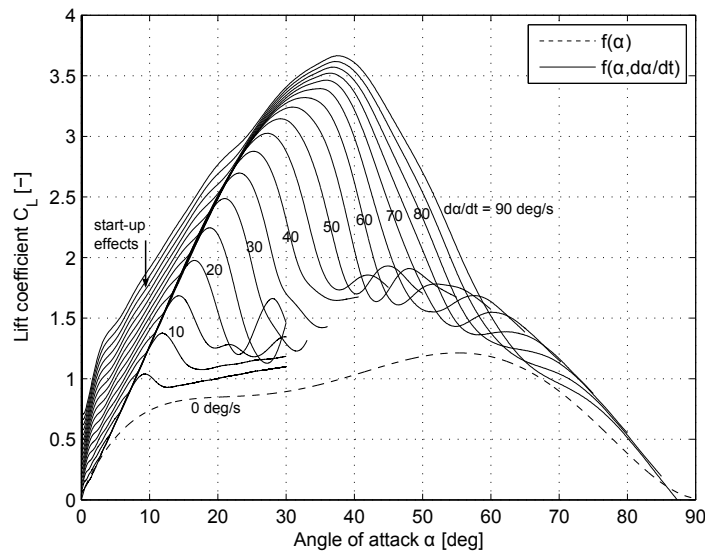


Figure G.2. Lift coefficient as function of the angle of attack at different angular velocities of the plate.

As the figure clearly indicates, the angle of attack at which the plate stalls increases when the rotational velocity is increased. Thereby, the lift coefficient becomes higher for higher rotational velocities.

Figure G.2 forms the basis of a new correlation for the lift coefficient, made to include rotational lift in the revised model. This correlation is based on polynomial regressions of the result presented in the figure. These regressions are illustrated in Figure 7.5, and the coefficients of these regressions are presented along with the revised model in Enclosure B. The start-up effects marked with the arrow in Figure G.2 are expected to be caused by a step acceleration of the plate from an angular velocity of 0 deg/s to the constant angular velocity specified in the UDF. The regressions do not account for this effect.

G.2 Rotational Drag as Function of Angle of Attack and Change in Angle of Attack

The results for drag coefficient as function of the angle of attack for different constant angular velocities are presented in Figure G.3. The dashed curve in the plot corresponds to a plate not rotating, that is $d\alpha/dt = 0$ deg/s. It is presented in Figure 3.10 on page 22.

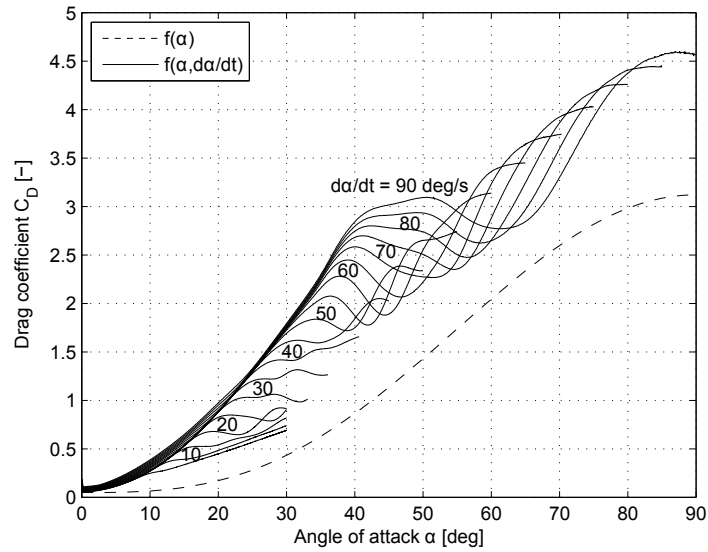


Figure G.3. Drag coefficient as function of the angle of attack at different angular velocities of the plate.

Based on Figure G.3 a new correlation describing the drag coefficient is developed. This correlation is used in the revised model. Similar to Figure G.2, Figure G.3 clearly indicates that the point of stall increases with the angular velocity. In the development of the correlations to be included in the revised model the drag coefficient beyond the stall point is assumed to be constant for simplicity.

The correlation developed based on Figure G.3 is illustrated in Figure 7.9 for different constant angular velocities.

G.3 Visualisation of the Flow Field

In this section the flow fields around the plate at different angular velocities are presented to give an overview of what causes the enhanced lift coefficient.

Figure G.4 illustrates the velocity magnitude in the flow field around a plate. The plate in Figure G.4 is not rotating. It is clear from the figure that the stall point has been exceeded and that the flow is fully separated from the plate.

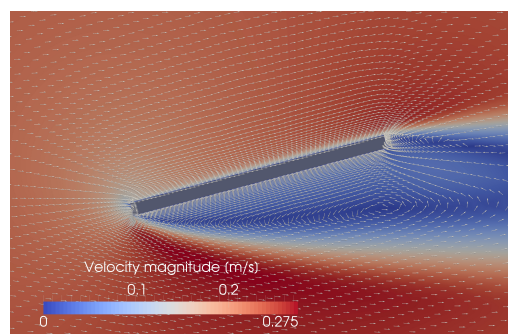


Figure G.4. Plate at an angle of attack of 15 deg and an angular velocity of 0 deg/s.

Figure G.5 shows the flow field around the plate just after the stall point. After the stall point, an increase in the angle of attack will not result in an increase of the lift coefficient. The flow is about to separate.

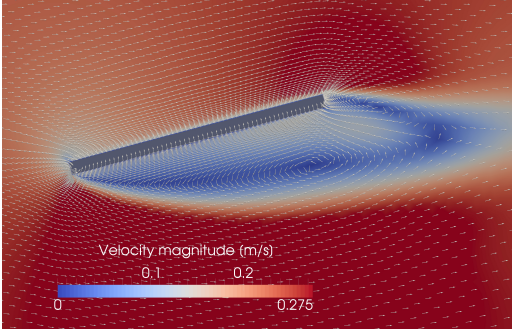


Figure G.5. Plate at an angle of attack of 15 deg and an angular velocity of 10 deg/s.

In Figure G.6 the stall point is not reached and the flow remains attached to the plate. Consequently the lift coefficient will still increase with the angle of attack. In the range of angular velocities investigated in the present study, it is evident that a higher the angular velocity results in the flow to remain attached to the plate at higher values of the angle of attack.

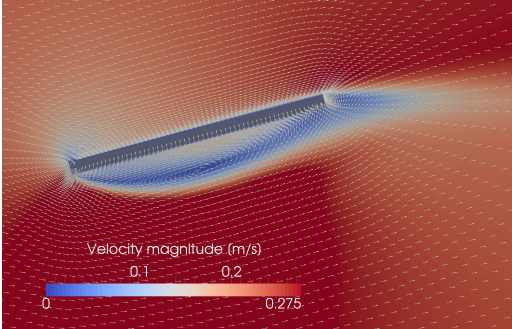


Figure G.6. Plate at an angle of attack of 15 deg and an angular velocity of 25 deg/s.

Appendix H

Detailed CFD Results

The following pages contain a selection of figures illustrating relevant results from the CFD simulation of the flat plate in free fall. These include the translational and rotational position, velocity, and acceleration of the plate as function of time presented in Figure H.1 to H.6. Additionally, Figure H.7 to Figure H.12 show the angle of attack, the change in angle of attack, the viscous force, the pressure force, the net force, and the net moment as function of time. Furthermore, Figure H.13 to Figure H.16 show the centre of pressure location, the Reynolds number, and total net force perpendicular to the relative fluid velocity corresponding to lift plus unsteady effects, and the total net force parallel to the relative fluid velocity corresponding to drag plus unsteady effects. All quantities are shown as function of time.

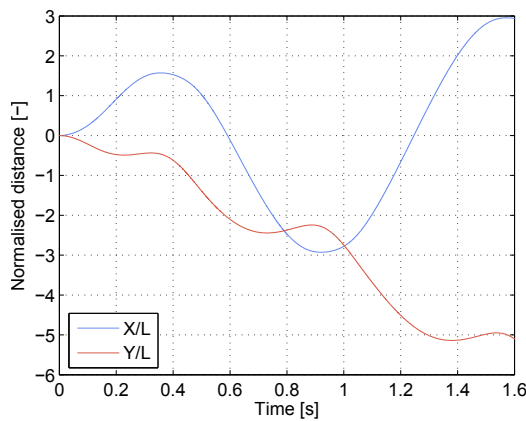


Figure H.1. Normalised x- and y-position as function of time.

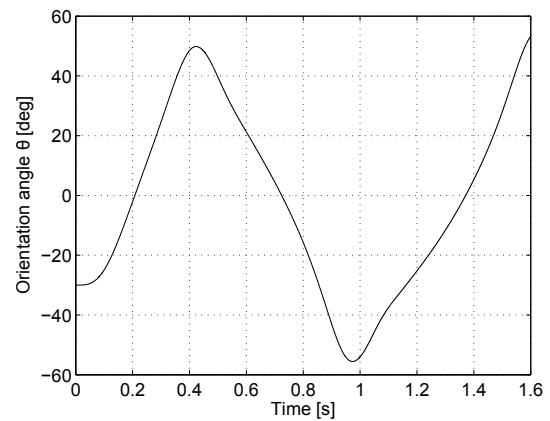


Figure H.2. Orientation angle as function of time.

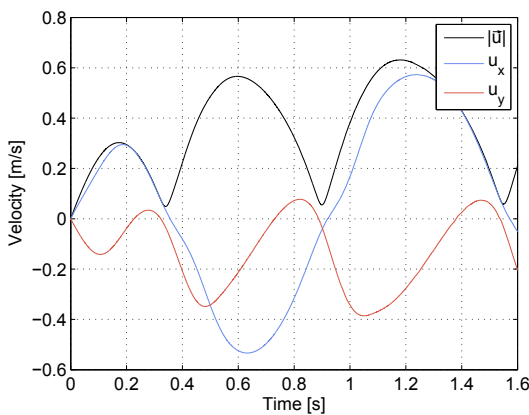


Figure H.3. Translational velocity as function of time.

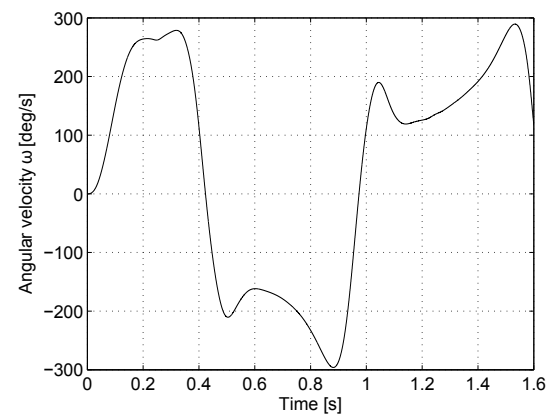


Figure H.4. Angular velocity as function of time.

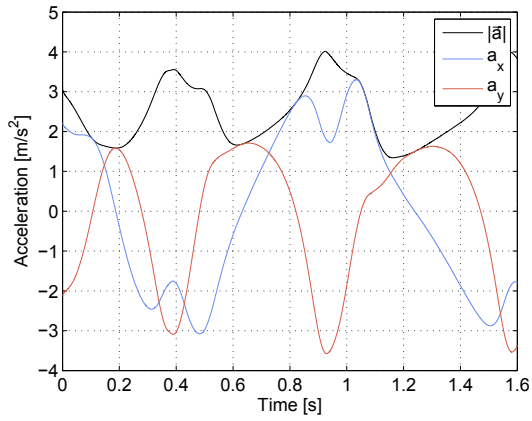


Figure H.5. Translational acceleration as function of time.

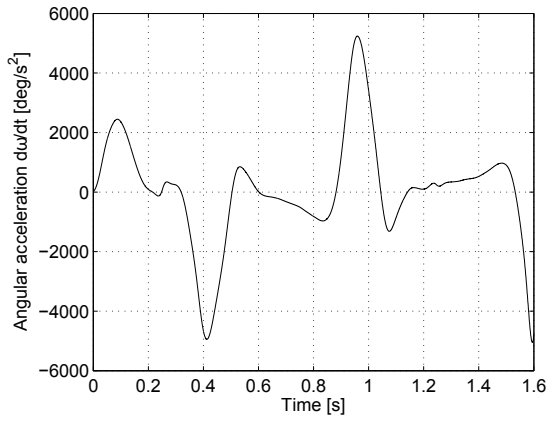


Figure H.6. Angular acceleration as function of time.

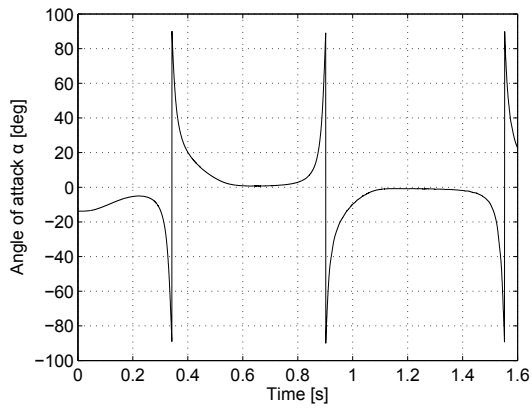


Figure H.7. Angle of attack as function of time.

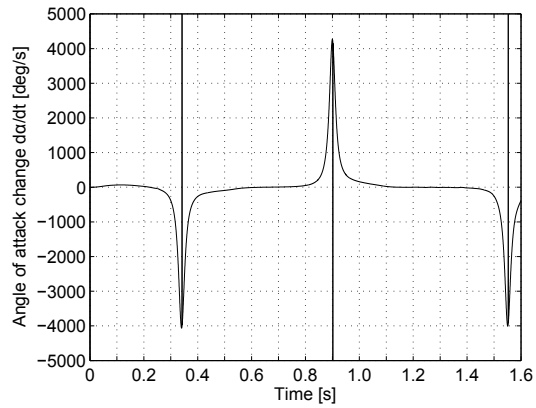


Figure H.8. Change in angle of attack as function of time.

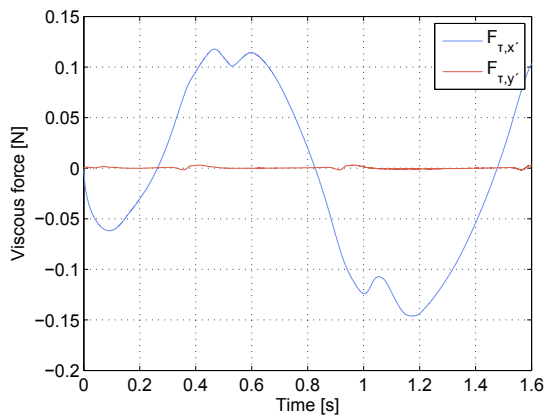


Figure H.9. Viscous force in local coordinates as function of time.

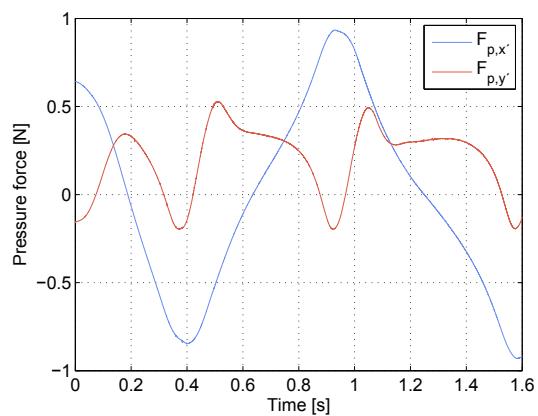


Figure H.10. Pressure force in local coordinates as function of time.

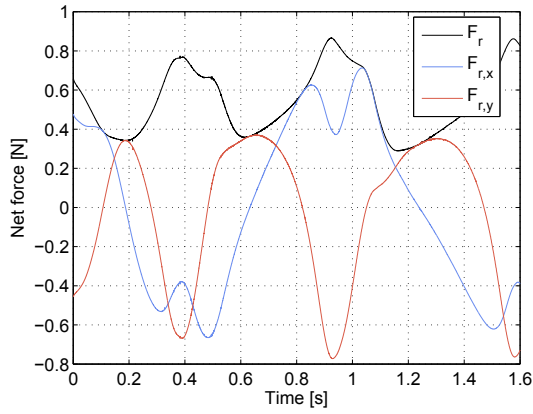


Figure H.11. Net total force as function of time.

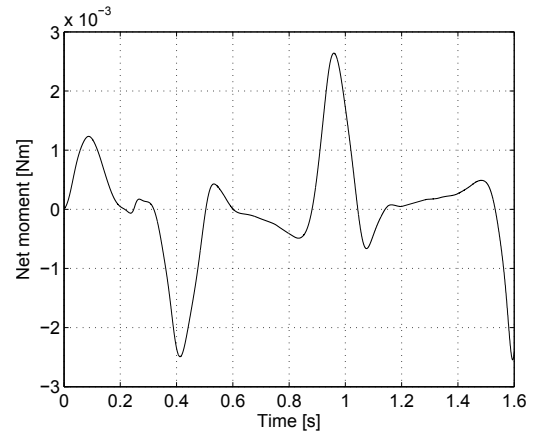


Figure H.12. Net total torque as function of time.

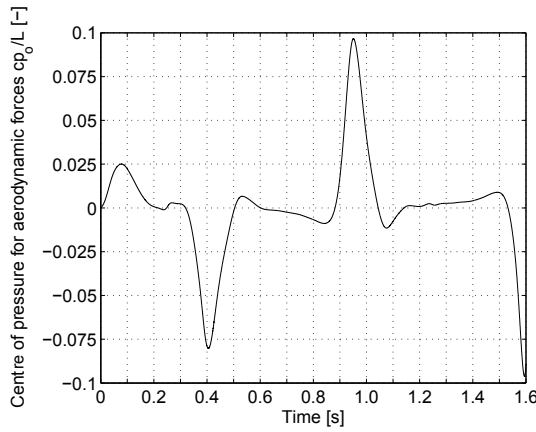


Figure H.13. Centre of pressure for aerodynamic forces as function of time.

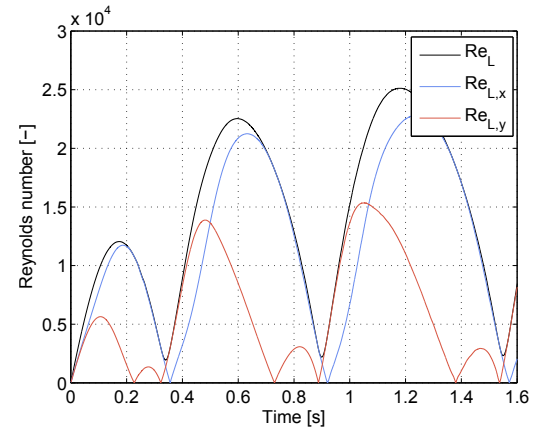


Figure H.14. Reynolds number as function of time.

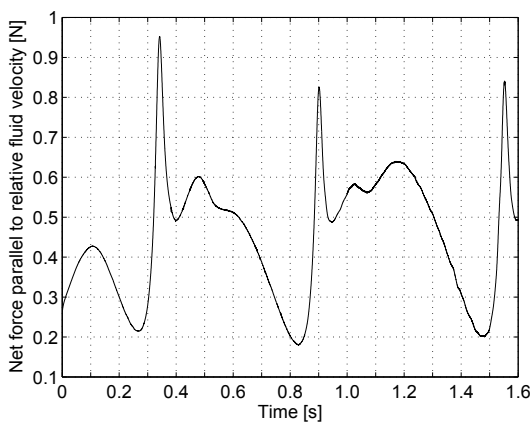


Figure H.15. Total force parallel to relative fluid velocity as function of time (drag plus unsteady contribution).

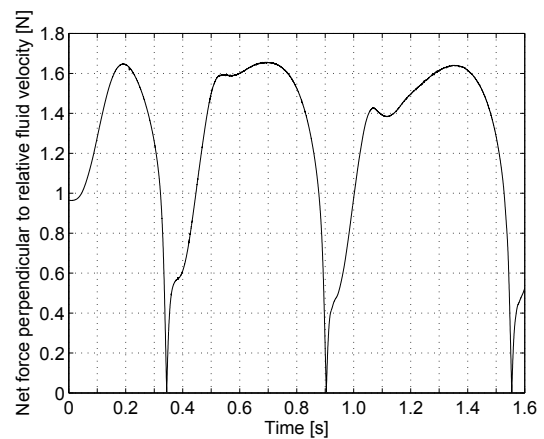


Figure H.16. Total force perpendicular to relative fluid velocity as function of time (lift plus unsteady contribution).

Appendix I

CD Content

I.1 Digital Copy of the Report

I.2 ANSYS Fluent Files

I.2.1 Meshes

I.2.2 User Defined Functions

I.2.3 Results of CFD Simulations

I.2.4 Case file

I.3 References

I.4 Revised 2D Model

I.5 Data from Free Fall Experiment

I.6 Figures

